Université de Liège
Faculté des Sciences Appliquées
Département d'Electricité, Electronique et Informatique

Ecole Royale Militaire
Faculté Polytechnique
Département CISS
(Communication, Information Systems & Sensors)

MAGNETIC SHIELDING WITH HIGH-TEMPERATURE SUPERCONDUCTORS

Samuel DENIS
Thèse présentée en vue de l'obtention
du grade de docteur en Sciences
de l'Ingénieur
Juin 2007

Remerciements

C'est avec une certaine émotion que j'écris ces remerciements. A quelques heures de la cloture de ce manuscrit, je réalise enfin que j'approche de la fin d'une histoire qui a duré cinq ans.

Je n'aurais pas pu réaliser ma thèse de doctorat sans l'Université de Liège et l'Ecole Royale Militaire de Belgique qui ont décidé de s'associer pour mener à bien une recherche sur le blindage magnétique par matériaux supraconducteurs. Je tiens à remercier ces deux institutions qui sont toutes les deux représentées dans le groupe SUPRATECS, et j'espère avoir été à la hauteur de la confiance qui m'a été témoignée. Plus particulièrement, je suis reconnaissant des moyens mis à ma disposition pour mener à bien ma recherche. Je suis concient que toutes les équipes n'ont pas ce luxe. Je pense qu'un tel résultat a été notamment possible grâce à l'association des deux institutions précitées et à la volonté que mon doctorat soit réalisé en cotutelle par l'Université de Liège et l'Ecole Royale Militaire. Espérons que de tels projets voient encore le jour.

Mais cette période de ma vie n'aurait pas été la même sans la rencontre de différentes personnes que je tiens à remercier ici et dont je retiendrai les qualités suivantes.

J'ai rencontré mon promoteur ULg, le professeur Benoit Vanderheyden, à la fin de mes années d'étude ingénieur. C'est lui qui m'a proposé le premier de réaliser ce travail de thèse. Une des raisons qui m'a fait accepter cette proposition est la personnalité de mon promoteur qui a comme grande qualité son honnêteté et son intégrité intellectuelle. Je retiendrai aussi la très grande liberté qu'il ma donnée, me forçant à défendre mes choix et mes résultats seul. Même si cela a pu être parfois déroutant, je pense que c'est une étape obligatoire pour se construire scientifiquement. Benoit Vanderheyden a également une très grande curiosité et culture scientifique. Sa formation théorique poussée lui permet de cerner très vite un problème, même en-dehors de son domaine. Ainsi, les petites discussions de couloir ont été souvent très enrichissantes. Finalement, je tiens à souligner son talent pour la rédaction d'un rapport scientifique. J'ai dû souffrir de sa très grande exigence à avoir un texte cohérent et fluide. En fin de compte, je suis content d'avoir subi cette requête et espère que la qualité de ce manuscrit traduira mon apprentissage dans ce domaine, oh combien absent de notre formation.

Le lieutenant-colonel Michel Dirickx, qui a supervisé notre étude au sein de l'Ecole Royale Militaire, est mon deuxième promoteur. Bien que nous devions réaliser des objectifs prédéfinis au début de l'étude (les fameux milestones ...), Michel Dirickx m'a toujours laissé une liberté d'investigation pour autant que les délais soient respectés. Je tiens à le remercier pour cette marque de confiance. Grâce à Michel Dirickx, j'ai pu ne pas trop souffrir de l'administration parfois (souvent ?) un peu lourde pour acheter du matériel. Il prenait le relais pour veiller à ce que les fameuses trois offres soient correctement présentées. Son souci du détail et de la cohérence m'ont poussé à vérifer mes résultats et mon manuscrit plutôt deux fois qu'une.

Le professeur Philippe Vanderbemden est la première personne qui m'a initié au monde de la supraconductivité. Il a également été mon chef de laboratoire pendant ces cinq années de recherche. Je tiens à le remercier sincèrement des nombreux moyens mis à ma disposition. Outre ses connaissances techniques poussées en mesures électriques, je retiendrai de Philippe Vanderbemden sa très grande efficacité et sa rapidité d'esprit parfois déconcertante. Il faut également mentionner ses grandes qualités de pédagogue et son dynamisme.

Ce projet n'aurait pas vu le jour sans la volonté et le soutien des professeurs Marcel Ausloos et Rudi Cloots, respectivement président et secrétaire du groupe SUPRATECS. J'ai pu apprécier la grande curiosité scientifique du professeur Ausloos et l'enthousiasme du professeur Cloots.

Je tiens à vivement remercier le docteur Ernst Helmut Brandt de Stuttgart de faire partie de mon jury de thèse mais également de nous avoir rendu visite à Liège en juin 2006. Cette rencontre a été décisive pour l'avancement de mon étude théorique.

J'aimerais remercier le professeur Marc Piette de l'Ecole Royale Militaire pour l'attention qu'il portera à ce manuscript. J'ai également apprécié d'avoir été invité aux Lema Days où j'ai pu présenter mes travaux. Je suis également content et fier de retrouver le docteur Frédérik Wolff Fabris dans mon jury. Finalement, je suis reconnaissant au professeur Jacques Destiné de présider ce jury.

Je tiens finalement à remercier différents chercheurs qui ont chacun contribué à l'avancement de mes travaux. Il faut bien sûr d'abord mentionner Laurent Dusoulier du laboratoire de chimie inorganique de l'Université de Liège qui n'a plus assez de doigts de pied et de main pour compter les nombreux échantillons qu'il a synthétisés. Je retiendrai avant tout sa persévérance. J'ai également quelques bons souvenirs de séjours en conférence passés avec lui.

A Montéfiore, je dois évidemment remercier Jean-François Fagnard qui a un véritable don pour la pose de contacts électriques. Grâce à sa patience, j'ai pu progressivement arriver à faire une mesure R(T) correcte. Il m'a également beaucoup aidé en faisant une partie des caractérisations électriques pour Laurent. Je retiendrai de Philippe Laurent son enthousiasme et ses compétences techniques. Je n'oublierai bien sûr jamais son humour oh combien subtil ! Je souhaite tout le meilleur à Grégory Lousberg qui, j'en suis sûr, fera un très bon doctorat. Je le remercie pour sa bonne humeur. Finalement, je n'oublierai pas les doigts de fée de Joseph Simon et les connaissances techniques de Pascal Harmeling.

J'ai gagné beaucoup de temps grâce aux deux étudiants ingénieurs que j'ai supervisés. Anne-Françoise Gerday a réalisé le dispositif de mesure d'efficacité de blindage pour les échantillons plans et Denis Bajusz celui pour caractériser les tubes en champ DC. Je tiens à les remercier sincèrement pour l'excellent travail fourni.

Je garde un très bon souvenir de ma rencontre avec Gianluca Grenci de Turin. Les trois mois durant lesquels il a travaillé avec moi à Liège ont été très enrichissants. Je me rappelle également de quelques bons moments dans le carré ...

Pour ne pas les compromettre, je ne citerai pas les différentes personnes qui ont relu mon manuscrit. Mais je les remercie de tout coeur et tiens à dire qu'elles ont contribué à améliorer significativement la qualité de ce texte.

Mon passé et mon présent ne seraient pas ce qu'ils sont sans ma famille. Mes parents m'ont inculté le goût du savoir, de la beauté, de l'effort et du dépassement

de soi. Ces différentes qualités ont été primordiales pour mener à bien cette thèse de doctorat.

Je ne serais sûrement pas en train d'écrire ces quelques mots sans avoir rencontré Geoffrey Gloire, Gloire comme la gloire, qui a trouvé les bons mots pour me convaincre de ne pas baisser les bras. Je tiens à lui dédier ce modeste travail et espère partager encore beaucoup de moments avec lui.

Résumé

Une solution classique pour blinder un champ électromagnétique haute fréquence consiste à employer des matériaux bons conducteurs qui atténuent le champ grâce à l'effet de peau. Le blindage est d'autant meilleur que l'épaisseur de l'écran est grande devant l'épaisseur de peau. A basse fréquence, ces matériaux continuent à blinder le champ électrique (par le principe de la cage de Faraday), mais deviennent de très mauvais écrans du champ magnétique. En effet, l'épaisseur de peau augmentant quand la fréquence diminue, le blindage par effet de peau devient inefficace.

Outre leurs propriétés électriques remarquables, les supraconducteurs présentent également des propriétés magnétiques spécifiques. Par exemple, un supraconducteur refroidi en-dessous de sa température critique "expulse" le flux d'induction magnétique de son volume. Cette propriété peut être utilisée pour réaliser des blindages magnétiques par matériaux supraconducteurs.

Cette thèse de doctorat s'inscrit dans le cadre d'un projet de recherche portant sur l'étude du blindage magnétique par supraconducteurs à haute température critique (HTS). Cette recherche est menée dans le groupe SUPRATECS de l'Université de Liège en collaboration avec l'Ecole Royale Militaire de Belgique. Une première partie du projet consiste à réaliser des blindages HTS. Cette étude a été menée par Laurent Dusoulier, un étudiant doctorant du laboratoire de chimie inorganique structurale de l'Université de Liège. Vu que les HTS sont des céramiques cassantes, il a été choisi de déposer un film supraconducteur sur un substrat métallique par la technique de déposition électrophorétique (EPD).

La deuxième partie du projet comprend la caractérisation des échantillons réalisés par la technique EPD, ainsi que l'étude de la pénétration du champ magnétique dans des blindages HTS. Ma thèse de doctorat porte sur ces dernières questions.

Dans un premier temps, nous avons caractérisé les propriétés supraconductrices et les propriétés de blindage magnétique des échantillons synthétisés en chimie. Cette étude a parfois nécessité de réaliser des montages expérimentaux spécifiques. Nous avons montré que les niveaux de blindage que l'on peut obtenir avec un échantillon supraconducteur sont généralement supérieurs aux niveaux obtenus avec des écrans magnétiques classiques, si le champ à blinder est inférieur à un seuil caractéristique à l'écran HTS.

Ensuite, nous avons étudié de manière détaillée les propriétés de blindage de tubes HTS soumis à un champ magnétique axial. Cette étude a été menée de manière expérimentale et à l'aide de simulations numériques basées sur la méthode de Brandt. Grâce à ces résultats, nous avons déterminé le champ limite qu'un tube HTS peut blinder, nous avons étudié la variation spatiale du facteur de blindage, ainsi que sa dépendance fréquentielle.

Finalement, grâce aux simulations numériques, nous avons étudié les propriétés de blindage magnétique d'échantillons HTS axisymétriques présentant des configurations d'un intérêt pratique. Cette étude permet d'évaluer le gain que l'on obtient en fermant un tube par un capuchon, de mesurer l'impact d'un trou dans ce capuchon, d'évaluer l'effet d'une soudure métallique et l'influence de la non-homogénéité des propriétés supraconductrices sur les niveaux de blindage d'un tube HTS.

Contents

1 Introduction **1**
1.1 Traditional solution to shield a low frequency magnetic field 2
1.1.1 Magnetic shielding by the deviation of the flux lines 2
1.1.2 Magnetic shielding by the skin effect 3
1.1.3 Difficulties associated to the use of ferromagnetic materials to shield a magnetic field 4
1.2 Magnetic shielding with high-temperature superconductors 5
1.3 Introduction to the geometric effects 6
1.4 Aim of the thesis 8
1.5 Organization of the thesis 9

2 Magnetic properties of superconductors **11**
2.1 History and basic features of superconductivity 11
2.2 Three critical values 13
2.3 Some applications of superconductors 14
2.4 Type-I versus type-II superconductors 16
2.4.1 Type-I superconductors 16
2.4.2 Type-II superconductors 22
2.5 Irreversible type-II superconductors 25
2.5.1 Bean model 25
2.5.2 Shielding with irreversible type-II superconductors 28
2.6 Summary 30

3 High-temperature superconductors (HTS) **33**
3.1 Chemical aspects 33
3.2 Granularity 35
3.3 Illustration of magnetic shielding in a bulk HTS 37
3.4 Techniques for fabricating a HTS magnetic shield 39
3.4.1 The electrophoretic deposition (EPD) technique 41
3.4.2 Heat treatment after the deposition 43
3.4.3 HTS samples made with the EPD technique 44
3.5 Summary 44

4 Methods to study the field penetration in HTS **47**
4.1 The method of Campbell and Evetts 47
4.2 Field dependence of the critical current density: the Kim law 49

4.3 Limitation of the Bean model related to the assumed relationship between E and J . . . 50
    4.3.1 Flux creep and constitutive law $\mathbf{E} \propto \mathbf{J}^n$ . . . 51
4.4 Geometric limitations of the Bean model . . . 53
4.5 Study of the field penetration into geometries with demagnetizing effects . . . 54
    4.5.1 Axial symmetric geometries . . . 54
    4.5.2 Infinitely long samples in a transverse magnetic field . . . 58
4.6 Summary . . . 59

5 Superconducting and shielding properties of planar HTS samples 61
5.1 Characterization techniques . . . 61
    5.1.1 Electrical transport measurements . . . 62
    5.1.2 AC magnetic measurements . . . 63
    5.1.3 Shielding characterization of planar samples . . . 64
5.2 Shielding properties of Y-123 coatings with non-connected grains . . . 66
5.3 EPD coatings on nickel . . . 68
5.4 EPD coatings on silver . . . 69
    5.4.1 Chemical characterization . . . 69
    5.4.2 Resistive transition . . . 70
    5.4.3 Critical current density . . . 71
    5.4.4 Shielding effect . . . 73
5.5 Summary . . . 75

6 Magnetic shielding properties of tubular HTS samples 77
6.1 Infinitely long hollow samples in the parallel geometry . . . 78
6.2 Characterization techniques . . . 81
    6.2.1 DC applied field . . . 81
    6.2.2 AC applied field . . . 82
6.3 Magnetic shielding properties of finite HTS tubes in the parallel geometry . . . 83
    6.3.1 Sample . . . 85
    6.3.2 Theory . . . 86
    6.3.3 Results in the DC mode . . . 87
    6.3.4 Results in the AC mode . . . 95
6.4 Magnetic shielding properties of a HTS EPD tube in the parallel geometry . . . 98
    6.4.1 DC mode . . . 99
    6.4.2 AC mode . . . 100
6.5 Magnetic shielding properties of a ferromagnetic tube in the parallel geometry . . . 101
6.6 Magnetic shielding properties of HTS tubes in the transverse geometry . . . 102
    6.6.1 Results . . . 103
6.7 Summary . . . 104

7 Numerical study: effects of a cap, a non-superconducting joint, and non-uniform superconducting properties 107
7.1 Constitutive laws and model parameters 108
7.2 Comparison of the shielding properties of open and closed tubes . . . 109
  7.2.1 The threshold induction $B_{\rm lim}$ 110
  7.2.2 Spatial variation of the shielding factor 111
7.3 Tube presenting an annular defect 115
7.4 Effect of inhomogeneities on the shielding properties 120
7.5 Summary 122

8 Conclusions and outlook 123

A Numerical method to study the field penetration in thin films 127

B Publications 129

Bibliography 131

Chapter 1

Introduction

Shielding a low frequency magnetic field is a challenging task [1, 2, 3, 4]. As long as the frequency of the source field remains large, typically $f > 1$ MHz, conducting materials can be used to attenuate an electromagnetic field with the skin effect. At low frequencies however, shields made of normal conducting materials require prohibitive thicknesses to attenuate magnetic fields, as the skin depth, δ, becomes large (for instance, $\delta \cong 1$ cm for copper at 50 Hz and 300 K). Nevertheless, conductors continue to act as good electric shields and can be used to make a Faraday cage.

The traditional approach to shield low frequency magnetic fields consists in using soft ferromagnetic materials with a high relative permeability [1]. If low temperatures are allowed by the application (77 K for cooling with liquid nitrogen), shielding systems based on high-temperature superconductors (HTS) compete with the traditional solutions [5]. Below their critical temperature, T_c, HTS are strongly diamagnetic and expel a magnetic flux from their bulk. They can be used to construct enclosures that act as very effective magnetic shields over a broad range of frequencies [5].

For these reasons, the SUPRATECS group has undertaken a research on HTS magnetic shields. The project, which emanates from a collaboration between the University of Liège and the Royal Military Academy of Belgium, consists of two major parts.

The first part is the construction of a HTS magnetic shield, which can be used at the boiling point of liquid nitrogen, $T = 77$ K. This work has been carried out by Laurent Dusoulier, a PhD student from the laboratory of inorganic structural chemistry of the University of Liège. As HTS are brittle ceramics, bulk shields are difficult to obtain. Instead, it has been decided to deposit a HTS film on a metallic substrate of chosen geometry by the electrophoretic deposition (EPD) technique. This method should allow us to make shields of large sizes and arbitrary shapes.

The second part of the project includes the characterization of the samples made by the EPD technique, and the study of the field penetration into HTS magnetic shields. The questions addressed in this dissertation are devoted to this second part.

Before clarifying these questions, we explain the traditional solution to screen a DC or low frequency magnetic field, introduce magnetic shielding with superconductors, and draw the attention to the geometric effects.

1.1 Traditional solution to shield a low frequency magnetic field

Electromagnetic shielding has two main purposes. The first one is to prevent an electronic device from radiating electromagnetic energy, in order to comply with radiation regulations, or to protect neighbouring equipments from electromagnetic noise. This is called the emission problem. In military applications, shielding is sometimes used to reduce the electromagnetic signature of some devices, in order to prevent them from being detected by radars or mines.

The second purpose of shielding is to protect devices from radiations emitted in their surroundings, in order to take advantage of their full capabilities. This is called the immunity problem. As an example, very sensitive sensors, in order to be used optimally, often need to be shielded from noisy environments. This is particularly important for biomagnetism measurements using superconducting quantum interference devices (SQUID), that aim at detecting very low magnetic inductions (around 10^{-13} T) produced by the human brain [6, 7, 8]. Such low levels cannot be detected in a noisy environment, and the measurement is generally carried out in a shielded area.

A screen is characterized by its shielding factor, SF, which is a measure of the attenuation that an incident electromagnetic field undergoes through the barrier (SF is generally expressed in dB). The shielding factor, SF, depends on the screen material and the screen thickness, but also on the frequency of the incident field, and on the geometry [1, 2, 3, 9].

The traditional approach to shield a low frequency or a DC magnetic field is to use ferromagnetic materials for the screen. These materials are characterized by a relative permeability, μ_r, that is much larger than 1. There are two main shielding mechanisms with ferromagnetic screens. To point out these two contributions, we consider two cases: the shielding of a DC or an AC magnetic field. First, we focus on the DC case.

1.1.1 Magnetic shielding by the deviation of the flux lines

The principle of magnetic shielding with ferromagnetic materials in the DC case is illustrated in figure 1.1, which shows an infinite ferromagnetic tube in a uniform DC transverse magnetic field, H_a. As the reluctance, $\mathcal{R} = \ell/(A\,\mu)$, in the ferromagnetic material is much lower than in air (ℓ is the path length, A is the cross-section of the path, μ is the magnetic permeability), the magnetic flux lines "channel" in the magnetic material. As a result, the tube diverts the flux lines from the inner region and the magnitude of the internal field, H_i, is strongly reduced with respect to H_a.

For the geometry of figure 1.1, one can show that H_i is uniform, and that SF in dB is given by [10, 11]:

$$SF = 20\,\log\left[\frac{H_\mathrm{a}}{H_\mathrm{i}}\right] = 20\,\log\left[\frac{(\mu_\mathrm{r}+1)^2 a_2^2 - (\mu_\mathrm{r}-1)^2 a_1^2}{4\mu_\mathrm{r} a_2^2}\right] \tag{1.1}$$

$$\cong 20\,\log\left[\mu_\mathrm{r}\,\frac{1-(a_1/a_2)^2}{4}\right], \tag{1.2}$$

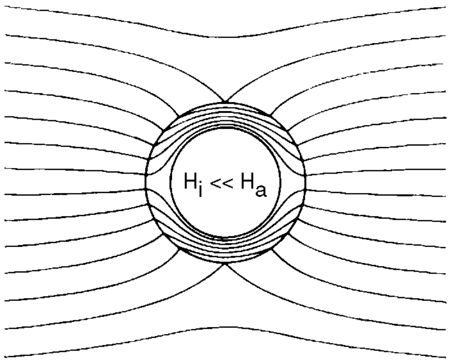

Figure 1.1: magnetic shielding realized by an infinite ferromagnetic tube in a uniform DC transverse magnetic field, H_a. The lines represent the magnetic induction. As the magnetic flux lines concentrate in the ferromagnetic shield, the internal field, H_i, is strongly reduced with respect to H_a.

where a_2 (resp. a_1) is the external (resp. internal) tube radius. The last approximation (1.2) holds when $\mu_\mathrm{r} \gg 1$. We find for instance that $SF \cong 54$ dB for $\mu_\mathrm{r} = 10^5$, $a_2 = 10$ cm, and $a_1 = 9.9$ cm. From (1.1), we see that SF only depends upon the ratio a_1/a_2, and μ_r. Hence, for a fixed SF, the thickness of the shield scales with the linear dimension of the volume to shield.

1.1.2 Magnetic shielding by the skin effect

Now, we consider that the field to shield is an alternating magnetic field. Then, any conducting material attenuates the field with the skin effect. To illustrate this effect, we consider an infinite conducting slab of thickness d which is subjected to a parallel AC magnetic field at its left surface, H_a (see figure 1.2).

In a first approximation, one can show that the shielding factor of the slab in dB is given by:

$$SF = 20\,\log\left(\frac{H_\mathrm{a}}{H_\mathrm{t}}\right) = 20\,\log \mathrm{e}^{d/\delta} \cong 8.68\,d/\delta, \tag{1.3}$$

where

$$\delta = \sqrt{\frac{2}{\omega\sigma\mu}} \tag{1.4}$$

is the skin depth. The pulsation ω is given by $\omega = 2\pi f$ where f is the frequency of H_a, and the magnetic permeability μ is given by $\mu = \mu_\mathrm{r}\mu_0$ ($\mu_0 = 4\pi\ 10^{-7}$ H/m is the permeability of vacuum). From (1.3), we see that the SF increases by ~ 8.68 dB for each increase of the thickness d by an amount δ. From this result, assuming that the frequency of the field to shield is 100 Hz, and that the screen thickness is 1 mm, we deduce at 300 K

$$SF \cong 1.33\ \mathrm{dB}, \tag{1.5}$$

for a copper plate, and

$$SF \cong 71.5\ \mathrm{dB}, \tag{1.6}$$

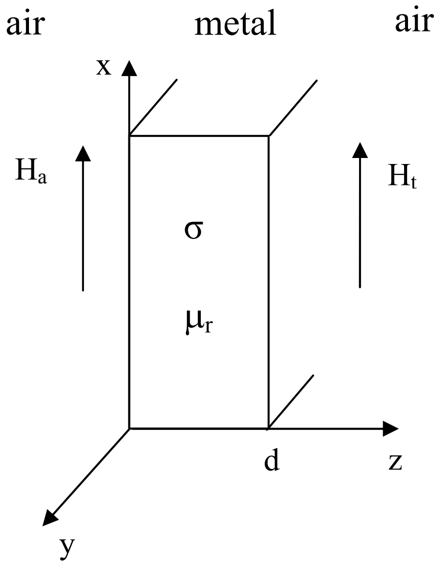

Figure 1.2: infinite metallic slab, of tickness d, with an incident AC magnetic field parallel to the surface $z = 0$. The incident field is denoted by H_{a}, and the field behind the slab is H_{t}. The metallic plate has an electrical conductivity σ, and a relative permeability μ_{r}.

for a ferromagnetic screen with $\mu_{\mathrm{r}} \cong 10^5$. Hence, at low frequencies, by using a ferromagnetic plate, one can reach a much higher SF than by using a normal conducting material.

Besides the shielding with the skin effect, there is also the deviation of the flux lines by the ferromagnetic material, which was explained above in the DC case. For an AC magnetic field, the actual attenuation is the result of both mechanisms. Note that the magnetic shielding by the deviation of the flux lines is very sensitive to the geometry of the shield. As somewhat "extreme" illustration, one can show that no flux line is deviated in the case of the ferromagnetic slab of figure 1.2 [10], because of its infinite extension. Hence, only the skin effect contributes to shielding in this case. The geometry effects are discussed in section 1.3. Before, we point out some difficulties associated to the use of ferromagnetic materials to screen a magnetic field, and introduce magnetic shielding with superconductors.

1.1.3 Difficulties associated to the use of ferromagnetic materials to shield a magnetic field

There are three intrinsic difficulties when using ferromagnetic materials for magnetic shielding. First, to obtain high SF with reasonable shield thicknesses (lower than 1 cm), ferromagnetic materials with a very high relative magnetic permeability, $\mu_{\mathrm{r}} \geq 10^4$, have to be used. Some commercial ferromagnetic shields have maximum μ_{r} values up to 450 000 in the DC case [12, 13, 14, 15]: Permalloy, Co-Netic, MuMetal, ... These materials are magnetic alloys, which typically contain nickel (around 80%), iron (around 20%), and a small amount of other elements such as silicium, molybdenum, ...[16]. To obtain high μ_r values, it is often necessary to apply a thermal treatment (around 1000° C) to the shield, after it has been made. One aim of this treatment, which is generally carried out under a hydrogen atmosphere, is to obtain high purity materials. Because of the thermal treatment, the realization of ferromagnetic shields can be costly.

The second difficulty in using ferromagnetic materials for magnetic shielding arises from the saturation of the magnetization at $B \sim B_{\mathrm{sat}}$. Above B_{sat}, we have $\mathrm{d}B/\mathrm{d}H \cong \mu_0$, and the shielding capabilities of the material decrease. Typically, the maximum induction that can be efficiently shielded is much lower than 1 T. If one wants to shield magnetic inductions around 1 T or higher, the solution is to use concentric ferromagnetic screens: the screen near the magnetic source should have the highest saturation induction, whereas the shield near the region to protect should have the highest relative permeability.

The third intrinsic difficulty in using ferromagnetic shields is that their relative permeability decreases when the frequency of the applied field, f, increases. Generally, for materials with a high relative permeability under DC conditions, μ_r decreases to $\mu_r \cong 1$ if f is higher than ~ 1 kHz [1].

In the next section, we present another solution than ferromagnetic materials for magnetic shielding.

1.2 Magnetic shielding with high-temperature superconductors

From (1.1), we observe that SF is unchanged if μ_r is replaced by $1/\mu_r$. Hence, one can expect to reach high shielding efficiencies by using materials with $\mu_r \ll 1$. Then, the shielding mechanism is no longer the concentration of the magnetic flux in the shielding material, but its expulsion from the shield.

Traditional diamagnetic materials such as silver present relative permeabilities close to one, $\mu_r \lesssim 1$ [17]. Hence, the use of such materials would not be efficient to obtain high SF.

Besides their remarkable electric properties, superconducting materials have specific magnetic characteristics. A superconductor which is cooled below its critical temperature, T_c, expels the magnetic flux from its body. This diamagnetic property is due to macroscopic shielding currents flowing inside the material, which generate a magnetic field that opposes the applied field. This leads to a behaviour that is similar, but not completely equivalent, to that of a material with $\mu_r < 1$.

High-temperature superconductors (HTS) are superconducting ceramics with a critical temperature which can be higher than 77 K, the boiling point of liquid nitrogen. This allows one to cool down the material easily with small cost. If a low magnetic field is applied to the HTS below its critical temperature, no field enters the material beyond ~ 100 nm from the superconductor surface. Upon increasing the applied field, the magnetic field penetrates the material in the form of vortices. If the material is irreversible, these vortices are pinned near the boundaries of the superconductor, which then exhibits strong diamagnetic properties. Here, we propose to realize HTS shields using the property of vortex pinning.

As for ferromagnetic materials, HTS shields are characterized by different limitations which are discussed in the next chapters. First, the fabrication of efficient HTS shields is intricate since these materials are brittle ceramics. Second, such magnetic shields have to be used below T_{c} which is typically lower than 100 K. Third, the SF of a HTS shield depends upon the applied magnetic induction. Nevertheless, HTS are reported to shield a low frequency magnetic field more efficiently than ferromagnetic materials do [5]. As an example, a HTS film with a thickness of $\sim 40\ \mu$m attenuates a low frequency ($f = 103$ Hz) magnetic induction with a shielding factor higher than 120 dB if the induction to be shielded is lower than 0.1 mT [18].

1.3 Introduction to the geometric effects

We have seen that the SF of a screen depends upon the shielding material. Besides this dependence, the geometry also influences the shielding properties.

Any real specimen has finite dimensions. To draw the attention to the importance of the geometric effects, we consider the example of a ferromagnetic cylinder of finite length that is subjected to a uniform axial magnetic field $\mathbf{H}_{\mathrm{a}}$. Because of the applied field, the sample is magnetized. The magnetization, $\mathbf{M}$, is the source of an additional field, called demagnetizing field, $\mathbf{H}_{\mathrm{d}}$. The total magnetic field that the material experiences, $\mathbf{H}_{\mathrm{T}}$, is thus:

$$\mathbf{H}_{\mathrm{T}} = \mathbf{H}_{\mathrm{a}} + \mathbf{H}_{\mathrm{d}}. \tag{1.7}$$

The different fields are shown in figure 1.3.

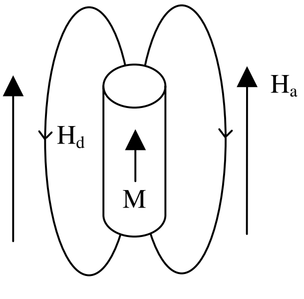

Figure 1.3: illustration of the demagnetizing field $\mathbf{H}_{\mathrm{d}}$ induced by the magnetization $\mathbf{M}$ of a ferromagnetic cylinder subjected to an axial uniform magnetic field $\mathbf{H}_{\mathrm{a}}$.

The field $\mathbf{H}_{\mathrm{d}}$ is always opposite to the sample magnetization, $\mathbf{M}$, and is related to it by the demagnetizing factor, $\tilde{\mathbf{N}}$:

$$\mathbf{H}_{\mathrm{d}} = -\tilde{\mathbf{N}}\mathbf{M}. \tag{1.8}$$

As we have assumed that the cylinder of figure 1.3 is ferromagnetic, $\mathbf{H}_{\mathrm{d}}$ is directed against $\mathbf{H}_{\mathrm{a}}$. In the general case, $\tilde{\mathbf{N}}$ is a tensor and is not uniform: $\tilde{\mathbf{N}} = \tilde{\mathbf{N}}(x, y, z)$. In MKS units, $0 \leq N_{\mathrm{ij}} \leq 1$.

If the specimen of figure 1.3 were an ellipsoid with uniform properties, the magnetization $\mathbf{M}$ and the demagnetizing factor $\tilde{\mathbf{N}}$ would be uniform inside the specimen [19, 20, 21, 22]. Furthermore, if $\mathbf{H}_{\mathrm{a}}$ were directed along one of the ellipsoid principal axes, one would have [19]:

$$H_\mathrm{T} = H_\mathrm{a} + H_\mathrm{d} = H_\mathrm{a} - NM = H_\mathrm{a} - N\chi H_\mathrm{T}, \tag{1.9}$$

where N is the uniform scalar demagnetizing factor and χ is the magnetic susceptibility, which is a scalar if the material is isotropic. Formulae giving N for ellipsoids of revolution can be found in [19]. When the specimen is not an ellipsoid, such formulae can nevertheless be used to have a rapid and first approximation of the geometric effects [19, 20]. Then the formulae are rather used for evaluating a volume averaged demagnetizing factor, $\langle N \rangle$.

Following this idea, we give some results which will be used later. If the specimen is a cubic sample, one generally takes

$$\langle N_\mathrm{x} \rangle = \langle N_\mathrm{y} \rangle = \langle N_\mathrm{z} \rangle \cong 1/3 \tag{1.10}$$

as $N_\mathrm{x} = N_\mathrm{y} = N_\mathrm{z} = 1/3$ for a uniformly magnetized sphere [19]. For a cylinder, with an applied field $\mathbf{H}_\mathrm{a}$ parallel to the $\hat{z}$-axis of revolution [19]:

$$\langle N_\mathrm{z} \rangle \rightarrow 0 \quad \texttt{if} \quad L \rightarrow \infty, \tag{1.11}$$

$$\langle N_\mathrm{z} \rangle \rightarrow 1 \quad \texttt{if} \quad L \rightarrow 0. \tag{1.12}$$

For the transverse case, i.e. $\mathbf{H}_\mathrm{a} \,||\, \hat{x} \perp \hat{z}$ [19],

$$\langle N_\mathrm{x} \rangle \rightarrow 0.5 \quad \texttt{if} \quad L \rightarrow \infty, \tag{1.13}$$

$$\langle N_\mathrm{x} \rangle \rightarrow 0 \quad \texttt{if} \quad L \rightarrow 0. \tag{1.14}$$

From (1.8) and (1.11)-(1.14), we see that the geometric effects are particularly important for samples presenting a large magnetization, as well as for those having a dimension along the direction of the applied field that is small compared to the other sample dimensions.

To illustrate the geometric effects, we consider the extreme example of the infinite ferromagnetic tube of section 1.1.1. We have seen that if a DC magnetic field is applied perpendicular to the tube axis, the specimen shields the internal cavity with a SF given by (1.1). Now, assume that the uniform magnetic field is applied parallel to the infinite tube axis. One can show [10, 23, 24] that there is no field attenuation at all, as for an infinite slab. That means that $H = H_\mathrm{a}$ everywhere and that $SF = 0$ dB. The shielding properties of the tube have changed only because of a different field geometry.

When the tube has a finite length, SF is not zero with an axial DC applied field because of demagnetizing effects. In a first approximation, the field attenuation is given by [23]:

$$SF = 20 \log \left(4 \langle N \rangle \; 10^{SF_\mathrm{trans}/20} + 1 \right), \tag{1.15}$$

where SF_trans is given by (1.1). The factor $\langle N \rangle$ is determined by assuming that the specimen is an ellipsoid with the same length to diameter ratio as the tube. If the length of the tube tends to infinity, one recovers $SF = 0$ as $\langle N \rangle = 0$.

We have presented the specificity of shielding a low frequency magnetic field, the traditional solution to shield such a field, and the possibility to use HTS to obtain high SF. Besides these features related to the material of the screen, we have also drawn the attention to the importance of geometric effects. The next section gives the objectives of this manuscript.

1.4 Aim of the thesis

This thesis aims at characterizing and modelling superconducting magnetic shields, more specifically shields made with high-temperature superconductors (HTS). As explained at the beginning of this chapter, this work is part of a larger project whose goal is to fabricate and design high-Tc magnetic screens that are capable of shielding volumes with linear dimensions of a few centimetres. Superconducting materials seem indeed to offer an interesting alternative to shield low frequency or DC magnetic fields, as higher shielding factors are reported than those obtained with ferromagnetic screens.

A characterization of the EPD samples was necessary to determine the best processing parameters, and to understand the physical properties of superconducting magnetic shields. Different experimental systems were used, and sometimes specifically designed for some shielding measurements. The realization of home-made experimental systems was necessary as commercial measurement systems are not available to determine the shielding factor of large superconducting samples of various geometries. Several difficulties are associated with the experimental study. HTS are superconducting only below a critical temperature which is typically lower than 100 K. Hence, the measurements have to be carried out in cryogenic environments. Besides, special care is needed when designing measurement systems used for superconducting or shielding characterizations due to the low level of signal. The field attenuation realized by a HTS shield is very strong ($SF > 60$ dB typically). To evaluate the shielding factor of such a screen, very sensitive measurement systems with small noise to signal ratios are needed.

In the past, different HTS magnetic shields have been studied, mainly experimentally [5, 25, 26, 27, 28, 29, 30, 31, 32, 33]. Generally, to characterize the shielding properties of a HTS screen, authors measure the evolution of the field inside a HTS cavity that is initially not magnetized, and is then subjected to increasing applied magnetic inductions. Below a threshold induction, called B_{lim}, the internal field remains close to zero. For higher applied inductions, the field penetrates the inner region and the internal induction increases with the applied field. In the literature, there is no widely accepted definition of the threshold induction, B_{lim}. In particular, the influence of geometric effects on B_{lim} is usually not discussed. Besides, there is no information concerning the geometrical volume over which a HTS shield of given size and shape can attenuate an external field below a given level. For the frequency response of a HTS shield, contradictory results are reported. Finally, the effects of defects, caps, and non-uniform superconducting properties on the shielding capabilities have not been studied. Here, we aim at studying these important properties experimentally and theoretically.

A theoretical study has two interesting features. First, with an adequate numerical tool, one can obtain interesting informations quickly and at low cost. Second, due to the many steps involved in fabricating superconducting shields, many effects can cause deviations from theory. These effects often act simultaneously, which makes data interpretation arduous. The theoretical results then serve as a reference, which allows one to investigate one effect at a time. The measured deviations can then be better interpreted, in order to optimize the process parameters.

1.5 Organization of the thesis

The thesis is organized as follows. In chapter 2, we present the phenomenon of superconductivity and give the classification of superconductors. For each type of superconductors, we emphasize their magnetic shielding properties and give some of their applications. At the end of this chapter, we introduce the Bean model which provides a simple description of the field penetration into irreversible type-II superconductors.

As our research project deals with high-temperature superconductors (HTS), we point out some features of these materials in chapter 3. This allows one to better understand the difficulties associated to the realization of such a shield. We also give an illustrative experimental result showing the magnetic shielding properties of HTS. We end the chapter with a description of the electrophoretic deposition (EPD) technique.

The limitations of the Bean model are discussed in chapter 4. To take into account the geometric effects, and the current voltage relation of HTS, other methods have to be used. In particular, we present in section 4.5.1 the numerical method of Brandt, which we used to study the field penetration into superconducting tubes of finite length.

The first results are given in chapter 5, which concerns planar samples. An emphasis is placed on the superconducting properties of coatings made by the EPD technique. The influence of the metallic substrate on the superconducting properties of the HTS film is also discussed. At the end of the chapter, we present a shielding measurement made with an EPD planar sample.

Chapter 6 presents experimental and theoretical results of the magnetic shielding properties of HTS open tubes. The field is applied either parallel or perpendicular to the tube axis. The experimental part is realized by using a commercial and an EPD tube. The theoretical results are obtained by using numerical simulations based on the Brandt method. When the field is applied parallel to the tube axis, these results allow us to point out several factors which determine the quality of a shield: the maximum field which can be shielded, the volume over which the attenuation is higher than a given level, and the frequency response of a HTS shield. A comparison of the field attenuation realized in the case of an axial or transverse field clearly shows the importance of the geometric effects.

Chapter 7 is devoted to numerical results obtained with the method of Brandt. Assuming that the field is applied parallel to the axis of tubular samples, we evaluate the shielding properties of a closed tube, of stacked tubes, and of tubes with non-uniform superconducting properties along the axis.

We conclude and give outlook in chapter 8.

Chapter 2

Magnetic properties of superconductors

In chapter 1, we saw that shielding low frequency or DC magnetic fields is not obvious. When superconductors are cooled below their critical temperature, they exhibit strong diamagnetic properties. One can thus expect to obtain high field attenuations with superconducting shields. Superconductors have other interesting properties, which, over since superconductivity was discovered at the beginning of the twentieth century, have been exploited in applications.

The magnetic shielding properties of superconductors are unique: they result from macroscopic currents flowing inside the material and which oppose the applied field. All superconductors do not have the same magnetic properties. Two major categories can be distinguished: type-I and type-II superconductors.

In this chapter, we explain the magnetic shielding properties of superconductors. First, we give some important dates and the main features of superconductivity. In section 2.2, we show that there are two other parameters than the critical temperature that determine whether the material is superconductor or normal. Because of their specific properties, superconductors are used in various applications. We give some of them in section 2.3. Afterwards, we detail the magnetic properties of type-I and type-II superconductors (section 2.4). For each type, we also study the possibility to use these materials to make a magnetic shield. Our research project aims at using irreversible type-II superconductors to attenuate a magnetic field. We explain the peculiarities of these materials in section 2.5. We finally introduce the Bean model, which allows one to have a first approximation of the field distribution in an irreversible type-II shield, assuming that the demagnetizing field is zero (no geometric effects).

2.1 History and basic features of superconductivity

The phenomenon of superconductivity is the name given to a combination of remarkable electric and magnetic properties that arise when certain materials are cooled below a given temperature, called the critical temperature, T_c. For all known superconductors, this temperature is lower than 150 K under normal pressure. Hence, the history of superconductivity is intimately linked to the history of cryogenic technology.

In 1908, Heike Kamerlingh Onnes, from the University of Leiden, first succeeded in liquefying helium whose boiling point is 4.2 K. This discovery gave the possibility to perform new experiments in low, stable temperature environments, by immersing the studied samples in a liquid helium bath. One of the first investigations that Onnes carried out in the newly available low temperature range was the study of the dependence of the electrical resistance of metals with temperature.

In 1911, Onnes asked an assistant, Gilles Holst, to measure the resistance of mercury immersed in a helium bath. He found that at very low temperatures, the resistance became immeasurably small, and that the manner in which the resistance decreases was completely unexpected. Figure 2.1 shows the original resistance measurement. We see that the resistance falls sharply at approximately 4.2 K. Below this temperature, the resistance becomes zero, within the limits of experimental accuracy.

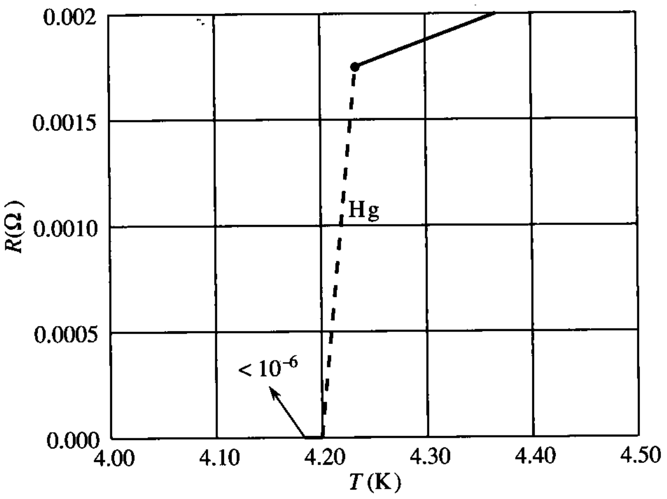

Figure 2.1: resistance of a mercury sample versus temperature (from [34]).

Onnes stated that below 4.2 K, mercury passes into a new state, with electrical properties quite unlike those previously known, and called this state the superconducting state. The temperature below which the metal presents zero resistance was called the critical temperature T_c.

After Onnes' discovery, it was found that superconductivity is not a rare phenomenon: over three dozen of elements display superconductivity. The critical temperature of superconducting elements, T_c, ranges from 0.01 K for tungsten to 9.3 K for niobium. Note that the best conductors at room temperature, such as copper, silver, gold, are not superconductors.

In 1933, W. Meissner and R. Ochsenfeld found that superconductors had specific magnetic properties besides their remarkable electric feature. Below T_c, Meissner and Ochsenfeld observed that lead and tin seek to maintain the local magnetic induction at $B = 0$ within their volume [35]. In contrast to a perfect conductor which would only expel a flux variation, superconducting elements expel the magnetic flux itself. This effect, which distinguishes a superconductor from a perfect conductor, is known as the Meissner effect.

Some metallic alloys are also superconductors. They can have higher T_c values than superconducting elements. As an example, $T_c = 18$ K for Nb_3Sn. Besides, it was found that the metallic compounds have magnetic properties in the superconducting state that differ from those of tin or lead. At low applied field, the metallic alloys totally expel the magnetic flux as the elements do, and one recovers the Meissner state. But as the applied field increases, it can enter the superconducting compound in the form of vortices, each vortex carrying a single flux quantum. If vortices can move freely, the material is called reversible. If the material presents defects, impurities, ... which can pin the vortices, the material is termed irreversible. In this case, it is possible to prevent flux from penetrating all the material. Moreover, after switching off the applied field, an irreversible material presents a remnant magnetic moment because of vortex pinning.

Before 1986, the superconductor with the highest known critical temperature was Nb_3Ge ($T_c = 23.2$ K), which had been discovered in 1971. By the end of 1986, K. Alex Müller and J. Georg Bednorz (IBM research laboratory, Zürich) discovered superconductivity above 30 K for the lanthanum-based cuprate perovskite material, La-Ba-Cu-O [36]. Müller and Bednorz' discovery triggered an intense activity in the field of superconductivity. Researchers around the world began making ceramics of every imaginable combination in a quest for higher critical temperatures. In 1987, Paul C. W. Chu and Maw-Kuen Wu (Houston and Huntsville) were the first to find a superconducting material whose critical temperature was high enough to be cooled by liquid nitrogen, which boils at 77 K [37]. They showed that $YBa_2Cu_3O_7$ (generally named Y-123) had a critical temperature near 92 K. Later, other superconducting compounds having a critical temperature higher than 77 K were discovered. All this compounds are characterized by layers of copper oxides. These materials are known as cuprates or as high-temperature superconductors (HTS), while the others are called low-temperature superconductors (LTS). There is no widely-accepted temperature that separates HTS from LTS. However, all the superconductors known before the 1986 discovery are called LTS (or conventional superconductors).

In 2001, a material that had been sitting on laboratory shelves for decades was found to be a superconductor. Japanese researchers measured the transition temperature of magnesium diboride (MgB_2) at 39 K [38], far above the highest T_c of any of the elemental or binary alloy superconductors. Figure 2.2 shows the evolution of the critical temperature of various materials.

Besides the critical temperature, there are two other parameters which characterize a superconductor. They are defined in the next section.

2.2 Three critical values

In 1913, Onnes discovered that besides T_c, there exists a maximum current density, J_c, that can flow in a superconductor before it reverts to the normal state. The critical current density, J_c, was found to increase as the temperature of the super-

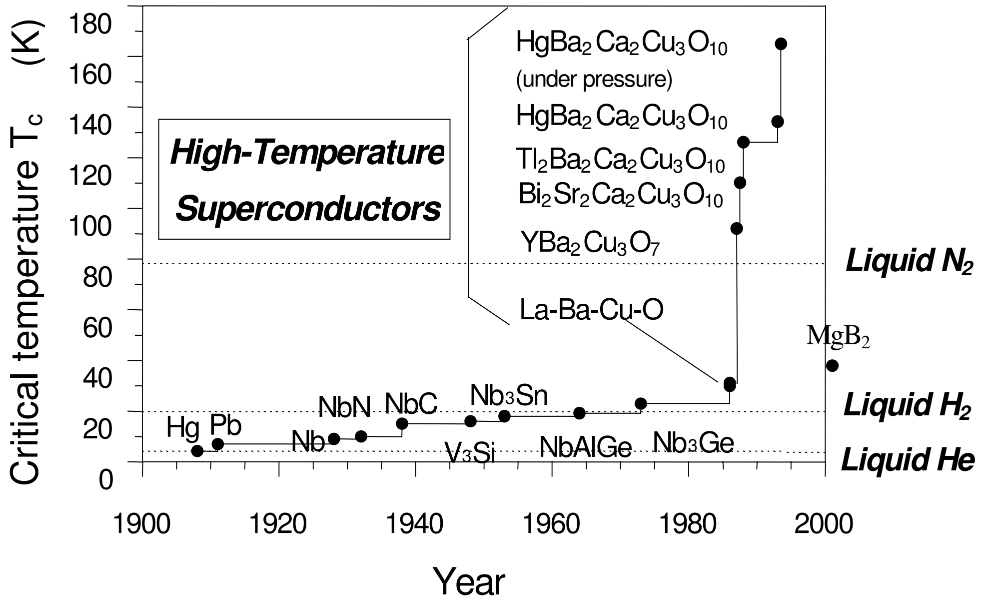

Figure 2.2: evolution of the critical temperature of superconductors (from [20]).

conductor was lowered. In 1914, Onnes reported that an applied magnetic field can also destroy superconductivity. The value of the field necessary to destroy superconductivity, called the critical magnetic field, H_c, also increases as the temperature decreases.

Hence, a superconductor is characterized by the critical surface shown schematically in figure 2.3. The surface, with H_c, T_c, and J_c intercepts, separates the normal and superconducting states: the material is superconductor below this surface.

Before clarifying the magnetic properties of the superconductors, we present some of their applications.

2.3 Some applications of superconductors

Because of their remarkable electric and magnetic properties, superconductors are used in different applications.

A great commercial opportunity for superconductors is in electric power applications, such as cables, motors, generators, transformers, ... As superconductors present a very small resistance to current flow, they can be used for electric energy transport with improved efficiency. But the greatest advantage of using superconductors in power applications is that they can carry a much higher current density than a traditional wire. As an example, $J_{\max} \cong 10^3$ A/cm^2 for a copper wire at 300 K whereas one can reach $J_c \geq 10^4$ A/cm^2 for a HTS cable at 77 K [39]. This last value is evaluated in self field, which means that no magnetic field is applied to the superconducting cable. This increase of admissible current density leads to lighter and more compact transformers, benefits that are particularly useful for mobile systems

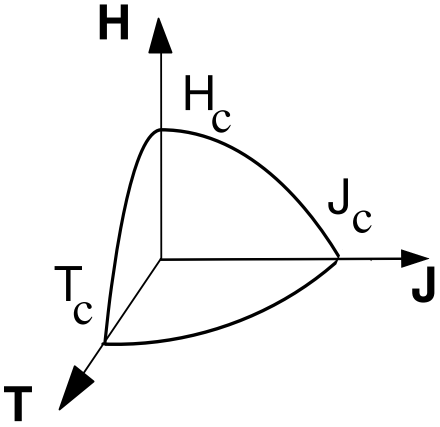

Figure 2.3: critical surface delimiting the normal (above the surface) and the superconducting states (below the surface).

such as trains.

As a large current can flow in a superconducting cable, high magnetic fields can be produced with superconducting coils. As an example, magnetic inductions up to 5 T are now commonly produced with superconducting wires for medical imaging. High magnetic fields also enable one to design compact rotating machines, which could be very useful for ship propulsion [40]. Such a project is currently investigated by the American Navy.

Above J_c, superconductors switch from the superconducting to the normal, resistive state. One can take advantage of this property to build very rapid fault-current limiters which protect the grid from short circuit. When the current rises above J_c, the superconductor becomes resistive, strongly reducing the current in the grid. The main advantage of a superconducting fault-current limiter with respect to conventional breakers resides in its short response time, typically 1 ms against 30 ms for conventional ones.

As said earlier in section 2.1, one can trap a magnetic induction in some superconductors by pinning the vortices. The remnant magnetization increases with the size of the superconductor [34]. Hence, it is possible to obtain a bulk monolith with a much higher magnetic induction than a classical magnet. One can use such superconducting bulks in rotating machines. The pinning of vortices can also be used to obtain a stable levitation [41], for instance to make flywheel systems which store energy in the form of kinetic energy. Because of the low losses, a levitating body can conserve a rotating movement during a long time. Levitating trains have also been built to reduce friction losses. High speeds (up to 580 km/h) can be achieved with such systems.

Thin film superconducting filters can provide enhanced network coverage and capacity in wireless communications [40]. One reason is that ultra-narrow band filters can be made with superconducting films. Moreover, highly selective filters require a large number of coupled resonators. Such a construction is possible with superconducting films because of their low surface resistance. Very high quality HTS films can have a surface resistance at 1 GHz and 77 K of about 2 $\mu\Omega$, that is about 10^4 times lower than the surface resistance of copper films [40].

Very sensitive magnetic sensors can be made with superconductors. Theoretically, a superconducting quantum interference device (SQUID) allows one to detect magnetic inductions down to 10^{-15} T. A SQUID consists of a superconducting loop with two Josephson junctions. Such a junction is composed of a thin layer of insulating material sandwiched between two superconducting layers.

Superconductors can also be used to shield a low frequency magnetic field, as we now discuss in detail.

2.4 Type-I versus type-II superconductors

In section 2.1, we mentioned that ceramic superconductors discovered after 1986 are called high-temperature superconductors (HTS). The others, which include elements and metallic alloys, are qualified as low-temperature superconductors (LTS). Besides that distinction that one can make between HTS and LTS, as a function of the critical temperature, one can also distinguish superconductors on the basis of their magnetic properties. One is thus led to consider type-I and type-II materials. In this section, we recall their main magnetic properties and consider their relevance for shielding applications.

Here, we do not discuss the geometric effects introduced in section 1.3. We rather focus on the intrinsic shielding properties of superconducting materials. Hence, in this section, when studying the possibility to use a superconductor to make a magnetic shield, we consider infinitely long tubes in a uniform axial magnetic field. From (1.11), the demagnetizing field then tends to zero.

2.4.1 Type-I superconductors

Type-I and type-II superconductors have different magnetic properties, what can best be seen by considering the intersection of the critical surface of figure 2.3 with the $J = 0$ plane (see figure 2.4). Type-I superconductors are characterized by one critical magnetic field, H_{c}. Below the curve $H_{\mathrm{c}}(T)$ depicted in figure 2.4, the material is superconducting and in the Meissner state: $\mathbf{B} = 0$. For this reason, superconductors in the Meissner state are sometimes termed perfect diamagnets. Above the $H_{\mathrm{c}}(T)$ curve, the material is in the normal state.

All type-I superconductors are pure metals and the maximum critical temperature is below 10 K. At 0 K, $\mu_0 H_{\mathrm{c}} \cong 100$ mT, typically. Such a low value is the main limitation for the applications and type-I superconductors are generally not used for current transport. They are sometimes used in Josephson junctions and in shielding applications.

In the next paragraph, we present the London equations which characterize the electromagnetic behaviour of type-I superconductors.

London equations

In 1934, Gorter and Kasimir proposed the two-fluid model inspired by thermodynamic arguments to describe the electric and magnetic features of the supercon-

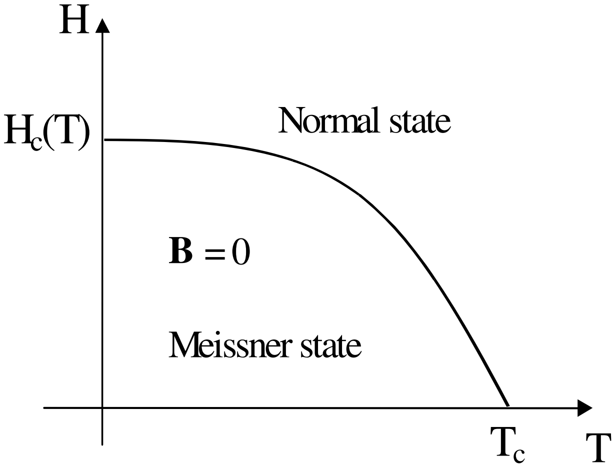

Figure 2.4: phase diagram of a type-I superconductor in the $J = 0$ plane.

ducting state. According to this model, the current in a superconductor is carried by two types of electrons: the super-electrons, of density n_s, which move freely in the crystal lattice, and the normal electrons, of density n_n, whose motion induces an electric resistivity. The density of the super-electrons increases as temperature decreases, following the law:

$$n_\mathrm{s}(T) = n_0 \left[1 - \left(\frac{T}{T_\mathrm{c}} \right)^4 \right], \tag{2.1}$$

where n_0 is the density of super-electrons at 0 K[1]. In 1935, F. and H. London proposed two important equations [42], now known as the London laws, in order to account for both zero-resistivity and the Meissner effect. The first and second London laws are:

$$\begin{aligned} \mathbf{E} &= \frac{\partial}{\partial t} (\Lambda \mathbf{J}), && (2.2) \\ \nabla \times (\Lambda \mathbf{J}) &= -\mathbf{B}, && (2.3) \end{aligned}$$

with

$$\Lambda = \frac{m}{n_\mathrm{s} e^2}, \tag{2.4}$$

where m and e denote the effective mass and charge of the superconducting charge carriers. These laws were not deduced from fundamental considerations and do not explain superconductivity. However, they lead to electric and magnetic characteristics which agree with the experimental results.

The first London law (2.2) shows that no dissipation occurs when a static current density flows through a superconductor. On the opposite, time-varying currents lead to a non-zero electric field. Such a property can be found with the two-fluid model [43]. A constant current is carried only by the super-electrons. For time varying currents, a part is carried by the normal electrons, which leads to dissipation.

---

[1] In 1957, Bardeen, Cooper, and Schrieffer found that super-electrons are in fact pairs of electrons, called Cooper pairs, interacting through the exchange of phonons (BCS theory).

The second London law (2.3) describes the Meissner effect. Introducing the Maxwell equation

$$\nabla \times \mathbf{B} = \mu_0 \mathbf{J}, \tag{2.5}$$

in (2.3), one obtains:

$$\nabla^2 \mathbf{B} = \frac{1}{\lambda^2}\mathbf{B}, \tag{2.6}$$

where

$$\lambda = \sqrt{\frac{\Lambda}{\mu_0}}, \tag{2.7}$$

is called the London penetration depth.

To understand the important consequences of equation (2.6), consider that a uniform magnetic induction $\mathbf{B}_\mathrm{a} = B_\mathrm{a}\,\hat{z}$ is applied parallel to the surface of a type-I superconductor, that has an infinite extension in the y and z directions, as shown in figure 2.5. Then the solution of (2.6), which is plotted in figure 2.5(b), is given by:

$$B(x)\,\hat{z} = B_\mathrm{a}\,\mathrm{e}^{-x/\lambda}\,\hat{z}. \tag{2.8}$$

The magnetic flux density decreases as an exponential as one moves into the material and the London penetration depth, λ, is the characteristic length of decay of magnetic flux within the superconductor. From (2.5), this spatial variation of flux density is accompanied by currents flowing near the surface of the material, which shield the external applied field. Hence, superconductors oppose the penetration of magnetic flux, in contrast with traditional conducting materials, which only oppose a variation of magnetic flux.

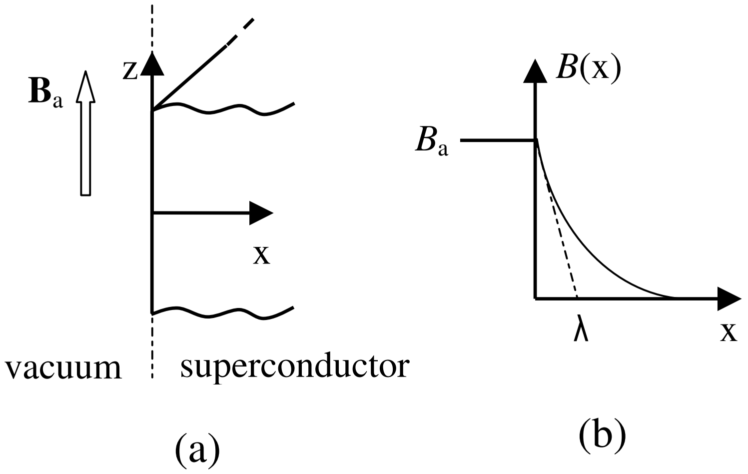

Figure 2.5: illustration of the second London law. Figure (a): geometry used to solve equation (2.6): type-I body only limited along the x-axis (semi-infinite along the x-axis). Figure (b): solution of (2.6) for the geometry of figure (a).

The surface layer where the screening currents flow is very thin. Indeed, λ lies around 60 nm for type-I superconductors at 0 K [34]. Equation (2.1) leads to the following temperature dependence:

$$\lambda(T) = \lambda(0)\left[1 - \left(\frac{T}{T_\mathrm{c}}\right)^4\right]^{-1/2}. \tag{2.9}$$

We deduce $\lambda \cong 100$ nm at $T = 0.9\ T_\mathrm{c}$ if $\lambda(0) = 60$ nm. Hence, for large superconducting samples (larger than 1 mm), the penetration of magnetic flux can be neglected. On the contrary, for small samples (around 100 nm), such as powder particles or thin films, flux penetration can be significant and has to be taken into account.

Reversible properties of type-I superconductors

We now present the evolution of the average magnetic induction, $\langle B\rangle$, with respect to the applied induction, B_a.

Consider an infinitely long type-I cylinder, whose diameter is much larger than the London penetration depth. The cylinder is subjected to a uniform axial magnetic induction B_a, see figure 2.6 (a). The average quantity $\langle B\rangle$ is defined by:

$$\langle B\rangle = \frac{1}{V}\int_V B(x,y,z)\mathrm{d}x\,\mathrm{d}y\,\mathrm{d}z = \frac{1}{S}\int_S B(x,y)\mathrm{d}x\,\mathrm{d}y, \tag{2.10}$$

where V is the volume of the superconductor, and S is the surface of the cross-section of the cylinder. The last equality of (2.10) holds when the cylinder is infinitely long. Figure 2.6 (b) shows the evolution of $\langle B\rangle$ with B_a.

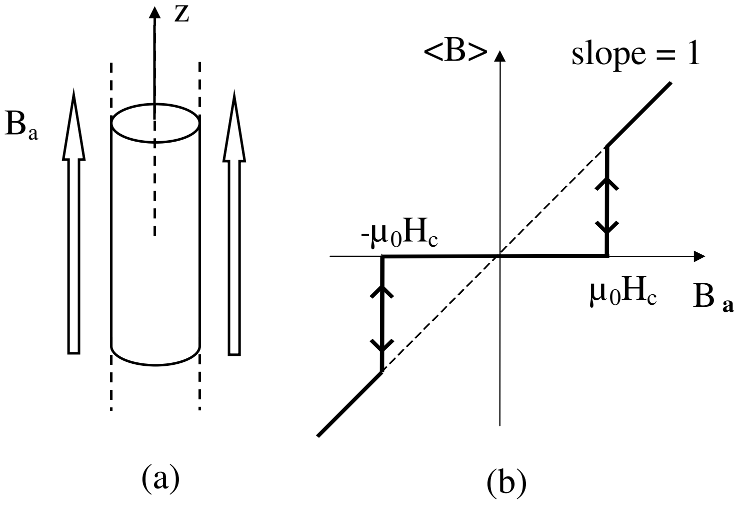

Figure 2.6: figure (a): infinitely long type-I superconducting cylinder in a uniform axial magnetic induction. Figure (b): evolution of the corresponding averaged magnetic induction, as a function of the applied magnetic induction.

Below $B_\mathrm{a} = \mu_0 H_\mathrm{c}$, $\langle B\rangle$ remains zero as surface Meissner currents shield the applied induction inside the superconductor. For higher applied inductions, the material is no longer superconducting and $\langle B\rangle = B_\mathrm{a}$. As shown in figure 2.6 (b), the magnetic behaviour is reversible: $\langle B \rangle$ only depends upon the value of B_a, and not upon the history of the applied induction. In particular, when decreasing B_a to zero, there is no remnant magnetic induction.

Due to the diamagnetic property below H_c, type-I superconductors seem adequate for making magnetic shields. In the next paragraph, we show that the cooling procedure of a type-I superconductor is of significant importance if one wants to use such a material for magnetic shielding.

Shielding with type-I superconductors

When cooling a superconductor below its critical temperature, there are two possibilities. Either the superconductor is cooled without any applied magnetic field, or the material is cooled in the presence of a magnetic field. In the first case, the material is said to be in zero-field cooled conditions, ZFC. In the second case, the material is in field cooled conditions (FC).

For shielding applications, one needs a cavity. Hence, consider a type-I superconducting tube (figure 2.7). We suppose that the tube is infinitely long, $\ell \to \infty$, and that the thickness of the wall, $d = a_2 - a_1$, is much larger than λ. Were are going to apply to this tube a static magnetic induction before and after cooling the sample, and evaluate the resulting induction in the hollow of the tube.

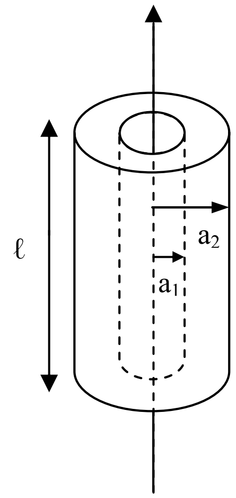

Figure 2.7: type-I tube with $\ell \to \infty$ and $a_2 - a_1 \gg \lambda$.

The field in the hollow of the tube can be deduced from classical electromagnetic laws. Faraday's law gives:

$$\oint_C \mathbf{E} \bullet d\mathbf{l} = -\frac{d}{dt} \int_S \mathbf{B} \bullet d\mathbf{s}, \tag{2.11}$$

where S is the surface delimited by the contour curve C. Equation (2.11) means that the temporal variation of magnetic flux through any surface is equal to the contour integral of the electric field along the curve delimiting this surface. As $\mathbf{E} = 0$ and $\mathbf{B} = 0$ within the superconducting material (we neglect the penetration depth), (2.11) implies that the total flux threading the tube hole is constant in time. From this result, we can now evaluate the magnetic field in the hole of a type-I tube, both in ZFC and FC conditions.

First, consider the ZFC case: the hollow cylinder of figure 2.7 is cooled below its critical temperature T_c, with no applied field. Afterwards, we apply a static magnetic induction parallel to the tube axis. Induced currents then flow on the outer surface of the tube to prevent field penetration into the superconducting material, but also to prevent field penetration in the hole, as the total flux must remain zero. The resulting situation is illustrated in figure 2.8(a). There is no field in the hole.

Second, consider the tube cooled below T_c in the presence of an axial magnetic induction (FC case). As in the ZFC case, a surface current flows on the outer surface to expel magnetic flux from the superconducting material. But such a current also cancels the flux threading the hole, which must remain constant. As a result, an equal and opposite surface current develops on the inner surface of the tube to maintain a constant flux. The resulting field distribution is illustrated in figure 2.8(b). The magnetic induction inside the cavity is equal to the applied one. Hence, a type-I tube can be used to shield a region from an external field, but only in the ZFC case.

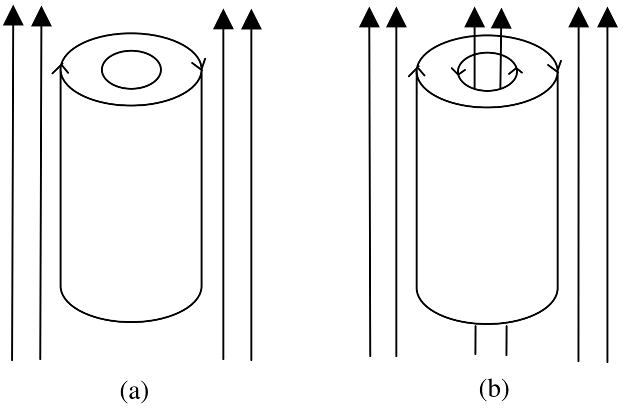

Figure 2.8: field distribution in a type-I superconducting tube subjected to a uniform axial magnetic induction. When the tube is cooled before applying the field (ZFC), figure (a), surface currents flow along the outer surface of the tube only, in the direction given by the arrows. When the magnetic induction is applied before cooling the tube (FC), figure (b), surface currents flow both along the outer and the inner surface, in opposite directions. The cavity is shielded only in the ZFC case.

Following this idea, some people used type-I superconductors to make magnetic shields, see for instance [44] in which lead cylinders are cooled at 4.2 K. As all type-I superconductors have a critical temperature lower than 10 K, very low temperatures are needed when using these materials. Fortunately, some type-II superconductors have a much higher T_c.

2.4.2 Type-II superconductors

Type-II superconductors are mainly composed of metallic alloys and ceramic superconductors (HTS). The critical temperature of type-II superconductors can be much larger than that of type-I superconductors. The phase diagram of a type-II superconductor in the $J = 0$ plane is shown in figure 2.9. Here, in contrast with type-I superconductors, we observe two curves $H_{c1}(T)$ and $H_{c2}(T)$.

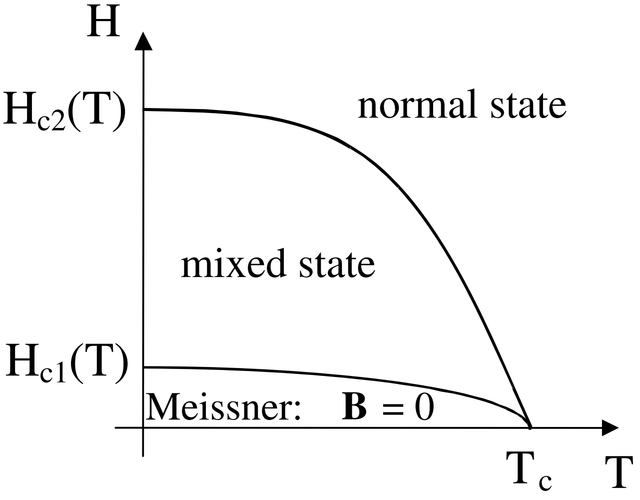

Figure 2.9: phase diagram of a type-II superconductor in the $J = 0$ plane.

If $H < H_{c1}(T)$, the material is in the Meissner state as a type-I superconductor. Hence, $\mathbf{B} = 0$ inside the body, at a distance from the surface larger than λ. The London depth, λ, can be much larger for type-II than for type-I superconductors. At 0 K, it typically lies between 90 to 500 nm [34]. If $H_{c1}(T) < H < H_{c2}(T)$, the material remains superconducting, but magnetic flux penetrates the material in the form of vortices. For higher magnetic fields, $H > H_{c2}(T)$, the material is in the normal state.

Since type-II superconductors remain superconducting in much higher fields and at higher temperatures than type-I materials, they are much more often used in applications. For instance, at 0 K, $\mu_0 H_{c1} = 0.1$ T and $\mu_0 H_{c2} = 22$ T for Nb_3Sn. For HTS, $\mu_0 H_{c1} = 1 - 10$ mT and $\mu_0 H_{c2} > 100$ T at 0 K. Hence, most applications of type-II superconductors deal with materials in the mixed state.

When $H > H_{c1}$, vortices penetrate a type-II superconductor if they can overcome a surface barrier. Vortices consist of a normal core, whose radius ξ is called the coherence length. In reality, the boundary between normal core and superconducting regions is not sharply defined: the transition is spread out over a distance roughly equal to the coherence length, ξ, as shown in figure 2.10. The coherence length varies between few nanometres for HTS, to 0.1 μm for other compounds. Each vortex carries the same magnetic flux, $\Phi_0 = h/2e \cong 2 * 10^{-15}$ Wb (h is the Planck constant, and e is the electron charge). When H increases between H_{c1} and H_{c2}, the number of vortices increases. In addition to the surface current shielding the applied field as discussed in section 2.4.1 for type-I superconductors, there exist supercurrents around each vortex. These supercurrents circulate in a zone whose extension is roughly equal to the penetration depth, λ, and in opposite direction to the diamagnetic surface current (see figure 2.10).

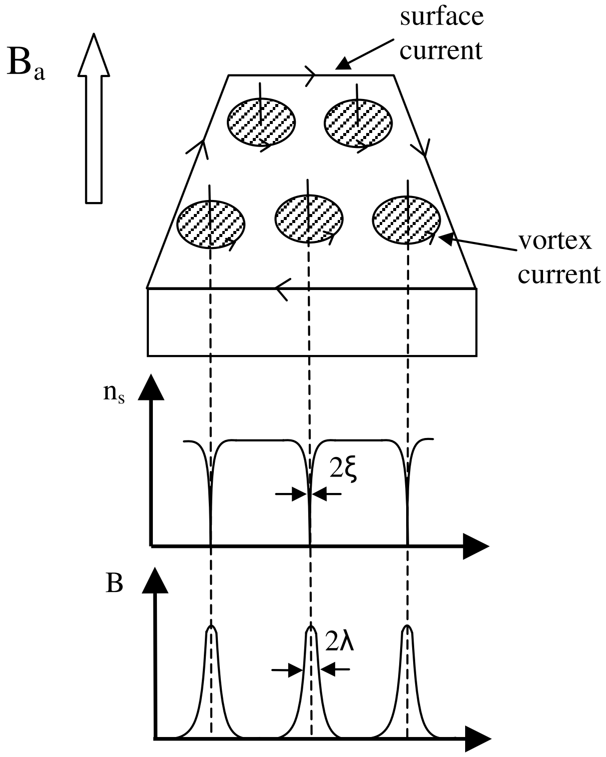

Figure 2.10: mixed state in a type-II superconductor. From top to bottom : lattice of vortices, spatial variation of the concentration of super-electrons, and spatial variation of flux density.

Two vortices repel each other, similarly to the repulsion between two parallel solenoids or two parallel magnets. There are also the surface barriers which tend to maintain vortices inside the material. If vortices move freely in the material (no pinning), Abrikosov predicted that they arrange themselves in a regular hexagonal pattern at equilibrium [45]. Vortices have been first observed experimentally in 1967 by U. Essmann and H. Trauble (Stuttgart) with the bitter decoration technique in niobium and in a lead-indium alloy [46]. Since then, the Abrikosov pattern has been observed with many other techniques (scanning tunnelling microscopy, Lorentz microscopy, magnetic force microscopy, scanning squid microscopy, scanning Hall probe, magneto-optical imaging).[2]

Reversible type-II superconductors

We now present the macroscopic magnetic properties of type-II superconductors when vortices move freely. Such materials are called reversible type-II superconductors. In what follows, we neglect the surface barriers.

---

[2] Pictures of the Abrikosov pattern observed by different techniques can be viewed at http://www.fys.uio.no/super/vortex/index.html.

We consider an infinitely long type-II reversible cylinder, whose diameter is much larger than the London penetration depth. When applying a uniform magnetic induction parallel to the cylinder axis, the average magnetic induction, $\langle B \rangle$, defined by (2.10), follows the curve of figure 2.11(b).

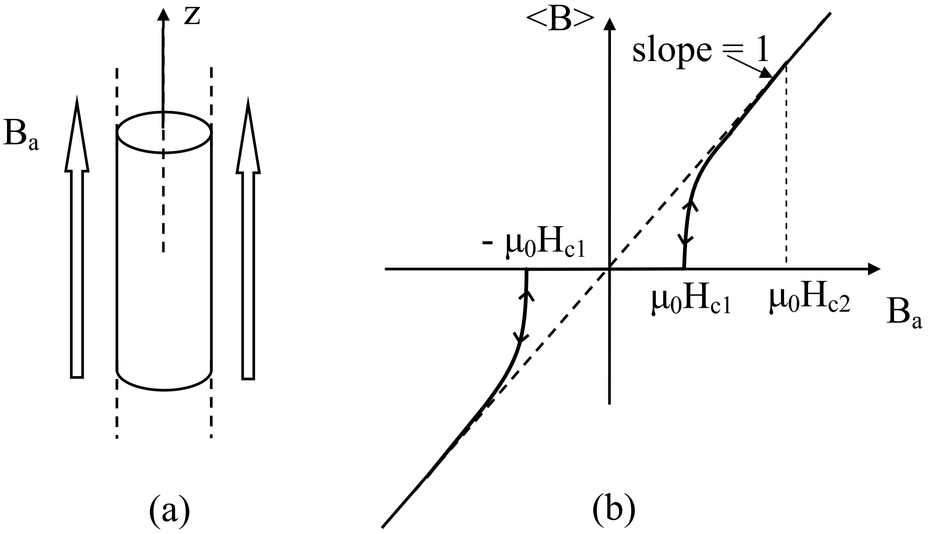

Figure 2.11: infinite type-II reversible cylinder in a uniform axial magnetic induction (figure (a)), and evolution of the corresponding averaged magnetic induction, as a function of the applied magnetic induction (figure (b)).

Below $B_{\mathrm{a}} = \mu_0 H_{\mathrm{c1}}$, the magnetic flux density remains zero, as the superconductor is in the Meissner state. Above $\mu_0 H_{\mathrm{c1}}$, vortices start penetrating the superconductor, and $\langle B \rangle$ increases. At $B_{\mathrm{a}} = \mu_0 H_{\mathrm{c2}}$, the material is no longer superconducting. Reducing the applied field, the magnetic induction follows the same curve as the initial one, since vortices move freely in the material. Hence, the magnetic induction only depends upon the applied field, and not upon its history.

If vortices move freely, a DC current cannot flow without loss in a type-II superconductor in the mixed state. Consider a type-II superconductor carrying a current density $\mathbf{J}$, and subjected to a magnetic induction $\mathbf{B} \perp \mathbf{J}$, with $|\mathbf{B}| > \mu_0 H_{\mathrm{c1}}$. Then a force acts on the vortex lattice, which is given by:

$$\mathbf{F}_{\mathrm{L}} = \mathbf{J} \times \mathbf{B}. \tag{2.12}$$

The force $\mathbf{F}_{\mathrm{L}}$ is called the Lorentz force. If the material is reversible, vortices move in the direction of $\mathbf{F}_{\mathrm{L}}$. Because of this displacement, there is an electric field $\mathbf{E} = \mathbf{B} \times \mathbf{v}$ which is parallel to $\mathbf{J}$ ($\mathbf{v}$ is the flux line velocity), hence an energy dissipation. Because of this dissipation, there is no interest to use reversible type-II superconductors for transport applications.

We now study the possibility to use reversible type-II superconductors for shielding applications.

Shielding with reversible type-II superconductors

Consider an infinite reversible type-II superconducting tube cooled in ZFC conditions. We assume that the thickness of the tube is much larger than the London depth, λ. Once the tube is below its critical temperature, we apply an increasing uniform axial magnetic induction, B_{a}. When $B_{\mathrm{a}} < \mu_0 H_{\mathrm{c1}}$, we recover the situation explained in section 2.4.1 for a type-I superconducting tube. Because of the Meissner currents flowing along the outer diameter of the tube, the magnetic induction in the hollow of the tube is zero. When $\mu_0 H_{\mathrm{c1}} < B_{\mathrm{a}} < \mu_0 H_{\mathrm{c2}}$, vortices enter the material. Due to their displacement as B_{a} is increased, a non-zero electric field appears inside the material. Hence, in contrast with the situation for which $B_{\mathrm{a}} < \mu_0 H_{\mathrm{c1}}$, the magnetic flux through the cavity of the tube can rise without violating (2.11). Thus, in the ZFC case, the tube no longer shields the cavity for $B_{\mathrm{a}} > \mu_0 H_{\mathrm{c1}}$ in the reversible case. But H_{c1} is small, typically $\mu_0 H_{\mathrm{c1}} \cong 1$ mT for HTS at 0 K. Hence, the shielding properties of a type-II reversible tube are poor.

In practice however, vortices cannot move freely in the superconductor because of the existence of defects, impurities, which act as pinning sites. Then higher magnetic inductions can be shielded with type-II superconductors. In the next section, we present the magnetic properties of type-II superconductors for which vortices are pinned.

2.5 Irreversible type-II superconductors

Every material contains lattice defects, impurities, ... If the size of these defects is comparable to the coherence length, ξ, they can act as pinning centres for vortices. The resulting macroscopic force which acts on the vortex lattice is called the pinning force, $\mathbf{F}_{\mathrm{P}}$. A type-II superconductor for which vortices cannot move freely is termed irreversible. Because of the pinning force, the spatial distribution of vortices in an irreversible material is expected to strongly differ from the equilibrium Abrikosov lattice of reversible type-II superconductors. In 1964, Bean introduced a model [47, 48], now kown as the Bean critical state model, which gives the vortex distribution in a material with strong pinning. We present this model in the next section, since it allows one to have a rapid approximation of the field distribution in an irreversible type-II superconductor for which the demagnetizing field is small.

2.5.1 Bean model

Bean proposed a model to calculate the internal magnetic induction of an irreversible type-II superconductor, $\mathbf{B} = \mu_0 \mathbf{H}$, as a function of the position inside the material, and as a function of the applied magnetic induction, $\mathbf{B}_{\mathrm{a}}$. Here, the local magnetic induction, $\mathbf{B}$, represents an average flux density over several vortices. The basis of Bean's theory is that there exists a limiting macroscopic superconducting current density, J_{c}, that the superconductor can carry; furthermore, any electromotive force, however small, induces this current to flow locally. This electromotive force is induced by the variation of the local magnetic induction, $\mathbf{B}$. Hence, the relation between the magnitude of the electric field, E, and the magnitude of the current density, J, is the one shown in figure 2.12. If $J < J_c$, the electric field is zero, and $E \to \infty$ if $J > J_c$.

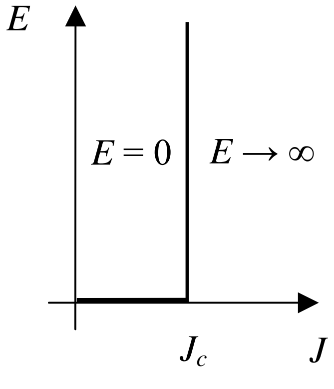

Figure 2.12: $E-J$ curve of an irreversible type-II superconductor in the Bean model.

Suppose that a type-II superconductor with strong pinning has been cooled in ZFC conditions, and is subjected to a magnetic induction $B_a > \mu_0 H_{c1}$. Following Bean's idea, only two states of current flow are possible: zero current for the regions that have never felt the magnetic field, and currents of magnitude J_c for the other regions. The direction of these currents depends upon the direction of the electromotive force that was induced by the local change of the magnetic field. The two states introduced by Bean can be summarized by the following equation, which is derived from Ampere's law:

$$\nabla \times \mathbf{B} = \mu_0 \mathbf{J}_c \quad \texttt{or} \quad 0. \tag{2.13}$$

To better understand the field distribution proposed by Bean, consider the infinitely long tube in the uniform axial magnetic induction of figure 2.13. The thickness of the tube is $d = a_2 - a_1 \gg \lambda$. For such a tube, the demagnetizing field, $\mathbf{H}_D$, is zero. The condition $\mathbf{H}_D = 0$ is the first assumption of the Bean model. He further supposed that the type-II superconductor is characterized by $H_{c1} = 0$, $H_{c2} \to \infty$, and by a critical current density, J_c, independent of the local magnetic induction, B. He also neglected the effects of surface barriers. Hence, vortices enter the material for any applied field.

We work with cylindrical coordinates, so that positions are denoted by (r, φ, z). Writing $\mathbf{B} = B\,\hat{z}$, and $\mathbf{J}_c = -J_c\,\hat{\varphi}$ with $J_c > 0$, equation (2.13) reduces to:

$$\frac{\partial B}{\partial r} = \mu_0 J_c \quad \texttt{or} \quad 0 \tag{2.14}$$

in the superconducting material. This one-dimensional equation allows one to find the flux distribution along the tube thickness, and J_c is the slope of B along the radial coordinate. The magnetic induction in the hollow of the tube is uniform as the tube is infinitely long.

Because of the spatial variation of the magnetic induction, we see from (2.14) that a macroscopic current flows in the superconductor. This current creates a Lorentz force which tends to move vortices. But their migration is stopped if $\mathbf{F}_P = \mathbf{F}_L$. The

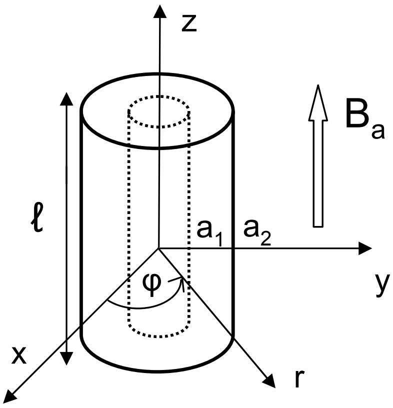

Figure 2.13: irreversible type-II superconducting tube in a uniform axial magnetic induction, B_{a}, with $\ell \to \infty$.

strong pinning condition of the Bean model imposes that the flowing currents due to the non-uniform field distribution have the maximum magnitude J_{c}. Then, one has $\mathbf{F}_{\mathrm{P}} = \mathbf{F}_{\mathrm{L}}$ at every point where $\mathbf{J} \neq 0$.

Suppose that the tube of figure 2.13 was first cooled in ZFC conditions, and then subjected to a magnetic induction B_{a}. Vortices enter from the outer surface, but are strongly pinned. As a result, B is not uniform along the tube thickness; it is higher near the outer surface, at $r = a_2$. From (2.14), this non-uniform flux distribution is associated with flowing currents of magnitude J_{c}. When increasing the applied induction, $\mathbf{F}_{\mathrm{L}}$ is temporarily larger than $\mathbf{F}_{\mathrm{P}}$, and pushes vortices towards the middle of the tube. As flux lines move towards a region of lower flux density, the current density decreases to J_{c} such that the equation $\mathbf{F}_{\mathrm{P}} = \mathbf{F}_{\mathrm{L}}$ is met again throughout the sample.

Figure 2.14 shows the magnetic induction in the plane $y = 0$ of the tube, for increasing and decreasing applied inductions, and the corresponding current distributions, following the Bean model. In the plane $y = 0$, the currents are parallel to the $\hat{y}$ axis.

If $B_{\mathrm{a}} = B_{\mathrm{a1}}$, the magnetic induction decreases towards the centre of the tube, and vanishes at $x = \pm x_1$ (figure 2.14(a)). From (2.14), the distribution of the magnetic induction along the tube thickness is linear, as J_{c} is constant. Currents only flow in the regions $x_1 < |x| < a_2$, because vortices have not reached the other parts of the tube.

At a higher applied induction, $B_{\mathrm{a}} = B_{\mathrm{a2}}$, vortices reach the inner surface of the tube. The applied field for which the tube is fully penetrated is called the field of full penetration, and is equal to

$$H_{\mathrm{P}} = J_{\mathrm{c}}\,(a_2 - a_1) = J_{\mathrm{c}}\,d. \qquad (2.15)$$

Then, currents flow into the whole thickness of the tube.

If B_{a} is further increased, $B(x)$ increases uniformly along the tube thickness, and the currents distribution is no longer changed. From figure 2.14, we see that the currents flow in such a direction that they tend to reduce the local magnetic induction in the material. Therefore, they are called shielding currents.

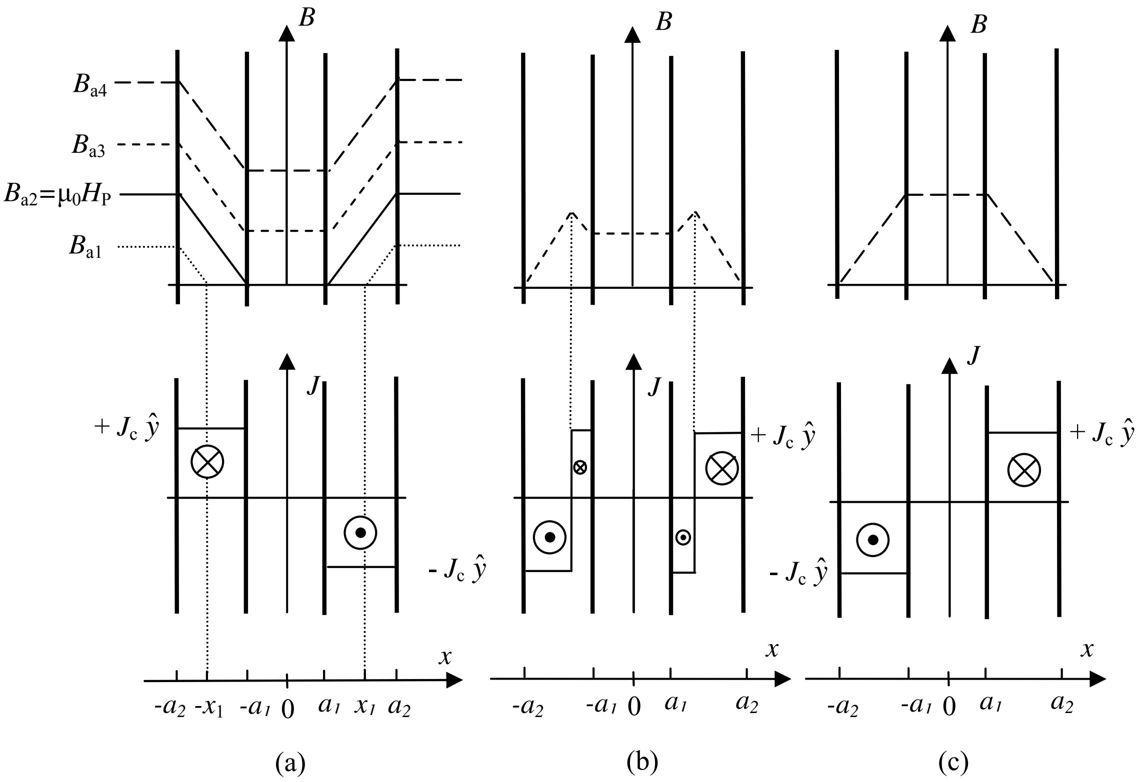

(a) (b) (c)

Figure 2.14: magnetic induction, and current distributions following the Bean model in an infinite tube subjected to a uniform axial magnetic induction B_a. Figure (a): increasing applied induction; figure (b): remnant state at $B_a = 0$ after having applied $B_{a3} < 2\,\mu_0\,H_P$; figure (c): remnant state at $B_a = 0$ after having applied $B_{a4} > 2\,\mu_0\,H_P$. The field H_P, defined by (2.15), is called the full penetration field.

Consider now the remnant state ($B_a = 0$). In figure 2.14 (b) (resp. (c)), the maximum induction applied before turning off the source field has reached $B_{a3} < 2\mu_0 H_P$ (resp. $B_{a4} > 2\mu_0 H_P$). Pinning of vortices, which opposes flux to penetrate the tube, also prevents vortices from leaving the tube when the applied induction is reduced. Hence, some vortices are pinned, and currents of magnitude J_c flow inside the tube thickness when B_a is reduced to zero. This pinning of vortices allows one to obtain a remnant magnetic induction (permanent magnet) with irreversible type-II superconductors. The maximum remnant induction one can obtain with an irreversible type-II superconducting tube increases with the thickness of the tube. Hence, high remnant magnetic inductions can be reached with irreversible type-II superconductors. The remnant induction is maximum if the applied field was higher than $2\mu_0 H_P$ in ZFC.

2.5.2 Shielding with irreversible type-II superconductors

Because of the pinning of vortices, one can expect that irreversible type-II superconductors have shielding properties and present a magnetic hysteresis. In this section, we study these properties using the Bean model.

Assuming that the tube of figure 2.13 has been cooled in ZFC conditions, figure 2.15(a) shows the evolution of the averaged magnetic induction in the superconducting material, $\langle B\rangle$, defined by (2.10), as a function of the applied magnetic induction B_a. Positive (resp. negative) values mean that the vectors $\langle \mathbf{B}\rangle$, and $\mathbf{B}_\mathrm{a}$ are directed along $\hat{z}$ (resp. $-\hat{z}$). We clearly observe a hysteretic behaviour: the averaged magnetic induction depends upon the history of the applied field. As H_c1 is assumed to be zero, $\langle B\rangle$ increases as soon as the applied field is turned on, but $\langle B\rangle$ is lower than B_a as the vortices are pinned next to the outer surface of the tube. At $B_\mathrm{a} = \mu_0 H_\mathrm{P}$, the curve of first magnetization meets the hysteretic cycle and for higher fields such that $B_\mathrm{a} \geq \mu_0 H_\mathrm{P}$, $\langle B\rangle$ increases as $B_\mathrm{a} - \mu_0 H_\mathrm{P}/2$. Reducing the applied field to zero, a remnant magnetic induction is present and is equal to $\mu_0 H_\mathrm{P}/2$.

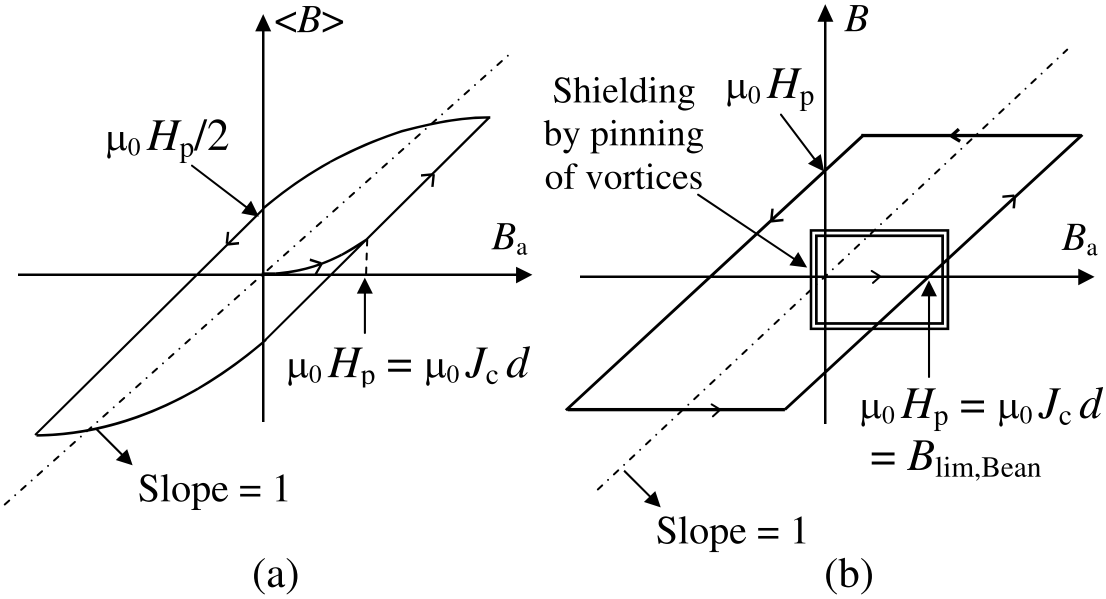

Figure 2.15: figure (a): magnetic induction averaged over the volume of the superconductor of the tube of figure 2.13, as a function of the applied magnetic induction. Figure (b): magnetic induction in the hollow of the tube as a function of the applied magnetic induction.

Figure 2.15(b) shows the evolution of the magnetic induction in the hollow of the tube, as a function of the applied induction. For shielding applications, we see that the region of interest for a sample cooled in ZFC conditions is located at $B_\mathrm{a} < \mu_0 H_\mathrm{P}$. For such applied inductions, the magnetic induction remains zero in the hollow of the tube. Hence, it is possible to shield magnetic fields that are much larger than H_c1 (which is assumed to be zero here) using irreversible type-II superconductors. When $B_\mathrm{a} > \mu_0 H_\mathrm{P}$, vortices reach the inner surface at $r = a_1$, raising the local induction in the hollow of the tube. Hence, from the Bean model, the maximum applied induction which can be efficiently shielded is given by

$$B_\mathrm{lim,Bean} = \mu_0 H_\mathrm{P}. \tag{2.16}$$

From (2.15), $B_{\mathrm{lim,Bean}}$ increases proportionally to the critical current density and the thickness of the tube.

If the tube is cooled in FC conditions, it no longer shields. Suppose that the tube has been cooled under $B_{\mathrm{a}} > \mu_0 H_{\mathrm{P}}$. After reducing the applied induction to zero, the remnant induction in the hollow is $\mu_0 H_{\mathrm{P}}$. Hence, as for type-I superconductors, it is important to cool a type-II superconductors in ZFC conditions for shielding applications.

2.6 Summary

Besides their remarkable electric properties, superconductors have specific magnetic characteristics. In this chapter, we have presented the magnetic properties of superconductors to show that these materials could be used to shield a low frequency magnetic field.

There are two types of superconductors. Type-I superconductors have reversible magnetic properties. When they are cooled below their critical temperature, T_{c}, and subjected to a magnetic field lower than the critical magnetic field, H_{c}, surface screening currents develop and cancel the magnetic induction inside the material (Meissner state). In contrast to traditional conductors, superconductors cancel the field itself and not only the field variation. Hence, they can give an interesting alternative to attenuate a low frequency or a DC magnetic field. When a type-I superconductor has a cavity, as it is the case for shielding applications, one has to cool the material with no applied field (zero-field cooled conditions, ZFC). If a magnetic field is applied during the cooling process, a magnetic flux is trapped in the cavity. The critical temperature of type-I superconductors is low: $T_{\mathrm{c}} < 10$ K. Hence, type-I magnetic shields have to be used at extremely low temperatures.

Type-II superconductors, which can have much higher T_{c} values than 10 K, have different magnetic properties than type-I materials. Below its critical temperature, a type-II superconductor subjected to a magnetic field lower than the first critical magnetic field, H_{c1}, is in the Meissner state as a type-I material. For higher magnetic fields, $H_{\mathrm{c1}} < H < H_{\mathrm{c2}}$, where H_{c2} is the second critical magnetic field, the magnetic induction enters the superconductor in the form of vortices. If vortices move freely in the superconductor (reversible type-II superconductors), the shielding properties of the material are poor for $H > H_{\mathrm{c1}}$. Vortices, repelling each other, form a regular lattice extending throughout the whole material. But generally, vortices cannot move freely. They are pinned by defects of the material. Then, the superconductor has strong irreversible shielding properties above H_{c1}. As $\mu_0 H_{\mathrm{c2}} > 10$ T typically, where H_{c2} is the maximum magnetic field for which the material is in the superconducting state, high magnetic inductions can be shielded with irreversible type-II superconductors.

In 1964, Bean introduced a theory, known as the Bean model, giving the field distribution in type-II superconductors with strong pinning. In this model, the sample is assumed to be infinitely long parallel to the applied field, so that the demagnetizing field is zero. Besides, any flowing current density in the superconductor is equal to the critical current density, J_{c}, which is the maximum current density that can flow in the material. Following this model, the maximum axial magnetic induction that can be efficiently shielded by an infinitely long irreversible type-II superconducting tube is $B_{\mathrm{lim,Bean}} = \mu_0 J_{\mathrm{c}} d$, where d is the thickness of the tube.

In our research project, we studied the shielding properties of high-temperature superconductors (HTS). As they are complex ceramic materials, we present some of their properties in the next chapter. The method used by the team of chemists to make a HTS shield is also explained.

Chapter 3

High-temperature superconductors (HTS)

In chapter 2, we have seen that superconductors have strong diamagnetic properties. Irreversible type-II superconductors, for which vortices cannot move freely, seem to be particularly interesting for shielding applications. Following the Bean model, these materials are expected to strongly attenuate a magnetic field if it is lower than a threshold field, which is proportional to the thickness and to the critical current density of the superconducting shield.

Magnetic shielding with low-temperature irreversible type-II superconductors has been reported [5, 49, 50]. A larger number of works concern high-temperature superconducting magnetic shields [25, 26, 27, 28, 29, 30, 31, 32, 33].

High-temperature superconductors (HTS), which belong to the type-II superconductors family, are complex materials. The aim of this chapter is to give a brief overview of their principal properties. This allows one to better understand the difficulties associated to the fabrication of a HTS magnetic shield. We also present the method used by the team of chemists to make our own HTS shields. To obtain more information concerning the chemical, and structural properties of the HTS, the interested reader is referred to [51, 52, 53, 54].

The chapter is organized as follows. In sections 3.1 and 3.2, we present some chemical and structural properties of HTS. Next, we illustrate the magnetic shielding of a HTS sample in section 3.3. Finally, we focus on the difficulties associated to the fabrication of a HTS shield and present the electrophoretic deposition technique, the method used by the team of chemists to make our shields.

3.1 Chemical aspects

HTS have a complex chemical composition and microstructure. Because of their multi-elementary composition, many other phases than the superconducting one can be present, some of them playing the role of pinning centres. One common feature of HTS is their two-dimensional character which results from their crystallographic structure. HTS structure consists of CuO_2 planes separated by layers of other elements or oxides. Because of this layered structure, HTS have strong anisotropic properties. Hence, the values of the superconducting parameters (such as the coherence length, ξ, or the London depth, λ) differ along the different crystallographic directions. The schematic structure of the HTS compound $YBa_2Cu_3O_7$, or Y-123, is shown in figure 3.1. We observe the CuO_2 layers, separated by an yttrium layer. Between each bilayer of CuO_2, there are chains of CuO and BaO. The a and b crystallographic directions lie in the CuO_2 planes, and the c axis is perpendicular to them. It is widely accepted that the CuO_2 planes are the principal stage for superconductivity, and that the other layers act as charge reservoirs [54].

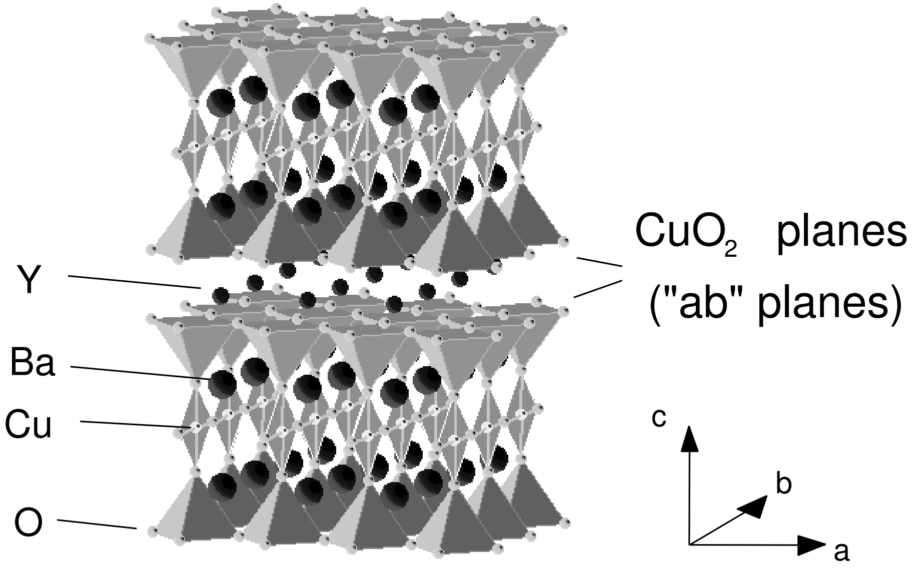

Figure 3.1: schematic structure of $YBa_2Cu_3O_{7-\delta}$ or Y-123.

HTS are characterized by a relatively high critical temperature T_c (which means that some HTS have $T_c > 77$ K), and by small coherence lengths [55]. At $T = 0$ K, one has $\xi_{a,b} = 3$ nm, and $\xi_c = 0.4$ nm for Y-123 [34]. Many kinds of defects can act as pinning centres in HTS (oxygen vacancies, dislocations, stacking faults, non-superconducting inclusions, ...). Nevertheless, the pinning force is finite and several effects can lead to vortex depinning. As an example, thermal energy can depin vortices out of their pinning centres. This process of depinning is particularly important in HTS, due to the large temperatures generally involved [55].

In addition to the two characteristic curves $H_{c1}(T)$ and $H_{c2}(T)$ of type-II superconductors, the HTS phase diagram contains a third characteristic line, $H_{irr}(T)$ (see figure 3.2). This curve is called the irreversibility line. For $H < H_{irr}(T)$, flux lines are strongly pinned and the sample is irreversible. For $H > H_{irr}(T)$, pinning becomes ineffective and vortices can move freely. Only the region below the irreversibility line is of practical interest for current transport and shielding applications. The HTS cannot carry a DC current without loss if vortices are not pinned, as the Lorentz force moves vortices and induces a finite electric field. For shielding applications, every field can reach the region to be protected if vortices are not pinned. The origin of the irreversibility line transition is not very well understood, but it seems that it is related to thermally activated processes and to the layered structure of HTS [56].

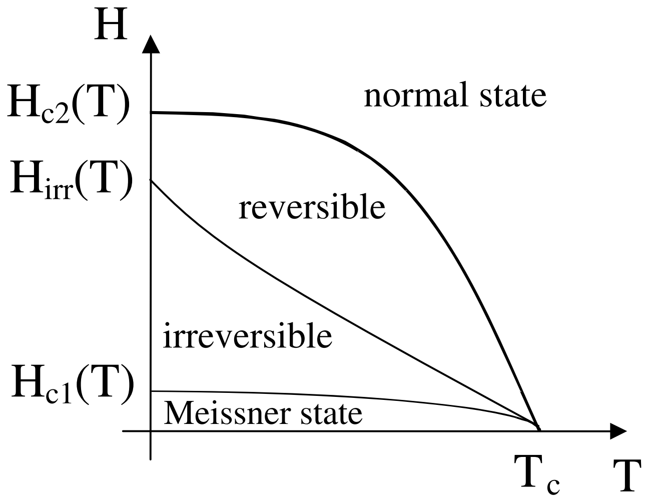

Figure 3.2: phase diagram in the $H - T$ plane ($J = 0$) for HTS. In addition to the curves $H_{c1}(T)$ and $H_{c2}(T)$, the diagram contains a third line, $H_{\mathrm{irr}}(T)$, below which vortices are pinned.

Three examples of HTS are $YBa_2Cu_3O_7$ (called Y-123 with $T_c \cong 92$ K), $Bi_2Sr_2Ca_2Cu_3O_{10}$ (called Bi-2223 with $T_c \cong 110$ K), and $Bi_2Sr_2Ca_1Cu_2O_{10}$ (called Bi-2212 with $T_c \cong 87$ K). On the one hand, Y-123 materials present better superconducting properties when the applications involve high magnetic fields. Indeed, at $T = 77$ K, the irreversibility induction, $\mu_0 H_{\mathrm{irr}}$, exceeds 5 T for Y-123, whereas $\mu_0 H_{\mathrm{irr}} = 0.3$ T for Bi-2223, and is less than 0.1 T for Bi-2212 [56]. On the other hand, Bi based materials present a priori better properties than Y-123 for current transport applications. This has to be related to the granularity of HTS which we discuss in the next section.

3.2 Granularity

The macroscopic superconducting properties of HTS strongly depend on their microstructure. Large (> 1 mm^3) HTS single crystals are difficult to grow. Hence, large HTS samples, which are ceramics, generally contain many grains that are weakly coupled together. Such samples are termed polycrystalline materials with weak links. These weak links strongly limit the maximum superconducting current that can flow macroscopically through the sample.

In chapter 2, we have seen that besides the critical temperature, a superconductor is characterized by its critical current density. In polycrystalline materials, one has to distinguish between the intragranular critical current density, J_{cg}, and the intergranular critical current density, J_{ci}. The first one is the critical current density which flows in each grain. The second one flows from grain to grain.

Generally, one has $J_{\mathrm{ci}} \ll J_{\mathrm{cg}}$, the exact value of J_{ci} depending on the exact microstructure. For large scale applications, the intergranular critical current density, J_{ci}, has to be optimized. For that purpose, the number of weak links has to be as small as possible by increasing the size of the grains, and the misorientation between the different c-axes of the different grains has to be minimized. Indeed, different studies have shown that the intergranular critical current density, J_{ci}, strongly increases when decreasing the misorientation of the different grains [57, 58, 59, 60].

Techniques have been developed to increase the size of the grains (for instance melt processing [61]). The most interesting method to obtain high quality bulk HTS is the top-seeded melt-texture growth [53, 62]. Then one can obtain a so-called single domain. A single crystal, typically $\mathrm{NdBa_2Cu_3O_7}$, $\mathrm{SmBa_2Cu_3O_7}$, or MgO, is placed on top of a precursor powder, for instance a Y-based powder. The powder is heated near the peritectic temperature of the YBaCuO system, T_{p}. For Y-123, $T_{\mathrm{p}} \cong 1015°$ C under air [63]. At T_{p}, the Y-123 phase decomposes to form a solid Y-211 phase, and a Ba, Cu rich liquid phase (incongruent fusion). During the cooling process, the Y-123 phase is re-formed, and the single crystal imposes the growth of the grain along a determined direction. Large single domains (a few centimetres) can be obtained with this technique. They are generally made of Y-123, as this compound presents a high irreversible field, H_{irr}. A Y-123 single domain consists of a pseudo-crystalline matrix composed of large parallel Y-123 crystal plates (platelets) having a common c-axis. A single domain generally contains many defects (Y-211 particles, cracks, ...), some of them playing the role of pinning centres for vortices [56, 64, 65].

Due to the ceramic nature of HTS, any shape or size cannot be realized with single domains. Hence, for large scale applications, such as current transport, polygranular forms of HTS have to be used. HTS cables consist either of superconducting filaments surrounded by normal conductors, or HTS films deposited on flexible metallic substrates (coated conductors or tapes). For such transport applications, Bi based materials were first preferred to Y based compounds. The connectivity between the different grains of the first kind of materials is a priori better, as a grain grows like a parallelepiped of small thickness (platelike grains) [52]. This particular shape tends to align the different c-axes of the grains naturally (natural texturation). Now, many teams work on the fabrication of long Y-123 tapes, as this compound has a much higher irreversibility field.

The intergranular critical current density is expected to strongly depend on the microstructure of the considered sample, which in turn strongly depends on the synthesis method and the sample type. As we are interested by the macroscopic properties of HTS, in what follows, J_{c} refers to the intergranular critical current density, unless otherwise stated. For epitaxially grown Y-123 thin films (thickness around 100 nm), values of $J_{\mathrm{c}} > 10^6$ A/cm^2 are reported at $T = 77$ K in self field [66, 67]. Values up to $J_{\mathrm{c}} = 10^5$ A/cm^2 have been reported for large (few centimetres) single domains at $T = 77$ K in self field [68]. Coated conductors, designed to transport large current densities, consist of a network of predominantly low angle grain boundaries. Hence, very high current densities can flow in such tapes. As an example, $J_{\mathrm{c}} \cong 10^6$ A/cm^2 at $T = 77$ K and in self field, is reported for Y-123 coated conductors, of thickness equal to 1 μm [69]. For depositions of larger thickness (~ 100 μm) with many grains, J_{c} is rather of the order of 10^3 A/cm^2 [70].

In section 3.4, we detail the appropriate fabrication method to obtain a large HTS magnetic shield. We also give the expected value of J_{c} for such samples. Beforehand, we present an illustrative result showing the magnetic shielding properties of a HTS sample.

3.3 Illustration of magnetic shielding in a bulk HTS

In chapter 2, we have seen that irreversible type-II superconductors have magnetic shielding properties above H_{c1}. To illustrate the irreversibility of HTS, we present some qualitative results obtained with the magneto-optical imaging (MOI) technique, which gives the magnetic induction distribution above the surface of a superconducting sample.

MOI is based on the Faraday effect. In the presence of a magnetic field, a Faraday active material, called magneto-optical layer (MOL), rotates the polarization plane of a linearly polarized transmitted beam of light. The rotation angle increases with the magnitude of the field component parallel to the beam direction. Thus, by placing the MOL on top of a superconductor, it is possible to visualize the surface magnetic field distribution. A detailed description of the experimental method can be found in [71, 72].

To illustrate the shielding properties of HTS, we use a $DyBa_2Cu_3O_7$ single domain made by the top-seeded melt-textured technique [53]. A previous characterization gave $T_c \cong 89$ K. The sample size is $1.8 \times 1.8 \times 0.6$ mm^3, the two first dimensions lying in the *ab* plane, whereas the last one is directed along the *c*-axis. Figure 3.3 shows a photograph of the sample. White regions in the lower right corner and in the upper left corner are traces of silver paint. The sample, with its *c*-axis perpendicular to the image plane, was placed in an optical cryostat. The MOL was put on top of the visible sample surface of figure 3.3, and the whole system was cooled to 82 K in ZFC conditions.

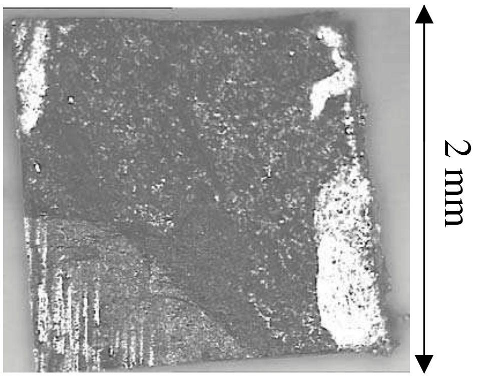

Figure 3.3: photograph of the $DyBa_2Cu_3O_7$ single domain used for the MOI experiment. The *c*-axis of the sample is perpendicular to the figure plane.

Then, an increasing magnetic induction was applied by a copper coil along the *c*-axis of the sample, and magneto-optical images were recorded. Figures 3.4 (a)-(g) show the pictures for different increasing applied magnetic inductions, and figure 3.4

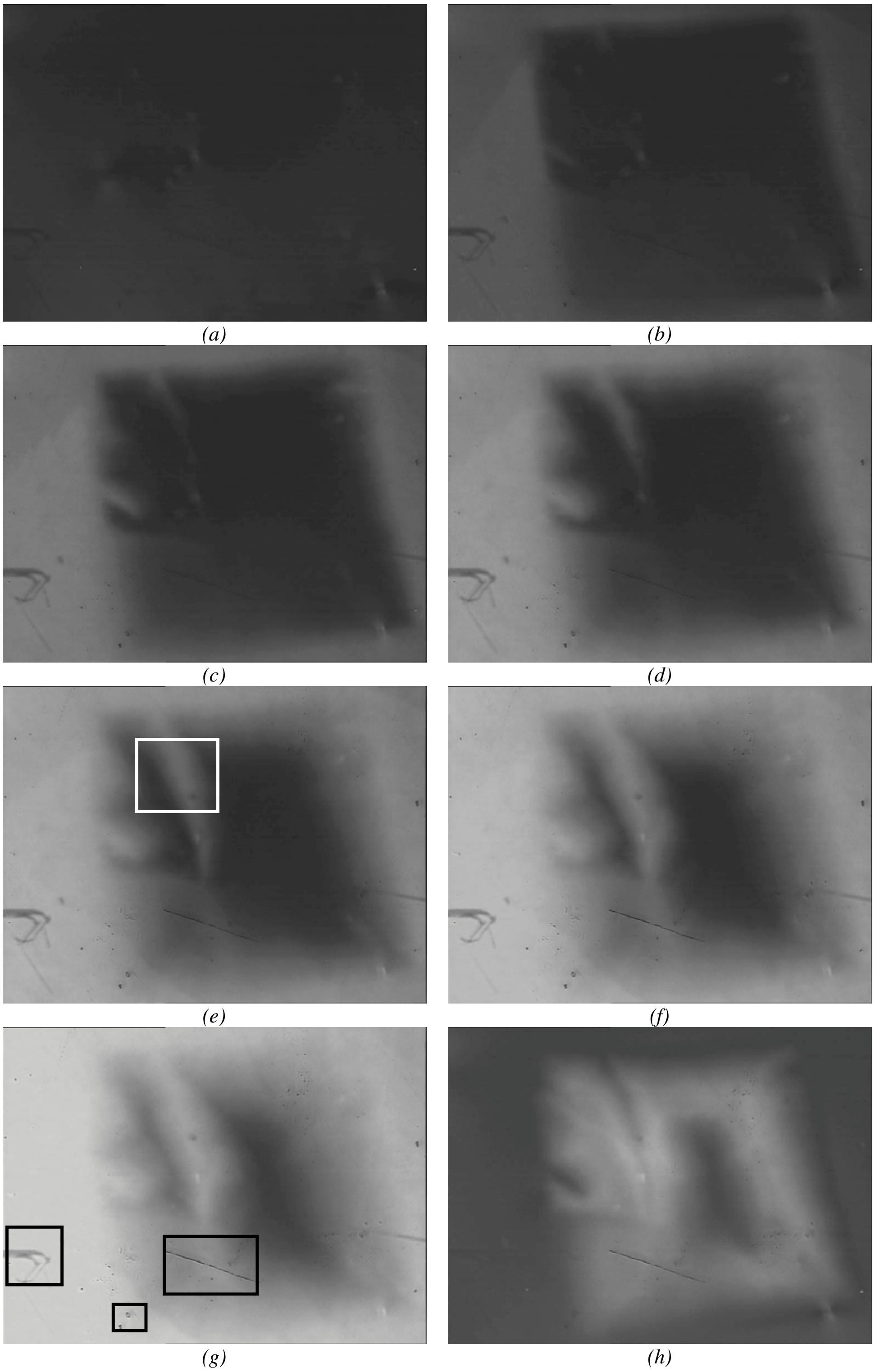
(a) (b) (c) (d) (e) (f) (g) (h)

Figure 3.4: magneto-optical pictures at 82 K for the $DyBa_2Cu_3O_7$ sample cooled in ZFC conditions. Figures (a)-(g): B_a = 0, 18, 36, 54, 72, 89, 107 mT; figure (h): remnant state after having applied $B_\mathrm{a} = 107$ mT.

(h) shows the remnant state after having applied 107 mT. Bright areas correspond to the strongest local magnetic inductions.

We clearly observe that magnetic flux does not easily penetrate the single domain. Vortices, which are strongly pinned, do not entirely penetrate the sample, and their concentration is larger near the sample edges. The magnetic induction penetrates more easily some regions, such as the zone delimited by the square of figure 3.4 (e). This region represents a crack along which vortices can enter the material, reducing its shielding properties. Such defects, which cannot always be observed in the optical pictures such as that of figure 3.3, have to be avoided for shielding applications. In figure 3.4 (g), some regions of the sample are black, meaning that the sample is not fully penetrated. Hence, $\mu_0 H_\mathrm{P} > 107$ mT. The lower left corner of the sample is penetrated faster than the other regions. This region could also be seen different from the others in figure 3.3. The rectangles in figure 3.4 (g) delimit defects of the magneto-optical layer. Reducing the applied induction to zero, a remnant magnetic induction is present on top of the sample surface, as some vortices are pinned (figure 3.4 (h)).

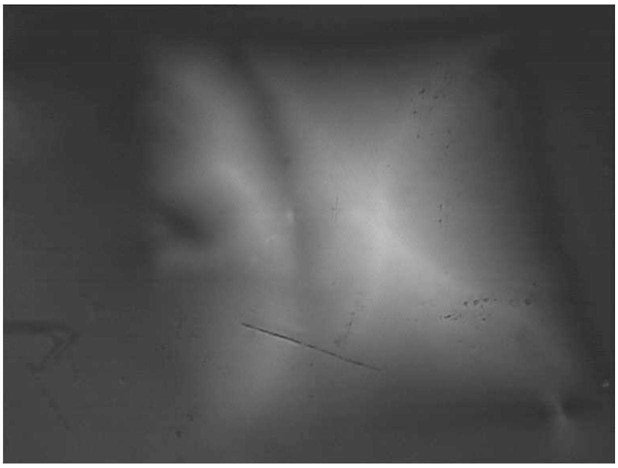

Figure 3.5: magneto-optical picture at 82 K for the $\mathrm{DyBa_2Cu_3O_7}$ sample in the remnant state ($B_\mathrm{a} = 0$ mT), cooled in FC conditions under $B_\mathrm{a} = 112$ mT.

A last picture (figure 3.5) shows the remnant state ($B_\mathrm{a} = 0$) above the same sample, but cooled in FC conditions down to 82 K under $B_\mathrm{a} = 112$ mT. If we do not consider the left part of the sample containing the crack, we see a magnetic profile close to that one could expect from the Bean model (pyramidal shape). So, even if the thickness of the sample is not large compared to the other dimensions, which means that the demagnetizing factor is not negligible, the Bean model seems to give a good qualitative description of the vortex distribution.

3.4 Techniques for fabricating a HTS magnetic shield

Early after 1986, people thought about the possibility to make efficient low frequency magnetic shields with HTS due to their property of strong pinning of vortices [31, 32, 73, 74, 75]. Y-123 polygranular tubes, or disks, were used in shielding measurements, clearly showing a high field attenuation. Y-123 seems to be a good candidate for shielding applications, as it presents a high irreversibility field. Typically, samples were made by cold pressing a precursor powder into the final shape, which was then heated near the peritectic temperature of the HTS [31, 32, 75]. This heat treatment which is called sintering process is particularly important. By heating the sample near the peritectic temperature of the YBaCuO system, a liquid phase is formed. This ensures a densification of the material, as well as a good connectivity between the different grains.

HTS are brittle ceramics. Hence, making large bulk HTS of complex shape is intricate. One could join different bulk samples together to obtain a larger one with silver paint [76], or with a superconducting paste [77], but the resulting shield would be heavy, and susceptible to cracking during handling and temperature cycling. Any defect of the HTS material can strongly reduce the shielding capabilities as it presents an entry for the magnetic flux (see section 3.3).

A better solution would be to grow a HTS film on a metallic substrate having the desired shape for the application [78, 79]. This should allow one to make large magnetic shields of complex shapes. To be efficient, the thickness of the coating has to be larger than λ. For Y-123, $\lambda_c \cong 200$ nm at 0 K [34]. Hence, very small thicknesses (< 1 μm) are not suitable for shielding applications, and thick films (thickness larger than 10 μm) are preferable.

Deposition techniques of thick films differ from that of thin films [80] (such as sputtering, laser ablation, chemical vapour deposition). Thin films are usually produced by methods which induce an epitaxial growth of the coating onto a single crystal substrate, which is not the case for thick films production. Thick films consist of a large number of grains, randomly oriented with respect to each other if no texturing is present. In the past, different thick films deposition techniques were used to make HTS shields.

Pavese et al. [33, 81] used the continuous detonation spray (CDS) technique to depose Y-123 coatings on silver and stainless steel substrates. This technique is based on a supersonic jet of powder propelled by a continuous detonation combustion of oxygen and propane. Pavese reports fast production of coatings (0.1 $\mathrm{m}^2\ \mathrm{min}^{-1}$), and coatings of high density due to supersonic impacts [33]. Tubes of diameter equal to 2 cm, and 20 cm long have been made. The thickness of the coating lies between 40 μm and 80 μm. A larger thickness induces too many cracks. At $T = 77$ K, such samples attenuate a magnetic induction lower than 0.1 mT. No value is given for the obtained shielding factor.

Another deposition method of thick films is the plasma spray technique. A precursor powder is introduced into a plasma flame generated by an electric arc, wherein the powder particles become molten, atomized, and sprayed onto the substrate surfaces. On impinging on the substrate, the powder particles flatten, splatter, quench, and overlap one another to form a dense and coherent coating. Karthikeyan et al. [82] have produced Y-123 coatings on stainless steel plates (4.5 cm × 4.5 cm × 1 mm) using the plasma spray technique. The thickness of the coatings lies between 150 μm and 200 μm. At $T = 77$ K, these coatings attenuate a magnetic induction lower than 0.4 mT. Here again, no value is given for the obtained shielding factor.

If one wants to make magnetic measurements with very high sensitivity (detection of magnetic inductions lower than 10^{-12} T), magnetic shielding is necessary to reduce the ambient noise. Due to their high field attenuation, HTS shields have been used in neuromagnetic SQUID measurements, that aim at measuring the brain activity. Ohta et al. [83, 84] have built a large HTS shield enclosing the SQUID measurement device: using the plasma spray technique, a thick Bi-2223 film has been deposited on a nickel cylinder, which has a diameter of 65 cm and a length of 160 cm ! They report a shielding factor of up to 80 dB (10^4) even if the frequency of the field to shield is around 0.05 Hz. The maximum magnetic induction that can be efficiently shielded with their HTS screens is not specified.

Hence, by growing HTS thick films on a metallic substrate, one should obtain large size magnetic shields. The chemists team of our project used the electrophoretic deposition (EPD) technique to grow thick Y-123 films on metallic substrates. We explain the main features of EPD in the next section.

3.4.1 The electrophoretic deposition (EPD) technique

The electrophoretic deposition (EPD) technique involves the preparation of a stable suspension of a material powder in an organic dispersant, or in water, and the application of an electric field between two electrodes dipped in it. Depending on the net charge of the powder particles, a deposit forms on the cathode or on the anode as particles are driven by the applied electric field. The shape and the size of the resulting coating only depend upon that of the electrode. Hence, complex and large coatings can be obtained with this method. In this section, we first give some examples where the EPD was used. Second, we briefly discuss the main experimental parameters, as well as the difficulties of using EPD. Reviews on the EPD technique can be found in [85, 86, 87].

History

Early, the EPD technique was used in industry to make enamels for sanitation [88] and to deposit anticorrosive paint in the automobile industry [89]. Different materials can be used (metals, polymers, ceramics) to produce objects of various shapes (films and bulks) [85, 86, 90]. Nevertheless, the EPD has been mainly used with ceramics and some teams grew HTS films with this technique.

Two years after the discovery of the superconducting phase Y-123, Chu et al. [91] used the EPD technique to deposit Y-123 coatings on Cu, Ag, and Al_2O_3 substrates, as well as on single crystals of MgO and $YZrO_2$. The thickness of the coating lied between 200 μm and 500 μm. Maiti et al. [92] produced coatings on silver tapes with $J_c \cong 85$ A/cm^2 at 77 K in self field. In 1991, Woolf et al. [93] made a continuous process to deposit Y-123 on Ni based wires. One kilometre long individual filaments were produced. A dozen of such wires were also introduced in a copper sheath to obtain a multifilament wire (of length up to 70 metres). At 77 K, they obtained J_c values around 10^3 A/cm^2 in self field.

Bi based materials have also been deposited with the EPD technique [94, 95, 96] to produce superconducting tapes. Nevertheless, the obtained critical current densities are small, and other techniques are generally preferred (especially the powder in tube technique). The production of HTS coatings with low critical current densities is the main disadvantage of the EPD technique.

Experimental details and difficulties

The exact mechanisms involved in the EPD are not fully understood. Generally, the different process parameters (applied electric field, deposition time, ...) are determined in an empirical manner.

First, a stable suspension without cluster has to be prepared. For Y-123 coatings, the electrophoretic bath generally consists of 100 ml of acetone, containing 1 g of Y-123 particles (hence, concentration of 1 % wt), and 20 ml of iodine as an addictive to increase the superficial charge of the Y-123 particles [70, 97, 98]. The size of particles generally lies around 2 μm. Too large particles induce sedimentation because of gravity. After 5-8 min of sonication, a homogeneous suspension is obtained. Then, if one applies an electric field between the two electrodes dipped in the solution, a coating grows on the cathode, indicating that Y-123 particles have a positive charge in the solvent. It seems that this positive charge comes from the adsorption of positive ions onto the surface of the Y-123 particles [70], but this explanation is under debate. Figure 3.6 shows a schematic diagram of an EPD cell.

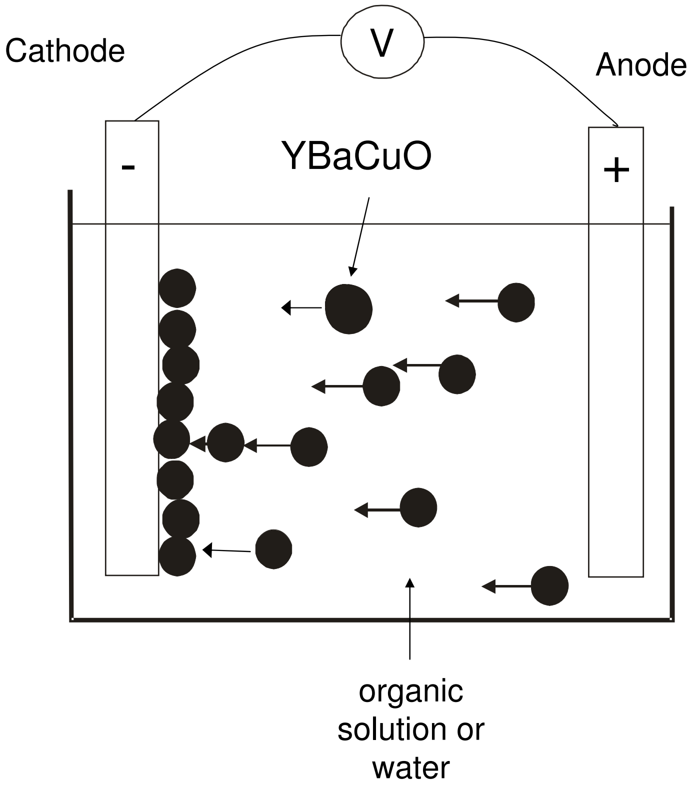

Figure 3.6: principle of the EPD technique. When an electric field is applied between the two electrodes, the positive Y-123 particles move towards the cathode.

After having obtained a stable suspension, a constant electric field is generally applied between the two electrodes. As the Y-123 particles move in the solution, a current flows. Under a constant applied electric field, the current decays as a function of deposition time [70, 99]. This comes from two effects. First the deposition process consumes the charged particles in the solution, decreasing its conductivity. Second, as the deposited Y-123 particles are not electrically connected, an increasing resistance develops in series of the solution resistance, so that the effective electric field applied to the solution decreases with time. This decrease of current yields coatings of low density. To decrease the resistance of the coating, and thus to increase the current in the bath, a multistep deposition is generally applied [70, 98, 100]. Each single layer is about 20 μm thick, and after each deposition step, a heat treatment is performed to obtain a dense coating, with electrical connections between the grains. Then, the resistance of the coating decreases, increasing the current between the electrodes during the next deposition step, and giving denser films. The details of the intermediate heat treatment can be found in [70, 98].

The applied electric field, the deposition time, the preparation and concentration of the suspension, the current intensity, and the conditions of stirring are the main parameters of the EPD process that affect the quality and the thickness of the film. Generally, our EPD coatings are made using the multistep deposition, with an applied electric field around 200 Vcm^{-1} during 60 s for each layer. The thickness of each layer is around 20 μm, and the final coating has typically a thickness between 50 μm and 80 μm (3 or 4 layers). Coatings thicker than 100 μm have a low density, and many cracks.

3.4.2 Heat treatment after the deposition

After the deposition step, the sample undergoes a final heat treatment which has two main purposes. The first goal is to obtain an oxygen-rich Y-123 phase, by annealing under 500° C during 30 h [51, 53, 54]. The second purpose of the heat treatment is to obtain a dense coating with mechanically connected grains. This should allow one to have a macroscopic superconducting path in the HTS layer. To obtain such a dense coating with connected grains, it is necessary to heat the sample near the peritectic temperature, T_{P}, of the YBaCuO system, where a liquid phase appears. This step of the heat treatment near T_{P} is called sintering.

There are two difficulties associated with the sintering of coatings on metallic substrates. First, if the melting point of the substrate, T_{f}, is close to T_{P}, the substrate loses its mechanical stability if temperatures around T_{P} are involved during the heat treatment. Second, some atoms of the metallic substrate diffuse into the Y-123 layer at high temperature. Depending on the type of substrate, the superconducting properties of the coating can be altered because of this diffusion.

In this project, we studied the superconducting properties of coatings deposited on silver and nickel with no buffer layer between the metallic substrate and the HTS layer. Silver is known to be non destructive for the superconducting Y-123 phase [101]. As we will see in chapter 5, this is not the case for nickel. Nickel was initially thought to be interesting to be used for the substrate, as it is ferromagnetic and can thus contribute to the atenuation of the magnetic field.

The maximum temperature which can be used during the heat treatment depends upon the used substrate. In air, the peritectic temperature of YBaCuO is $\sim 1015°$ C.

The melting point of silver, T_{f}, is 962° C, but it loses its mechanical rigidity at around 930° C [63, 102]. Therefore, one cannot heat an EPD coating on silver near T_{P} =1015° C.

The fusion point of nickel is higher than that of silver: $T_{\mathrm{f}} = 1455°$ C for nickel. Besides, nickel loses its mechanical stability at a higher temperature than the peritectic temperature of the YBaCuO system. Hence, one could expect to have dense Y-123 coatings with connected grains using a nickel substrate. However, there are other difficulties for coatings on nickel. During a heat treatment at high temperature, some atoms of the substrate diffuse into the HTS film if no buffer layer is used. This diffusion increases with the temperature. In contrast to silver, diffused nickel can strongly affect the superconducting properties of the Y-123 phase [103, 104]. In particular, some Ni^{2+} ions can enter the crystallographic structure of the Y-123 phase, replacing some Cu^{2+} ions of primary importance for superconductivity. As a result, the critical temperature decreases, by an amount that increases with the nickel proportion in the Y-123 phase. This decrease of T_{c} occurs until the Ni doped Y-123 is no longer superconducting [103, 104]. Because of this diffusion, one cannot heat a Y-123 coating on nickel near T_{P} =1015° C.

In chapter 5, we detail and explain the thermal treatments used for obtaining the best EPD coatings on silver and nickel.

3.4.3 HTS samples made with the EPD technique

Y-123 coatings produced by the EPD technique generally present moderate values of the critical current density, as they have many randomly oriented grains. For planar films with a thickness larger than 20 μm, values between $J_{\mathrm{c}} = 500$ A/cm^2 and $J_{\mathrm{c}} = 1000$ A/cm^2 are reported [70, 98, 100, 105] at $T = 77$ K in self field. Texturation of the coating under a magnetic field has improved the critical current density from 220 to 460 A/cm^2 [106], hence remaining of the order of 1000 A/cm^2. Such performances are only attained for coatings with a thickness smaller than 100 μm.

Using the Bean model, we deduce that the maximum magnetic inductions which can be efficiently shielded with the EPD coatings are low: $B_{\mathrm{lim,Bean}} \leq 1$ mT from (2.16). If higher magnetic inductions have to be shielded, a concentric shield made of a traditional ferromagnetic material has to be used as a first screen, to reduce the field applied to the superconducting coating. The innermost screen must be the superconducting layer, as it presents the highest field attenuations (see chapters 5 and 6).

3.5 Summary

High-temperature superconductors (HTS), which are type-II superconductors, have specific properties. Besides the two critical magnetic fields, H_{c1} and H_{c2}, they are characterized by a third important field: the irreversibility field, H_{irr}. Below H_{irr}, HTS present a strong pinning of the vortices, and for higher magnetic fields, the vortices are not pinned.

HTS are brittle ceramics with a complex chemical composition and microstructure. Large HTS samples generally contain many grains. The electric properties of these materials strongly depend upon their microstructure.

Our project is to use the HTS compound Y-123 ($T_c \cong 92$ K) to shield low frequency magnetic fields. Y-123 seems to be a good HTS candidate for shielding applications as it has a high irreversibility field: $\mu_0 H_{\mathrm{irr}} \cong 5$ T at 77 K. To make large HTS shields of complex shape, the deposition of a thick polycrystalline film on a metallic substrate seems to be the best solution. To make our Y-123 shields, the chemists team of our project chose the electrophoretic deposition (EPD) technique. This method is based on the preparation of a precursor suspension of the HTS ceramic in a solvent, and the application of an electric field between two electrodes dipped in the solution. Because of the application of an electric field, the Y-123 particles move towards and settle on the cathode. To obtain a good connectivity between the different grains of the coating, a heat treatment is finally applied to the EPD sample.

Before presenting our results, we discuss in the next chapter the limitations of the Bean model to study the field penetration into HTS. We also explain the constitutive laws and the numerical method of Brandt, which we used in our theoretical study.

Chapter 4

Methods to study the field penetration in HTS

In section 2.5.1, we have introduced the Bean model. Knowing the applied magnetic field and the critical current density, J_{c}, this model allows one to determine the field distribution in infinitely long HTS with strong pinning. Following Bean's ideas, Campbell and Evetts studied the field penetration into irreversible type-II superconductors of arbitrary cross-section [107].

The Bean model is based on simplifying assumptions. For realistic shielding configurations, three additional effects have to be taken into account. First, for polygranular HTS, the critical current density is known to be very sensitive to small magnetic inductions. Kim introduced a model to take into account the decrease of J_{c} with the local magnetic induction, B. Second, at $T \neq 0$ K, the vortex dynamics is affected by the finite temperature. This effect, which is not included in the Bean model, can be modelled by an appropriate relation between the current density, J, and the electric field, E. Third, the Bean model is only strictly correct for geometries without demagnetizing effects. For some geometries with a non zero demagnetizing factor, it is possible to calculate the field distribution with appropriate numerical methods.

In this chapter, we first present the method of Campbell and Evetts which is used in chapter 6 to study the field penetration into infinitely long cylinders with hollow cross-sections of various shapes. After, we introduce the Kim law which allows one to take into account the field dependence of the critical current density. In section 4.3, we detail the limitation of the Bean model related to the assumed relationship between E and J. We also discuss the flux creep regime. In section 4.4, we point out the geometric limitations of the Bean model. Finally, we present the numerical method of Brandt which allows one to determine the field distribution in some geometries with demagnetizing effects. This method is used in chapters 6 and 7 for our theoretical study.

4.1 The method of Campbell and Evetts

Following the Bean model, Campbell and Evetts proposed a graphical method which allows one to find quickly the position of the flux front and the direction of the cur-

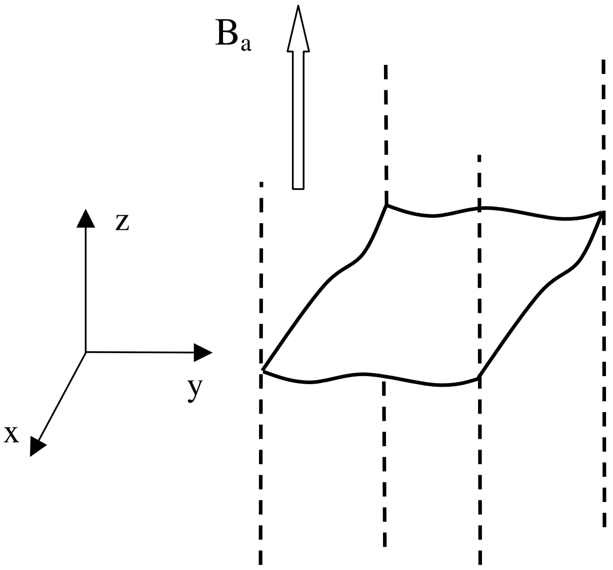

Figure 4.1: infinitely long sample in the $\hat{z}$ direction, with a uniform magnetic induction applied parallel to the z-axis, $\mathbf{B}_{\mathrm{a}} = B_{\mathrm{a}}\,\hat{z}$.

rent stream lines in infinitely long irreversible type-II superconductors of arbitrary cross-section [107]. To explain this approach, we consider the geometry of figure 4.1. This corresponds to an infinitely long sample in the $\hat{z}$ direction, subjected to a uniform magnetic induction $\mathbf{B}_{\mathrm{a}} = B_{\mathrm{a}}\,\hat{z}$. The cross-section in the $x - y$ plane can have any shape.

For such a geometry, there is no variation of the current density, $\mathbf{J}$, and of the magnetic induction, $\mathbf{B}$, with respect to z. Moreover,

$$\mathbf{B} = B\,\hat{z}. \tag{4.1}$$

From the Maxwell equation

$$\nabla \times \mathbf{B} = \mu_0 \mathbf{J}, \tag{4.2}$$

we deduce

$$\mu_0 J_{\mathrm{x}} = \frac{\partial B}{\partial y}, \qquad \mu_0 J_{\mathrm{y}} = -\frac{\partial B}{\partial x}, \qquad J_{\mathrm{z}} = 0. \tag{4.3}$$

Hence, the current density flows in a plane perpendicular to B. The infinite tube that we used to illustrate the Bean model in section 2.5.1 is a particular case of the geometry that we consider here. In section 2.5.1, it was a one dimension problem. Here, it is a two dimensions problem.

Taking the norm of (4.2) and imposing $J = |\mathbf{J}| = J_{\mathrm{c}}$ in the penetrated regions, one obtains:

$$\sqrt{\left(\frac{\partial B}{\partial x}\right)^2 + \left(\frac{\partial B}{\partial y}\right)^2} = |\nabla B| = \mu_0 J_{\mathrm{c}}, \tag{4.4}$$

which is constant if we assume that the critical current density does not depend upon the magnetic induction.

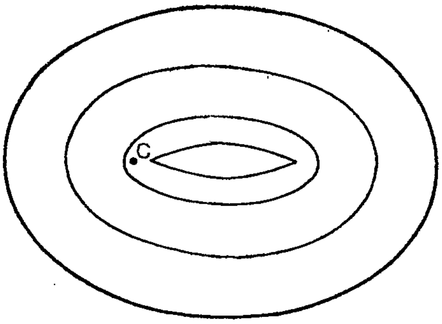

Figure 4.2: flux front (or contours of constant B) at increasing applied fields for an infinitely long cylinder of elliptical cross-section (from [107]). The outer ellipse represents the sample cross-section. The applied magnetic induction is directed perpendicular to the figure plane. The point c is the centre of curvature closest to the cross-section perimeter.

From the definition of the gradient, equation (4.4) implies that the perpendicular distance between two given contours of constant B is the same all along these contours [107]. As the applied field increases, the flux front, defined as the boundary between regions with and without currents, progresses in the sample from its outer surface and each part of the front is at the same perpendicular distance from this surface. Hence, the flux front has the same shape as the cross-section of the infinite superconductor, until it reaches the centre of curvature of any part of the surface. This is illustrated in figure 4.2 which shows the flux front at increasing applied fields for an elliptical cross-section. The different positions of the flux front also correspond to the contours of constant B. These contours are also the trajectories followed by the current. In fact, from (4.2) and the assumed geometry, we have:

$$\mathbf{B} \times (\nabla \times \mathbf{B}) = \nabla \left(\frac{B^2}{2} \right) = \mu_0 \, \mathbf{B} \times \mathbf{J}. \tag{4.5}$$

As $\mathbf{B} = B\,\hat{z}$, and $\nabla\left(B^2\right)$ is perpendicular to the contours of constant B, $\mathbf{J}$ follows the contour lines of figure 4.2. For cross-sections whose boundary presents sharp edges (square, rectangle, triangle, ...), this construction leads to discontinuity lines along which $\mathbf{J}$ abruptly changes its direction.

4.2 Field dependence of the critical current density: the Kim law

In the Bean model and in the method of Campbell and Evetts, we assumed that the critical current density, J_c, does not depend on the magnetic induction, B. In reality however, J_c is expected to decrease as the local magnetic induction, B, increases. Taking an independent critical current density overestimates the shielding properties of real HTS, as J_c is the slope of the decrease of B within the sample.

In chapter 3, we made the distinction between two critical current densities. The intragranular critical current density, J_cg, flows within each grain, while the intergranular critical current density, J_{ci}, flows from grain to grain. Typically, J_{ci} is several orders of magnitude lower than J_{cg}, as the intergranular current must cross each grain. In this manuscript, J_{c} refers to the macroscopic critical current density. Hence, $J_{\mathrm{c}} = J_{\mathrm{ci}}$ for a polygranular material. Experimentally, the intergranular critical current density was found to be very sensitive to low magnetic inductions [108, 109]. Hence, taking a constant J_{c} is not very realistic.

Different models exist to take the field dependence of J_{c} into account [20]. Here, we follow the Kim model [110], which agrees very well with our experimental results, as will be demonstrated in chapters 5 and 6.

Following Kim's law, the critical current density, J_{c}, decreases with the local magnetic induction B as

$$J_{\mathrm{c}}(B) = \frac{J_{\mathrm{c}\,0}}{1 + B/B_1}, \tag{4.6}$$

where $J_{\mathrm{c}\,0}$ is the critical current density with no magnetic induction. The two parameters, $J_{\mathrm{c}\,0}$ and B_1, can be obtained by fitting experimental data using (4.6), or expressions derived from it (see chapters 5 and 6). From (4.6), we observe that $J_{\mathrm{c}}\,B$ is field independent if $B \gg B_1$, where $J_{\mathrm{c}}\,B$ represents the strength of the Lorentz force.

To study the shielding properties of HTS samples, one could use the Bean model with (4.6) to take into account the field dependence of J_{c}. Then, one should solve the equation $\nabla \times \mathbf{B} = \mu_0 \mathbf{J}_{\mathrm{c}}(B)$.

However, there are two limitations of the Bean model which result from two assumptions of the Bean model: the assumed relationship between the electric field and the current density, and the geometry for which the model is strictly correct. In the next section, we explain the first limitation and detail the flux creep regime. After, we focus on the geometric limitations of the Bean model.

4.3 Limitation of the Bean model related to the assumed relationship between E and J

The Bean model is based on the assumption that an equilibrium exists between the Lorentz force, $\mathbf{F}_{\mathrm{L}} = \mathbf{J} \times \mathbf{B}$, which tends to move vortices, and the pinning force, $\mathbf{F}_{\mathrm{P}}$, which tends to maintain vortices immobile:

$$\mathbf{F}_{\mathrm{P}} = \mathbf{F}_{\mathrm{L}}. \tag{4.7}$$

In the Bean model, only the Lorentz force can depin vortices.

Equation (4.7) implies that any current density flowing in the superconductor takes the value: $J = J_{\mathrm{c}}$. It is also assumed that no current densities higher than J_{c} can flow in the superconductor. Hence, in the Bean model, the relationship between the electric field, E, and the current density, J, is that shown in figure 4.3.

In real HTS however, the current density takes a whole range of values. Then, if one assumes that only the Lorentz force can depin vortices, J_{c} is defined as the limit between lossless (pinned vortices) and lossy (moving vortices) regimes. With this definition, J_{c} is the current density for which one has the equality (4.7).

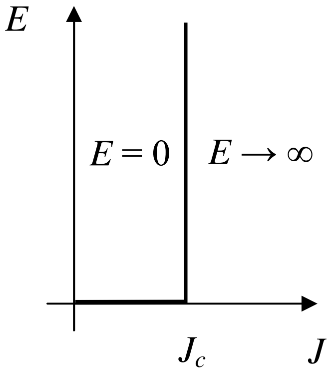

Figure 4.3: $E-J$ curve for an irreversible type-II superconductor in the Bean model.

Effects other than the Lorentz force, $\mathbf{F}_{\mathrm{L}}$, can release vortices from their pinning sites. In particular, the relaxation of vortices occurs when they have enough thermal energy [111]. Once depinned, vortices move in the direction of the Lorentz force $\mathbf{F}_{\mathrm{L}}$. Depending upon the importance between thermal effects and the effects related to the Lorentz force, there are different regimes, hence different relations between the electric field, and the current density. It follows that the $E-J$ curve of real HTS differs from that shown in figure 4.3.

At $T = 0$ K, only the Lorentz force can depin vortices. Hence, vortices are pinned ($E = 0$) if $J < J_{\mathrm{c}}$. When $J > J_{\mathrm{c}}$, vortices move, and the superconductor enters the flux-flow regime. A moving vortex experiences a viscous drag. In a first approximation, one can write [112]:

$$\mathbf{E} = \rho_{\mathrm{FF}}\mathbf{J}, \tag{4.8}$$

where the flux-flow resistivity is given by [112, 113, 114]:

$$\rho_{\mathrm{FF}}(B,T) \cong \rho_{\mathrm{n}} B/B_{\mathrm{c2}}(T), \tag{4.9}$$

where $B_{\mathrm{c2}} = \mu_0 H_{\mathrm{c2}}$, and ρ_{n} is the normal state resistivity.

If $T \neq 0$ K, thermal energy can also depin vortices. Thermal activation is particularly important for HTS [111, 112, 114, 115], as pinning energies are small, and the involved temperatures are generally high (typically 77 K). Working close to the critical temperature, T_{c}, a small current density is sufficient to depin vortices. This regime, where the resistivity $\rho = \mathrm{d}E/\mathrm{d}J$ is linear, is called thermally assisted flux flow (TAFF) [112, 116].

At lower temperatures, a higher current density is necessary to set the vortices into motion. This regime is called flux creep. Then, the relation between E and J is strongly nonlinear: $E \propto J^n$, with $n \gg 1$. As this regime is generally encountered in practice, we explain it in more details in the next section.

4.3.1 Flux creep and constitutive law $\mathbf{E} \propto \mathbf{J}^n$

Anderson's flux creep theory [117, 118] was developed in parallel with tube magnetization measurements carried out by Kim [110]. In these experiments, a time logarithmic decay of superconducting currents in LTS tubes under constant applied field was observed. This behaviour cannot be predicted by the Bean model. The experimental results were explained in term of a thermal activation of vortices out of their pinning wells, called flux creep. Once depinned, vortices move in the direction of the Lorentz force, $\mathbf{F}_{\mathrm{L}}$, reducing the spatial variation of the magnetic induction in the material. From $\nabla \times \mathbf{B} = \mu_0 \mathbf{J}$, this decrease induces a decay of the superconducting currents. The flux creep model differs from the Bean model, in that only quasi-equilibrium states are possible because of the thermal activation of vortices.

According to the conventional Arrhenius relation, a hopping time, t, is given in terms of the activation energy for depinning, U [111]:

$$t = t_0\,\mathrm{e}^{U/kT}, \tag{4.10}$$

where t_0 is the effective hopping attempt time, and k is the Boltzmann constant. The hopping process is assisted by the driving force $\mathbf{F}_{\mathrm{L}} = \mathbf{J}\times\mathbf{B}$. Therefore, U should be a decreasing function of J, and must vanish at J_{c}. In a first approximation, the net barrier reduces linearly with J, according to

$$U(J) = U_0(1 - J/J_{\mathrm{c}}), \tag{4.11}$$

where U_0 is the barrier height in the absence of a driving force. Combining (4.10) and (4.11), we obtain

$$J = J_{\mathrm{c}}\left[1 - \frac{kT}{U_0}\ln(t/t_0)\right]. \tag{4.12}$$

Equation (4.12) is often referred to as the Anderson-Kim equation for flux creep. It predicts the temporal logarithmic decay of currents observed by Kim.

Later versions of flux creep theory considered nonlinear $U(J)$ dependencies [55, 111]. For instance, a logarithmic barrier,

$$U(J) = U_0 \ln(J_{\mathrm{c}}/J), \tag{4.13}$$

was proposed by Zeldov et al. [119].

A closed relation can be established between the flux creep and the $E - J$ curve of a superconductor. Its origin lies in the fact that depinned moving vortices which experience the Lorentz force, induce an electric field $\mathbf{E} = \mathbf{B} \times \mathbf{v}$, where $\mathbf{v}$ is the average velocity of the flux lines in the direction of the Lorentz force. When pinning is important, the average velocity associated with the thermally activated flux lines is $v = v_0 \exp\left[-U(J)/kT\right]$ [111, 114], where v_0 is the velocity with no barrier. When flux lines are moving in a perpendicular magnetic induction B, the generated electric field is $E = B\,v$. Using (4.13), one obtains

$$E = E_{\mathrm{c}}\left(\frac{J}{J_{\mathrm{c}}}\right)^{n}, \tag{4.14}$$

with $n = U_0/kT$, and $E_{\mathrm{c}} = B\,v_0$. Flux creep corresponds to $kT \ll U_0$, hence to $n \gg 1$. The $n \to \infty$ limit corresponds to the Bean model, whereas $n = 1$ corresponds to a normal conducting material or to a superconductor in the (thermally assisted) flux flow regime.

From (4.14), the current density can take any value, and the electric field is never zero. Hence, at finite temperatures, the definition of J_c is not obvious: regardless of the value of J, there is always some flux motion, and therefore some loss. True critical current density is an inaccessible theoretical construct, and J_c is generally defined by a voltage criterion. Often, J_c is the value of the critical current density which leads to an electric field of 1 μV/cm.

The power law (4.14) has been shown to hold in many experiments and is often used with a n value typically larger than 20 to model HTS. For such large n values, the electric field, i.e. the dissipation, is very small if $J < J_c$, and strongly increases for higher current densities. Hence, J_c represents a practical limit between regimes with small and large losses.

The strong nonlinearity of (4.14) leads to a nonlinear diffusion of the magnetic field through a HTS. The magnetic diffusion coefficient, D, is related to the resistivity $\rho = E/J$ by $D(J, B, T) = \rho(J, B, T)/\mu_0$.

Scaling laws

The constitutive law (4.14) gives rise to frequency scaling laws with n-dependent power exponents [22, 120]. The scaling laws can be obtained by changing the time unit in the Maxwell equations by a factor $c > 0$: $t \longmapsto t_{\text{new}} = t/c$. Given a solution with a current density $\mathbf{J}(\mathbf{r}, t)$, an applied induction $\mathbf{B}_{\text{a}}(\mathbf{r}, t)$, and a total induction $\mathbf{B}(\mathbf{r}, t)$, new solutions can be found that satisfy

$$\begin{aligned} \mathbf{J}_{\text{new}}(\mathbf{r}, t_{\text{new}}) &= \mathbf{J}(\mathbf{r}, t) c^{1/(n-1)}, && (4.15) \\ \mathbf{B}_{\text{new}}(\mathbf{r}, t_{\text{new}}) &= \mathbf{B}(\mathbf{r}, t) c^{1/(n-1)}, && (4.16) \\ \mathbf{B}_{\text{a,new}}(\mathbf{r}, t_{\text{new}}) &= \mathbf{B}_{\text{a}}(\mathbf{r}, t) c^{1/(n-1)}. && (4.17) \end{aligned}$$

Transposed to the frequency domain, these relations imply that, if the frequency of the applied field is multiplied by a factor c, then the current density and the magnetic induction are rescaled by the factor $c^{1/(n-1)}$. In the $n \to \infty$ limit (Bean model), current and field distributions are not affected when changing the frequency.

We now turn to the geometric limitations of the Bean model.

4.4 Geometric limitations of the Bean model

When we have explained the Bean model and the method of Campbell and Evetts, we have considered an infinitely long tube subjected to a uniform axial magnetic induction. The reason is that the Bean model cannot take into account the geometric effects. But, in real HTS, the demagnetizing effects are present and can be important.

The Bean model suffers another geometric limitation. The Bean model is based on the idea that for any applied field, the driving Lorentz force, $\mathbf{F}_{\text{L}} = \mathbf{J} \times \mathbf{B}$, is exactly balanced by the pinning force, $\mathbf{F}_{\text{P}}$, see (4.7). Only the component of the current density that flows perpendicular to the flux lines is capable of setting the vortices into motion. Hence, the equilibrium (4.7) imposes that the component of current density perpendicular to flux lines, $J_\perp$, is equal to J_c:

$$J_\perp = J_c, \tag{4.18}$$

but says nothing about the component of **J** parallel to **B**. The Bean model is therefore limited to those geometries where **J** always flows perpendicular to **B** [121].

Geometries for which **J** is not perpendicular to **B** require a special treatment. When the component of the current density that is parallel to the magnetic induction, $J_{||}$, reaches a critical value, $J_{\mathrm{c}||}$, Clem's double critical state occurs [122, 123]. However, in many situations, $J_{||}$ does not reach $J_{\mathrm{c}||}$. In these cases, the distribution of **J** cannot be determined from the Bean model alone [121]. Additional information about $J_{||}$ must be obtained from the history of the field configuration. Recently, Mikitik and Brandt solved such a problem for an infinite slab of finite thickness in a perpendicular magnetic field, subjected to an additional magnetic field of small amplitude applied parallel to the plate [121].

In this manuscript, we focus on situations for which $\mathbf{J}\perp\mathbf{B}$. The corresponding geometries are given in the next section.

4.5 Study of the field penetration into geometries with demagnetizing effects

To obtain the constitutive law $E \propto J^n$ (see (4.14)), we used the fact that the pinning barrier height, U, is reduced by the Lorentz force. As only $J_\perp$ participates to the Lorentz force, the law (4.14) only determines the current density component perpendicular to the flux lines, as the Bean model does. Geometries for which a current density component parallel to B exists cannot be solved with the only constitutive law (4.14).

The current density is perpendicular to the magnetic induction for specific 1D, 2D, and axisymmetric geometries [124]. As an example, for the method of Campbell and Evetts that we have explained in section 4.1, the sample is infinitely long and a magnetic field is applied parallel to the infinite dimension. It follows that the current flows in a plane perpendicular to **B**.

In this section, we consider two other geometries for which $\mathbf{J}\perp\mathbf{B}$ and present a numerical method to study the field penetration in such geometries. We first focus on axial symmetric geometries, and more specifically a tube with a uniform magnetic field applied parallel to the sample axis. Such a geometry has a great practical interest for the shielding application: tubes can easily be made and nearly closed screens are expected to give high shielding factors. For axial symmetric geometries, the current flows along concentric circles which are perpendicular to **B**. After, we consider infinitely long samples in a uniform transverse field. Then, the current is directed along the infinite specimen dimension again perpendicular to **B**. First, let us consider the axial symmetric geometry.

4.5.1 Axial symmetric geometries

We work with cylindrical coordinates, so that positions are denoted by (r, φ, z), where the z-axis is the axis of revolution. The axial symmetry imposes that the different fields do not vary with φ. We further assume that:

$$B_\varphi = 0. \tag{4.19}$$

From

$$\nabla \times \mathbf{B} = \mu_0 \mathbf{J}, \tag{4.20}$$

we deduce:

$$J_\mathrm{r} = 0, \qquad \mu_0 J_\varphi = \frac{\partial B_\mathrm{r}}{\partial z} - \frac{\partial B_\mathrm{z}}{\partial r} \qquad J_\mathrm{z} = 0. \tag{4.21}$$

The current density, $\mathbf{J}$, thus has only one component and $\mathbf{J} \perp \mathbf{B}$.

Different numerical methods exist to study the field penetration into superconducting samples with an axial symmetry. Prigozhin proposed a variational formulation [124]. He formulates the problem in terms of the current density, which is to be determined only in the region occupied by the superconductor. Once the current distribution is known, the magnetic field is calculated from the Biot-Savart law. It is also possible to obtain a nonlinear diffusive equation for the current density. Only one equation has to be solved, as the current density is directed along $\hat{\varphi}$. The diffusive equation can be solved by the finite differences method [125]. The main disadvantage is the difficulty of using the finite differences method with complex geometries. Hence, several authors preferred the finite elements method (FEM) [27, 126] which can be applied more easily to various geometries. Element-free Galerkin method has also been used to calculate the field penetration into axisymmetric HTS [127]. Finally, Sanchez and Navau [128, 129] proposed a method based on the magnetic energy minimization. This method has been developed for the case $n \to \infty$, i.e. $J = 0$ or $J = J_\mathrm{c}$. Chen et al. [130] used this method to calculate the complex ac susceptibility of irreversible type-II superconducting cylinders.

We decided to follow Brandt's approach [120]. Unlike the finite elements method, Brandt's approach can be easily implemented on a personal computer with standard numerical tools. The formulation is also simple, as it is based on the discretization of the Biot-Savart law. One has to solve an equation of motion for the current density flowing only in the superconductor. The equation to solve can be easily extended to geometries other than the axial symmetric geometry, if one has $\mathbf{J} \perp \mathbf{B}$. The exact geometry is taken into account by an integral kernel. Using an adaptive time step proposed by Brandt, the algorithm converges even for high n values ($n > 50$).

The numerical method of Brandt

The numerical method of Brandt is based on the discretization of the Biot-Savart integral equation. To set up the main equations, we closely follow [120]. The method applies to any axial symmetric geometry (sphere, cone, ...). For the sake of simplicity, we consider the tube of figure 4.4 to explain the algorithm. The tube is symmetric with respect to the plane $z = 0$, has an inner radius a_1, an outer radius a_2, a length ℓ, and is subjected to a uniform magnetic induction $\mathbf{B}_\mathrm{a} = B_\mathrm{a}\, \hat{z}$.

As the magnitude of the axial induction, B_a, is increased, the induced electric field and the resulting current density assume the form

$$\mathbf{J} = -J(r,z)\, \hat{\varphi}, \quad \mathbf{E} = -E(r,z)\, \hat{\varphi}, \tag{4.22}$$

where $\hat{\varphi}$ is the unit vector in the azimuthal direction. The magnetic induction is invariant under a rotation around the z-axis and has no φ-component. Thus,

$$\mathbf{B}(r,z) = B_r(r,z)\, \hat{r} + B_z(r,z)\, \hat{z}. \tag{4.23}$$

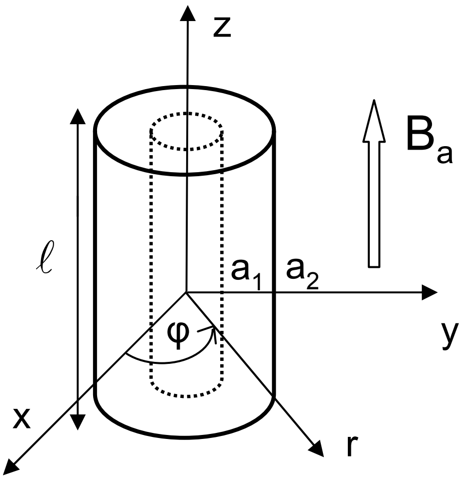

Figure 4.4: tube of internal radius a_1, external radius a_2, and length ℓ subjected to a uniform axial magnetic induction $\mathbf{B_a} = B_\mathrm{a}\,\hat{z}$.

In order to avoid an explicit and costly computation of the magnetic induction $\mathbf{B}(\mathbf{r}, t)$ in the infinite region exterior to the tube, an equation of motion is first established for the macroscopic shielding current density, $\mathbf{J}(\mathbf{r}, t)$, since its support is limited to the volume of the superconductor. The magnetic field is then obtained where required by integrating the Biot-Savart law.

The magnetic induction, $\mathbf{B}$, can be expressed by:

$$\mathbf{B} = \nabla \times \mathbf{A}, \tag{4.24}$$

where the magnetic vector potential, $\mathbf{A}$, satisfies:

$$\mathbf{A} = -A(r, z)\,\hat{\varphi} = -(A_\mathrm{ind} - A_\mathrm{a})\,\hat{\varphi}. \tag{4.25}$$

The first term, A_ind, results from the macroscopic shielding currents flowing inside the sample. The second contribution, A_a, is the magnetic vector potential of the applied induction, that means $\mathbf{B}_\mathrm{a} = \nabla \times \mathbf{A}_\mathrm{a}$.

Noting that $A_\mathrm{a} = (r/2)\,B_\mathrm{a}$, and using the Biot-Savart law, one can obtain

$$A(\mathbf{r}) = \mu_0 \int_{a_1}^{a_2} \int_0^{\ell/2} \mathrm{d}r'\mathrm{d}z' Q(\mathbf{r}, \mathbf{r}') J(\mathbf{r}') - \frac{r}{2} B_a, \tag{4.26}$$

where $\mathbf{r}$ and $\mathbf{r}'$ are shorthands for (r, z) and (r', z'), while $Q(\mathbf{r}, \mathbf{r}')$ is a kernel which only depends on the sample geometry. In the present case, Q assumes the form

$$Q(\mathbf{r}, \mathbf{r}') = f(r, r', z - z') + f(r, r', z + z') \tag{4.27}$$

where

$$f(r, r', \eta) = \int_0^{\pi} \frac{r' \cos\varphi}{2\pi\sqrt{\eta^2 + r^2 + r'^2 - 2rr'\cos\varphi}}\,\mathrm{d}\varphi, \tag{4.28}$$

is to be evaluated numerically as suggested in [120]. Taking the time derivative of (4.26), and using $\nabla \times \mathbf{E} = -\partial \mathbf{B}/\partial t$, one has

$$E(J) = -\mu_0 \int_{a_1}^{a_2} \int_0^{\ell/2} Q(\mathbf{r}, \mathbf{r}') \dot{J}(\mathbf{r}') + \frac{r}{2} \dot{B}_a, \tag{4.29}$$

where $\dot{J}$ represents the time derivative of the current density.

The equation of motion for J is then obtained in three steps. First, the electric field is eliminated from (4.29) by using a constitutive law linking the electric field and the current density. To model HTS in the flux creep regime, one can use the law (4.14). Second, the equation is discretized on a two-dimensional grid with spatial steps Δr and Δz. Third, the resulting matrix equation is inverted, yielding the relation

$$\dot{J}_i(t) = \frac{1}{\mu_0 \Delta r \Delta z} \sum_j Q_{ij}^{-1} \left\{ \frac{r_j}{2} \dot{B}_a - E\left[J_j(t)\right] \right\}. \tag{4.30}$$

Here, J_i and Q_{ij} are shorthands for $J(\mathbf{r}_i)$ and $Q(\mathbf{r}_i, \mathbf{r}_j)$.

Imposing the initial condition

$$J_i(t = 0) = 0 \quad \forall i, \tag{4.31}$$

the current density can be numerically integrated over time by updating the relation

$$J_i(t + \Delta t) \cong J_i(t) + \dot{J}_i(t)\, \Delta t, \tag{4.32}$$

where $\dot{J}_i$ is evaluated as in (4.30) and Δt is chosen suitably small. An adaptative time step procedure described in [120] makes the algorithm converge towards a solution that reproduces the experimental data fairly well (see chapter 6).

Logarithmic singularity of the integral kernel Q. From (4.27) and (4.28), we see that the integral kernel Q diverges as $\mathbf{r}'$ tends to $\mathbf{r}$. To avoid this singularity, Brandt suggests to replace η^2 by $\eta^2 + \epsilon^2$ in (4.28), ϵ^2 being a small quantity compared to the size of a grid element. In [120], ϵ^2 is chosen in an empirical way equal to $0.015\, \Delta r \Delta z$ in order to have zero magnetic induction before the flux front and no oscillating current densities.

Such a singularity is often encountered in electromagnetic fields calculations. The equation (4.26) is the solution in cylindrical coordinates of the Poisson equation $\nabla^2 \mathbf{A} = -\mu_0 \mathbf{J}$, and can be obtained by integrating the corresponding Green function, solution of the Poisson equation for a point and unit source. Green functions diverge as $\mathbf{r}' \to \mathbf{r}$, but one can show that the singularity can be integrated around $\mathbf{r}' = \mathbf{r}$. Boundary elements method uses Green functions, and treat their singularity by integrating them locally around $\mathbf{r}' = \mathbf{r}$. We tried this approach with the constitutive law (4.14). It led to bad convergence, and to large oscillating currents. We explain such a result by the strong nonlinearity of the law $E \propto J^n$ which needs very small grid elements if one wants to integrate locally the Green function. In general, the method of integrating locally the Green function around $\mathbf{r}' = \mathbf{r}$ is indeed done for linear materials (ohmic materials), and with many grid elements.

Hence, as suggested by Brandt, we introduced the parameter ϵ^2 to solve the problem of singularity. Then, one does not need to take a large number of elements.

Typically, we used around 700 elements to calculate the current distribution, and the calculation time lies around 12 hours to obtain a whole hysteresis curve. Note that the resolution of (4.30) is not performed by calculating explicitly the inverse of the kernel Q, but rather by using the Gauss elimination method [131].

The equations that we have presented in this section can be used for another geometry, an infinitely long sample in a perpendicular field. Only the integral kernel has to be modified. We focus on this geometry in the next section.

4.5.2 Infinitely long samples in a transverse magnetic field

The geometry of infinitely long bars in a transverse magnetic field is very similar to the axial symmetric geometry presented in the previous section. The geometry studied in this section is shown in figure 4.5. The specimen is infinite along the z-axis, and the applied induction, $\mathbf{B}_\mathrm{a}$, located in the $x-y$ plane, does not depend upon the z coordinate. For the sake of simplicity, we consider the example of a specimen with a rectangular cross-section, which is subjected to the uniform magnetic induction $\mathbf{B}_\mathrm{a} = B_\mathrm{a}\,\hat{x}$.

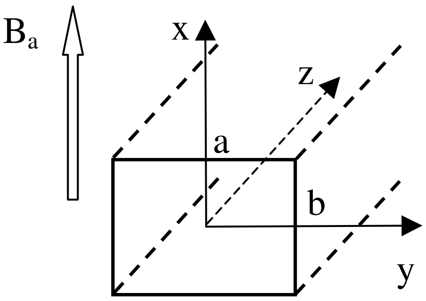

Figure 4.5: infinitely long sample in the $\hat{z}$ direction, with a uniform applied induction located in the $x-y$ plane.

From the Maxwell equation $\nabla \times \mathbf{B} = \mu_0 \mathbf{J}$, we deduce:

$$J_\mathrm{x} = 0, \qquad J_\mathrm{y} = 0, \qquad \mu_0 J_\mathrm{z} = \frac{\partial B_\mathrm{y}}{\partial x} - \frac{\partial B_\mathrm{x}}{\partial y}. \tag{4.33}$$

Hence, $\mathbf{J} \perp \mathbf{B}$.

As for the axial symmetric geometry, the current density has only one component and the different numerical methods explained in the previous section can also be used, with minor changes, in these cases. Prigozhin used his variational method to study the field penetration into bars of various cross-sections in [124, 132]. The finite elements method has also been used to calculate the current distribution, the electromagnetic fields, and the AC losses in superconducting cables [133, 134, 135], assuming that their extension is infinite.

The method of Brandt can also be used for the geometry of figure 4.5 [136]. Then, the equation of motion (4.30) is computed with the kernel

$$Q(\mathbf{r}, \mathbf{r}') = \frac{\ln|\mathbf{r} - \mathbf{r}'|}{2\pi}, \tag{4.34}$$

while, for the uniform magnetic induction $\mathbf{B}_\mathrm{a} = B_\mathrm{a}\,\hat{x}$, we have $\mathbf{A}_\mathrm{a} = yB_\mathrm{a}\,\hat{z}$. Here, $\mathbf{r} = (x, y)$ and $\mathbf{r}' = (x', y')$, whereas the integral of (4.26) is carried over the domain $|x| < a$ and $|y| < b$. In chapter 6, we use this method to study the field penetration into HTS tubes in a perpendicular magnetic field.

Hence, the method of Brandt is general. Following the same method, one can calculate the field distribution in an infinitely thin film subjected to a perpendicular uniform magnetic field. Then, the current flows in a plane perpendicular to **B**. The equations to solve in such a case are explained in appendix A.

4.6 Summary

Using Bean's ideas, it is possible to study the field penetration into infinitely long samples of arbitrary cross-section if the magnetic field is applied parallel to the infinite dimension. Then, the contours of constant B, which are also the lines of current flow, are parallel to the sides of the cross-section.

Rather than using a constant critical current density, $\mathbf{J}_\mathrm{c}$, one could use a decreasing current density with the magnitude of the magnetic induction, **B**. Such a dependence is particularly important for polygranular HTS. To take the dependence $J_\mathrm{c}(B)$ into account, we have introduced the Kim model (4.6) in section 4.2.

Two assumptions of the Bean model can be very limiting when studying real HTS samples. First, the Bean model assumes that there is always an equilibrium between the Lorentz force, which tends to move vortices, and the pinning force, which retains them. It is also assumed that no other effect than the Lorentz force can depin vortices. The corresponding relation between the current density, J, and the electric field, E, is shown in figure 4.3. If $J < J_\mathrm{c}$, $E = 0$. When $J > J_\mathrm{c}$, $E \to \infty$. In reality, $E \neq \infty$ if $J > J_\mathrm{c}$, and other factors than the Lorentz force can depin vortices, such as thermal energy. Thermal effects are particularly important for HTS due to their small pinning energies, and due to the relatively high temperatures involved when using HTS. Depending on the importance between thermal effects and effects linked to the Lorentz force, different regimes are involved. Flux creep, which is often encountered in the applications using HTS, corresponds to the regime for which a high current density is required for moving vortices at finite temperature. In this case, the relation between the electric field and the current density is a highly nonlinear power law:

$$E = E_\mathrm{c}\left(\frac{J}{J_\mathrm{c}}\right)^n, \tag{4.35}$$

with $n \gg 1$. Such a relation gives rise to scaling laws.

Second, the Bean model assumes that the demagnetizing factor is zero. Hence, only infinite samples with a parallel magnetic field can be studied rigorously.

The calculation of the field penetration into HTS of arbitrary geometry is a challenging task [121]. Here, we focus on cases for which $\mathbf{J}\perp\mathbf{B}$. For such geometries, the constitutive law (4.35) can be used to determine the total current density.

More specifically, we consider axial symmetric geometries and infinite samples in a transverse magnetic field. In the first case, the current flows along concentric circles. In the second case, the current is directed along the infinite sample dimension. For such geometries, Brandt proposed a numerical method which is based on the discretization of the Biot-Savart law. In chapter 6, using this method and the constitutive law (4.35), we study the field penetration into HTS tubes in an axial and transverse magnetic field.

Before presenting these theoretical results, we show in the next chapter some characterizations obtained with EPD planar samples.

Chapter 5

Superconducting and shielding properties of planar HTS samples

In the previous chapters, we have discussed the magnetic shielding properties of high-temperature superconductors (HTS). We have also explained the principle of the electrophoretic deposition (EPD) technique used to make HTS shields. This technique allows one to deposit a Y-123 film on a metallic substrate. To optimize the process parameters and to check that the EPD coatings are superconducting, it was necessary to characterize the samples.

In this chapter, we focus on electrical and magnetic measurements carried out with planar samples, which means that the EPD coating is deposited on planar metallic substrates. The electrical characterizations allow one to check the existence of a macroscopic superconducting path, and to evaluate the critical current density of the coating. Magnetic measurements were used to determine the critical temperature of the grains of the coating, and to measure the field attenuation realized by a planar sample subjected to a low frequency magnetic field. For some characterizations, we used a commercial system (Quantum Design PPMS). Because of geometric constraints, it was also necessary to build our own system for some magnetic shielding measurements.

The chapter is organized as follows. First, we present the different measurement systems that we use in this chapter. In section 5.2, we give the results of a shielding measurement carried out with a sample whose grains are superconducting but not well connected, which means that there is no macroscopic superconducting transition. Afterwards, we focus on coatings whose grains are well connected. In section 5.3, we present characterizations of superconducting layers on nickel substrates. In section 5.4, we consider coatings on silver. We measured their critical current density, the field dependence of J_c, and the shielding effect of a 4 cm × 4 cm EPD coating whose thickness is around 50 μm.

5.1 Characterization techniques

To characterize the superconducting and shielding properties of the EPD coatings, we used several techniques. Some electrical and AC magnetic measurements were carried out with a commercial physical property measurement system (PPMS) from

Quantum Design. This device can perform characterizations from $T = 2$ K to $T = 350$ K. To enter the PPMS chamber, the maximum allowed area of the EPD coating is 1 cm^2. Therefore, we have also designed home-made systems for larger samples. In particular, we have built our own experimental setup to determine the shielding properties of the EPD samples. Coatings with a surface up to 50 cm^2 can be studied with this setup.

In the next sections, we explain the principles of each characterization technique.

5.1.1 Electrical transport measurements

The electrical transport measurements refer to the measurements of the electrical resistance and the critical current density of the EPD coatings.

By measuring the electrical resistance of the deposited layer as a function of temperature, one can check the existence of a macroscopic superconducting path. If the coating is superconducting, a graph similar to that of figure 5.1 is obtained. As the temperature decreases, the resistance drops at the critical temperature, $T_c \cong$ 90 K here, and is too small to be measured below T_c. For a polycrystalline material, if the grains are not connected, such a transition does not occur even though the grains are superconducting below a critical temperature.

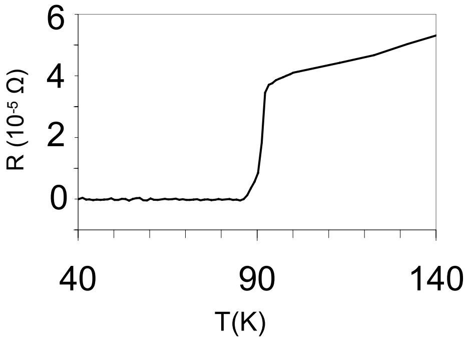

Figure 5.1: typical transition measured for a superconducting EPD sample. For $T < T_c \cong 90$ K, the Y-123 layer presents a macroscopic superconducting path, and the resistance is no longer measurable.

Once knowing that a macroscopic superconducting path exists, it is of interest to measure the critical current density, J_c. Then, using the Bean model, one can estimate the maximum magnetic induction that the EPD samples can efficiently shield, $B_{\mathrm{lim,Bean}}$ (see section 2.5.1). As a reminder, we determined $B_{\mathrm{lim,Bean}} = \mu_0 H_{\mathrm{P}}$, where the full penetration field, H_{P}, is directly proportional to J_c.

As we are concerned with low impedance measurements, both resistance and J_c measurements are based on the conventional 4-probe technique [137]. This measurement method is illustrated in figure 5.2. A current of known value is injected through the sample via the outer pair of leads and the voltage due to the material resistance is measured across the inner pair of leads. The leads must be in contact with the sample with the smallest possible contact resistance. The sensitivity is higher when using long samples of small cross-section.

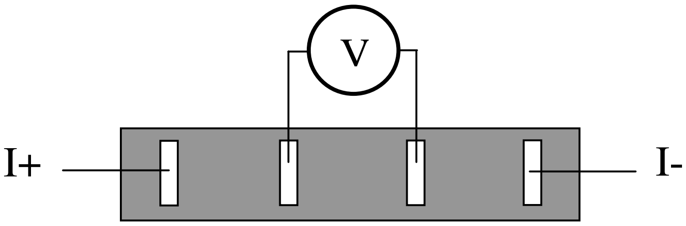

Figure 5.2: the 4-probe technique principle.

The resistance measurement is carried out with thin copper wires (diameter equal to 80 μm), electrically connected to the sample with silver paste. The input current is a low frequency AC signal (30 Hz) with an amplitude ranging between 10 μA and 2 A. Knowing the current flowing in the sample, and the voltage across the two inner contacts, one can determine the electrical resistance between the two inner leads. The use of an AC current gives measurements of higher sensitivity than measurements carried out with a DC current, because synchronous detection techniques can be employed to significantly increase the signal to noise ratio. Besides, thermoelectric effects do not alter the measured signal, as the current polarity is reversed at each cycle. With the PPMS, the resistance measurement can be carried out from 2 K to 350 K, with a magnetic induction up to 9 T, applied perpendicular to the sample plane.

The $I - V$ curve of a HTS is strongly non-linear in the flux creep regime, see chapter 4. Below the critical current, I_c, the voltage, V, is very small; for higher currents, V strongly increases. The critical current I_c is determined by a criterion. Generally, I_c is equal to the flowing current for which the resulting electric field is 1 μV/cm. We used this definition to determine I_c of the EPD coatings.

When critical current measurements are carried out with the PPMS, the maximum allowed surface of the coating is 1 cm^2. Therefore, we also used a home-made setup allowing us to determine I_c for larger samples, but only at 77 K, and without any applied magnetic induction. Then, the sample is immersed in liquid nitrogen, and fed by a DC current (power supply SM 70-22 from Delta Electronika). The voltage is measured with a nanovoltmetre (model HP34420).

5.1.2 AC magnetic measurements

When the electrical resistance of an EPD coating fails to vanish under a critical temperature, two situations are possible. First, the grains may never become superconducting, a situation which can result from a bad oxygen treatment. Second, the grains may be superconducting but not well connected. Then, the measurement of the AC magnetic moment of the powder scratched from the coating allows one to check whether the different grains are superconducting.

Above the critical temperature of the grains, the magnitude of the real part of the AC magnetic moment, m', measured by means of a small AC applied magnetic field, is expected to be very small, as Y-123 is not a good conductor above T_c. When the grains become superconducting, they prevent the applied field from penetrating them. Hence, m' becomes negative below T_c [19, 20]. By measuring the real part of the AC magnetic moment of the powder scratched from the coating as a function of temperature, one can check whether the different grains are superconducting, and determine their critical temperature.

The measurement of the AC magnetic moment at various temperatures can be performed with the PPMS. The sample is subjected to a small alternating field generated by a primary coil, and the magnetic response is measured by two sensing coils surrounding the sample.

5.1.3 Shielding characterization of planar samples

We now turn to describing our home-made system for measuring the shielding properties of planar samples. The principle of the measurement is shown in figure 5.3. An AC magnetic field is applied by a small source coil (length: 2.2 mm, diameter: 6 mm), named 1 in figure 5.3. This coil has 303 turns. The magnetic induction on the other side of the sample, which is named 2 in figure 5.3, is measured by a sensing coil (named 3 in figure 5.3) of identical geometry as the source coil. The two coils have the same axis of revolution (z-axis). The distance between the coils is 5 mm and the sample is placed exactly in the middle. A photograph of the setup, which can be immersed in liquid nitrogen, is shown in figure 5.4 and the source coil is shown in figure 5.5.

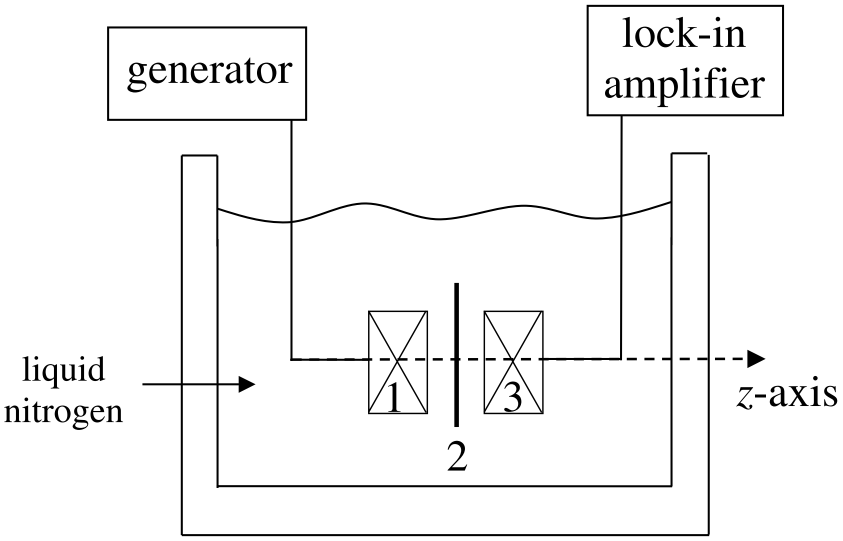

Figure 5.3: magnetic shielding measurement system for planar samples. The source coil (number 1) is connected to the generator HP8904A, and the sensing coil (number 3) is connected to the lock-in amplifier EGG7260. The sample is represented by number 2.

The z component of the local magnetic induction at the sensing coil is determined from its voltage, which is measured by a lock-in amplifier (EGG7260 model). The shielding properties are evaluated as follows: the magnetic induction at the centre of the sensing coil is measured both in the absence (B_{abs}) and in the presence (B_{pres}) of the sample. We then compute the ratio $B_{\text{abs}}/B_{\text{pres}}$. As HTS have

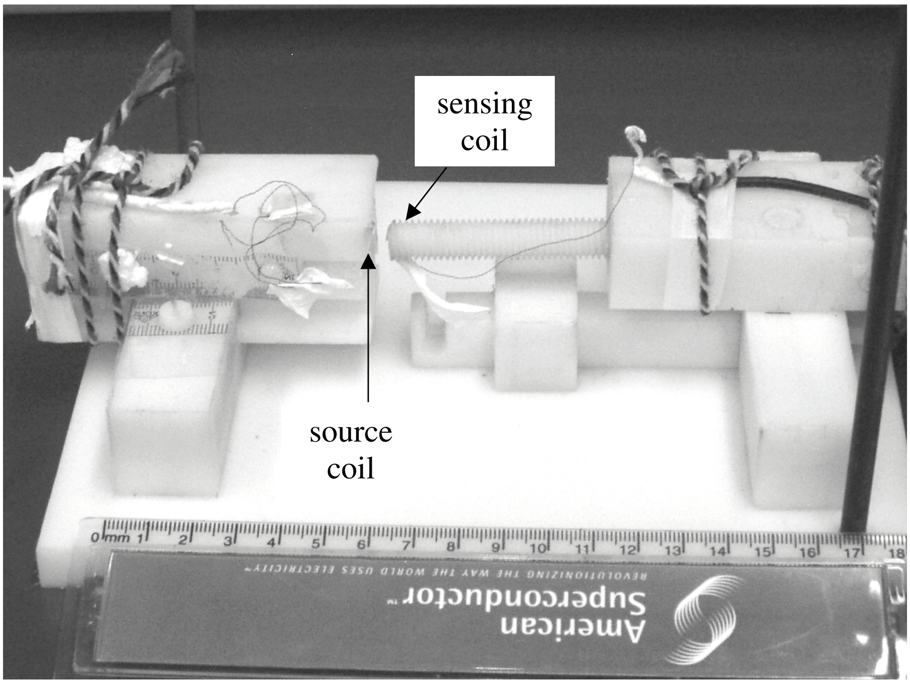

Figure 5.4: photograph of the system designed to evaluate the shielding properties of planar samples. The setup can be immersed in liquid nitrogen.

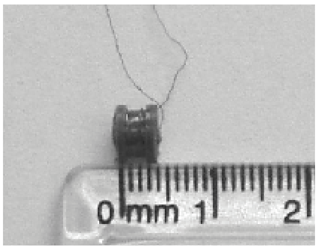

Figure 5.5: photograph of the source coil of the measurement system of figure 5.4.

non-linear magnetic properties, the magnetic induction measured with the sample can have different harmonics. We measure the fundamental component of B_{pres}, as this component strongly dominates the other harmonics. For the EPD samples, the measurements are carried out in liquid nitrogen, $T = 77$ K. The source coil is connected to a generator HP8904A and the amplitude of the applied magnetic induction can reach 10 mT. At 103 Hz, the minimum magnetic induction that can be detected by the sensing coil is around 10 nT. Both the generator and the lock-in amplifier are connected to a computer through IEEE-488 interface, to allow automatic measurements. The interested reader can find more details about this setup in [138].

5.2 Shielding properties of Y-123 coatings with non-connected grains

In section 3.4.2, we explained the difficulties of the thermal treatment which applies to the EPD coating after the deposition step. Because of the metallic substrate, one cannot heat the sample near the peritectic temperature of the YBaCuO system, T_{P} =1015° C. One could wonder whether a heat treatment near T_{P} = is useful for shielding applications. In this section, we experimentally study the superconducting and shielding properties of Y-123 coatings which were not heated near T_{P} =1015° C.

We consider EPD Y-123 coatings on silver, which underwent a heat treatment at the maximum temperature of 925° C. After this step, an oxygen annealing at 500° C for 30 h was applied to the samples. The temperature of 925° C is close to the maximum one that the silver substrate can support before losing its mechanical stability. But this temperature is much lower than the peritectic temperature of YBaCuO, T_{P} =1015° C. For such a heat treatment, one expects to have coatings with superconducting, but disconnected, grains.

To carry out this study, we use two planar samples, called sample 1 and sample 2, which were synthesized in the same conditions. The thickness of the silver substrate is 1 mm and the thickness of the coating is around 50 μm. Samples 1 and 2 differ by their geometric size: sample 1 is a 1 cm × 1 cm coating, whereas sample 2 is a 4 cm × 4 cm one. Sample 1 is used for the superconducting characterizations, and sample 2 for the shielding ones.

The resistance measurement made with sample 1 (not shown here), using the method of section 5.1.1, clearly indicates that the different grains are effectively not connected as there is no superconducting transition. No macroscopic superconducting current can flow in the coating. However, a measurement of the AC magnetic moment, m, of the powder scratched from the coating of sample 1 shows a transition, hinting at the onset of superconductivity in the grains. We made the measurement with an AC applied magnetic induction having a frequency of 1053 Hz and a magnitude of 1 mT.

The real part of m versus temperature is shown in figure 5.6. We observe that there is a transition at $T_{\mathrm{c}} \cong 90$ K. Above this temperature, the real part of m, m', is zero, and below T_{c}, m' is negative. This shows that the grains become superconducting at $T_{\mathrm{c}} \cong 90$ K.

Knowing that the different grains of sample 1 are superconducting but not connected, we now turn to the shielding properties of sample 2. To carry out this study, we use the experimental setup described in section 5.1.3. An AC magnetic induction is applied to sample 2 by the source coil, and the magnetic induction behind the sample is measured by the sensing coil. The distance between the coils is 5 mm and the sample is placed in the middle. The measurement is carried out in liquid nitrogen (T = 77 K) and at a frequency of 103 Hz.

Figure 5.7 shows the ratio between the magnetic inductions measured at the sensing coil in the absence (B_{abs}), and in the presence (B_{pres}) of sample 2, for different values of the applied induction. We see that the ratio is nearly constant and equal to ~ 1.2, which means that there is nearly no field attenuation at all.

In fact, the small field attenuation can almost completely be attributed to the

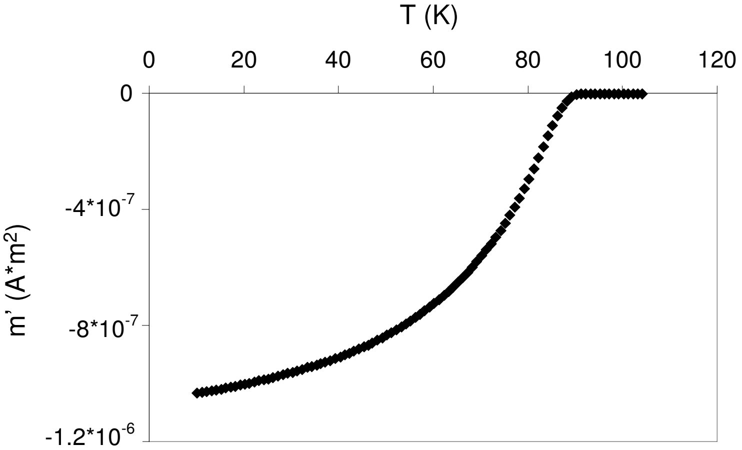

Figure 5.6: real part of the AC magnetic moment of the powder scratched from sample 1 versus temperature. Sample 1 is an EPD Y-123 coating on silver with non-connected grains. This measurement shows that the different grains are superconducting below ~ 90 K.

silver substrate. Taking an electrical resistivity of 0.3 $\mu\Omega\,\mathrm{cm}$ for silver at 77 K [139], we have a skin depth equal to $\delta \cong 2.7$ mm at 103 Hz. From chapter 1, we deduce that the shielding factor of the silver substrate is about

$$\frac{B_{\mathrm{abs}}}{B_{\mathrm{pres}}} \cong \mathrm{e}^{t/\delta} \cong 1.45, \tag{5.1}$$

where t is the substrate thickness (1 mm). The value of 1.45 is close to the measured one, 1.2. The expression (5.1) was deduced from an ideal case, assuming that an infinite plate is subjected to a parallel magnetic field. Such a situation differs from the experimental geometry, where the sample is of finite extension. This could explain the difference between the measured field attenuation and the expression (5.1). Thus, with such figures, it does not seem likely that the superconducting coating plays any role in the measured field attenuation.

The results show that a coating which has not any macroscopic superconducting path is not efficient for shielding applications, even if the grains are superconducting. We therefore focus on samples with connected grains in the next sections.

First, we present the superconducting properties of Y-123 coatings on nickel. After, we consider coatings on silver. In each case, we present the results which were obtained with optimized samples, resulting from a semi-empirical study of the process parameters to obtain the coatings with the highest T_{c} and J_{c} values. We do not give all the details of the samples preparation but we explain, in each case, how it is possible to obtain a dense coating with connected grains. The reader interested in the details of the samples preparation is referred to [70, 97, 98, 140, 141].

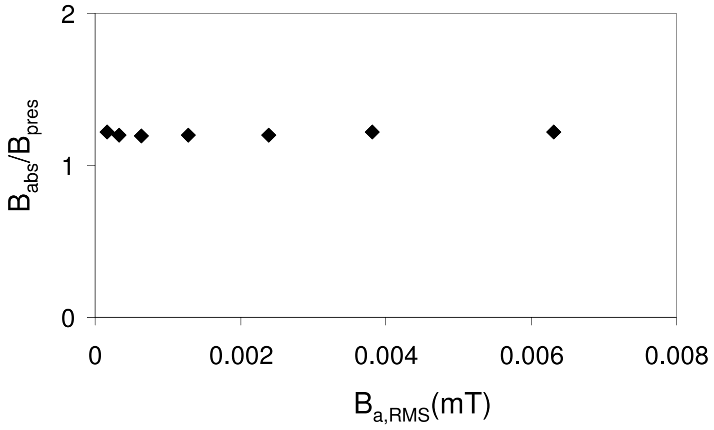

Figure 5.7: ratio between the magnetic inductions measured at the sensing coil without and with sample 2.

5.3 EPD coatings on nickel

The fusion point of nickel is higher than the peritectic temperature of the YBaCuO system, T_{P}. But, as nickel can destroy superconductivity of the Y-123 phase, one cannot heat the coating up to T_{P}, see section 3.4.2. In the past, it was shown that an atmosphere with poor oxygen content decreases T_{P} [70, 142, 143]. Hence a heat treatment under flowing argon was tested. Nevertheless, the obtained coatings turned out to be of poor quality: they do not adhere to the metallic substrate and have large cracks [141]. Besides, the non-superconducting Y-211 phase is present in great quantity. This is the reason why a heat treatment under air was used for coatings on nickel. The highest temperature to use during the heat treatment under air was found, empirically, to be 940° C. Higher temperatures lead to an excessive amount of nickel in the HTS layer; lower temperatures do not give a good connectivity between the grains.

Figure 5.8 shows the best result that we have obtained with a Y-123 EPD coating on nickel. This coating has been first heated to a maximum temperature of 940° C under air, and has then undergone a final step at 500° C under oxygen. We refer to this coating as sample 3.

We see that the superconducting transition of sample 3 is large: the resistance begins to decrease at $T = 80$ K, but only falls below the noise level at 58 K. This suggests that the connectivity between the grains is poor [20]. As observed by other authors [103, 104], above $T = 80$ K, the measured resistance of the Ni doped Y-123 layer exhibits a semiconductor like behaviour, i.e. the resistance decreases as the temperature increases. From [104], this semiconductor behaviour is observed when Ni ions occupy more than 8 % of the Cu sites. Note that we measure the resistance of the coating above T_{c}, and not the resistance of the substrate, because of the presence of nickel oxide (NiO) at the interface between the HTS layer and the substrate.

It seems that T_{c} cannot be increased by applying different heat treatments. This suggests that EPD coatings on nickel cannot be used for magnetic shielding at 77 K.

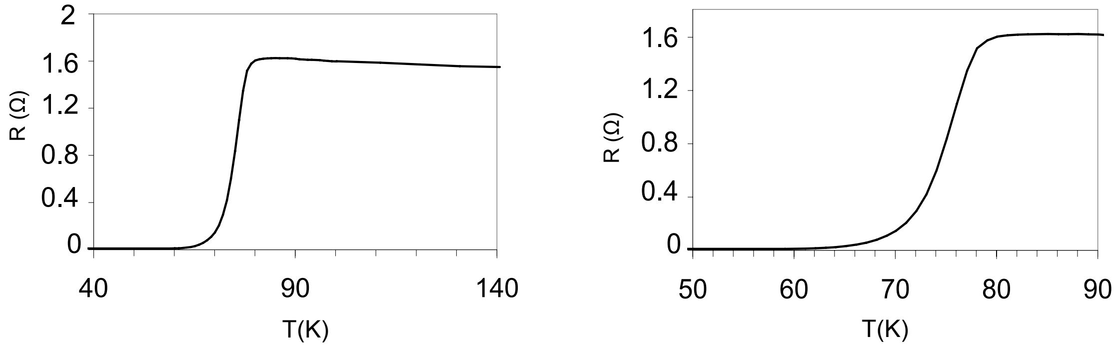

(a) (b)

Figure 5.8: (a) and (b): measured resistance of sample 3 (Y-123 coating on a nickel substrate), as a function of temperature. The resistance falls below the noise level at 58 K. Figure (b) is a zoom of figure (a) showing a large transition. We did not obtain coatings on nickel with a higher critical temperature than 58 K.

Nickel is nevertheless often used in the cable industry. There, one generally uses a buffer layer (CeO_2, Y-ZrO_2, MgO, ... [144, 145]) between the metallic substrate and the HTS layer to prevent nickel from diffusing into the superconductor during the heat treatment. In the next section, we present the characterizations of EPD coatings on silver.

5.4 EPD coatings on silver

Silver loses its mechanical stability around 930° C. Hence, a Y-123 coating on silver cannot be heated to $T_{\mathrm{P}} = 1015°$ C. A heat treatment under flowing argon was tested to decrease T_{P}. In contrast to coatings on nickel, such a heat treatment leads to dense layers without large cracks, and which adhere to the silver substrate.

Three samples, called sample 4, 5, and 6, were prepared in exactly the same conditions. Y-123 coatings were formed on silver substrates, 0.5 mm thick, with the EPD technique. After the deposition step, the samples were heated to 920° C under argon. Finally, an oxygen annealing at 500° C was applied for 30 h. More details on the samples preparation can be found in [70]. The three samples differ by their size. Samples 4 and 5 are square coatings of 1 cm × 1 cm, and serve for chemical and electrical characterizations. Sample 6 is a square coating of 4 cm × 4 cm and is used for shielding characterizations.

First, we present a chemical characterization of sample 4.

5.4.1 Chemical characterization

Figure 5.9 shows a scanning electron microscopy (SEM) visualization of the cross-section of sample 4: we deduce that the coating thickness is $\sim 45\ \mu$m. From an energy dispersive X-ray (EDX) analysis, the main phase in the coating was found to be the Y-123 phase [70] (the $BaCuO_2$ and the Y-211 phases are present, but in low

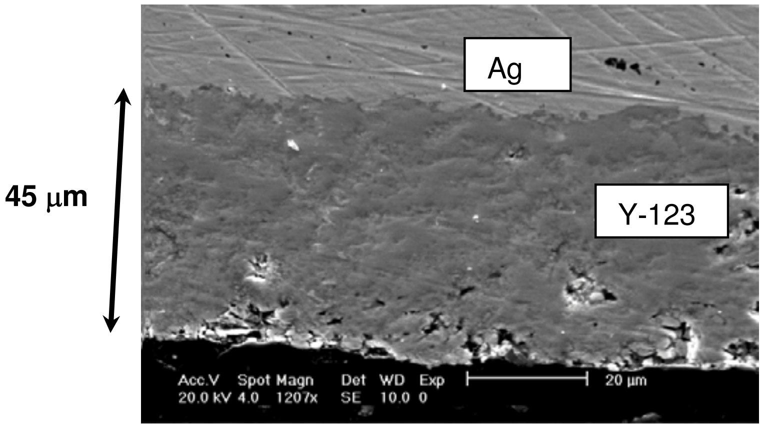

Figure 5.9: SEM photograph of the cross-section of sample 4; magnification 1207 x. The main phase present in the coating is the Y-123 phase. The stoichiometry of the different regions was determined by EDX analysis (ESEM XL-30 FEG Philips). Except near the surface, we observe that the density of the coating is high, and that it is homogeneous.

concentrations). From figure 5.9, we observe that the coating is quite homogeneous, and that much higher densities could not be achieved as we do not observe a large porosity. Hence, the heat treatment at 920° C under argon seems to have induced a partial melting of the coating which leads to its densification. In the next section, we check the existence of a macroscopic superconducting path in such a sample.

5.4.2 Resistive transition

Here, we focus on the resistive transition, and study its dependence on an applied magnetic field. For that purpose, we use sample 5 and the experimental technique described in section 5.1.1, with a DC magnetic field applied perpendicular to the sample plane. Figure 5.10 shows the measured $R(T)$ curves around T_c, for different values of the applied magnetic induction.

With no applied field, the onset takes place near 90 K. Then, the resistance decreases until the temperature reaches $T = T_\mathrm{c} \cong 87$ K, below which R is no longer measurable. In contrast to coatings on nickel, we have a sample with a critical temperature above 77 K with no applied field. Therefore, we will focus on EPD coatings on silver in the rest of the thesis. Above $T = 90$ K, we observe a metallic like behaviour, i.e. the measured resistance increases with temperature. Besides, this resistance is comparable to that of a silver plate of the same dimensions as the substrate. This suggests that the superconductor is shunted by silver above T_c.

As an increasing magnetic field is applied, we observe in figure 5.10 that the transition widens, and that the temperature of zero resistance, T_c, decreases. This comes from the fact that the grain boundaries are very sensitive to small magnetic inductions [20, 146], or said in other words, that the intergranular critical current density is very sensitive to the local magnetic induction. The resistance vanishes above 77 K, up to an applied magnetic induction of 20 mT. We can thus use the EPD coatings on silver up to 20 mT at 77 K. For higher magnetic inductions, the macroscopic superconducting properties of the EPD coatings are strongly altered.

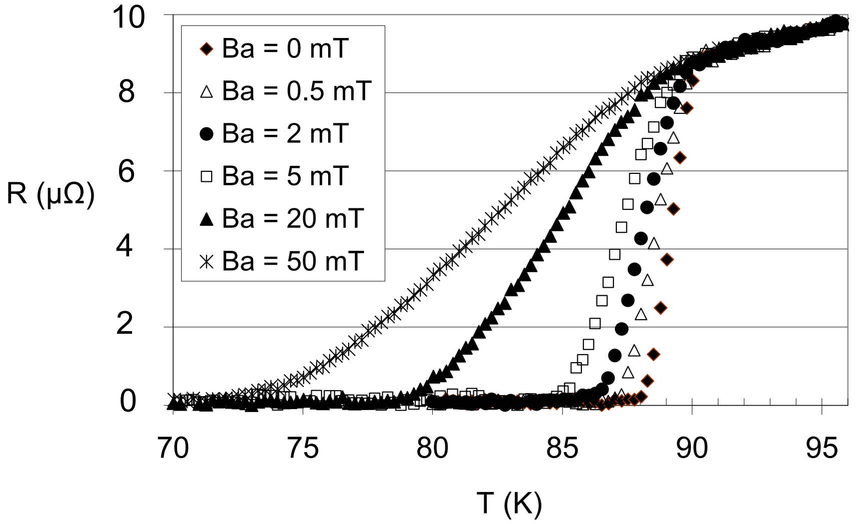

Figure 5.10: measured resistance of sample 5 versus temperature for various magnetic inductions applied perpendicular to the sample plane. The transition widens as the applied induction increases, but the temperature of zero resistance is higher than 77 K up to $B_\mathrm{a} = 20$ mT.

5.4.3 Critical current density

Knowing the intergranular critical current density, J_c, one can use the Bean model to estimate the maximum magnetic induction that can be efficiently shielded with the EPD coatings. In this section, we determine J_c for the coating of sample 5. This is carried out from the measured $I - V$ curves. Using the four-probe technique, an increasing current is injected through the coating, and the corresponding voltage is measured using the two inner contacts of figure 5.2. The critical current is reached when the electric field is equal to 1 μV/cm. For the measurement with sample 5, the distance between the voltage contacts is 4 mm, thus giving a critical voltage of 0.4 μV.

Figure 5.11 shows the measured $I - V$ curves at 77 K, for different magnetic inductions applied perpendicular to the coating surface. The curve $I_\mathrm{c}(B)$ can be deduced by determining the intersections between the $I - V$ curves and the line of constant critical voltage (dashed line), assuming $B = B_\mathrm{a}$, which means that the self field effects are neglected. Dividing the I_c values by the cross-section of the coating, one can obtain the critical current densities $J_\mathrm{c}(B)$.

Figure 5.12 shows the evolution of J_c with the magnetic induction. As expected, J_c strongly decreases as B increases. A fit based on the Kim law, $J_\mathrm{c} =$

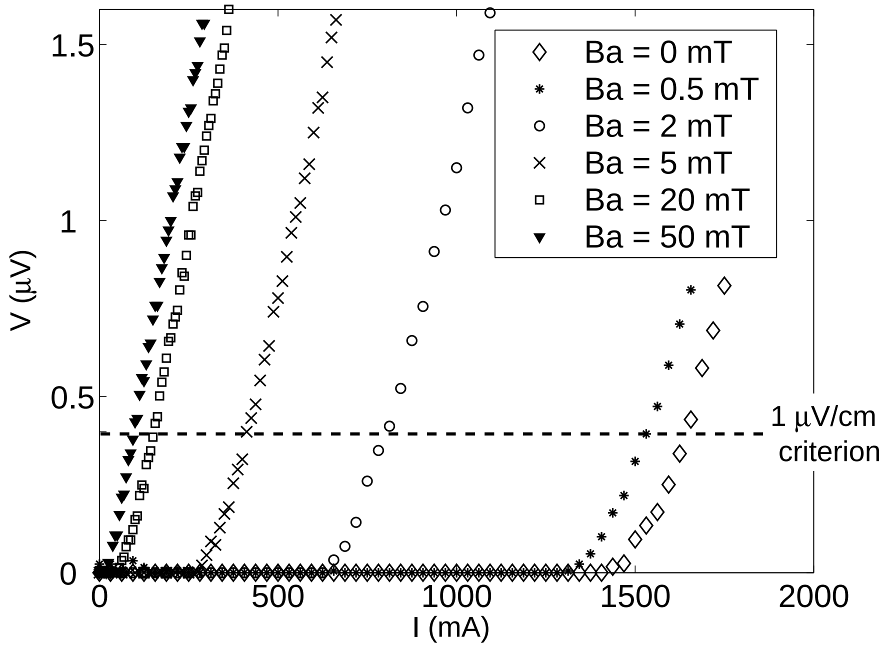

Figure 5.11: measured $I - V$ curves of sample 5 (EPD Y-123 coating on silver) for different applied magnetic inductions. The temperature is 77 K.

$J_{c0}\,(1 + B/B_1)^{-1}$, is also shown (solid line). From this fit, we deduce:

$$J_{c0} \cong 700\ \mathrm{A/cm^2}, \tag{5.2}$$

$$B_1 \cong 1.9\ \mathrm{mT}. \tag{5.3}$$

Other measurements of J_c were carried out with other EPD coatings on silver. All these measurements give J_c values ranging between 300 and 1100 A/cm^2 at 77 K in self field. No special dependence of J_c upon the thickness of the coating has been found. Such values can seem low, as compared to values of bulk single domains (J_c up to 10^5 A/cm^2) or thin films (J_c up to 10^6 A/cm^2). But the coatings that we consider here are made of a large number of small grains, randomly oriented, and connected by weak links. For Y-123 EPD coatings on silver, at 77 K and in self field, Bhattacharya et al. [100] report values around 500 A/cm^2 with a thickness of 65 μm, whereas Ondono-Castillo et al. [105] give J_c values up to 1500 A/cm^2 for coatings having a thickness of 20 μm. Hence, our coatings show similar performances. For bulk non-textured polycrystalline HTS, $J_c \cong 500$ A/cm^2 is reported at 77 K in self field [20].

Taking the value $J_c = 500$ A/cm^2, and a film thickness equal to $d = 50\ \mu$m, one can estimate the threshold induction given by the Bean model, $B_{\mathrm{lim,Bean}}$. Taking $B_{\mathrm{lim,Bean}} = \mu_0\ H_{\mathrm{P}}$, where the full penetration field H_{P} is given by $H_{\mathrm{P}} = J_c\, d$, we thus obtain $B_{\mathrm{lim,Bean}} \cong 0.3$ mT. For geometries with strong demagnetizing effects, the threshold induction is expected to be smaller than $B_{\mathrm{lim,Bean}}$. It follows that the magnetic inductions which can be efficiently shielded with the EPD coatings are small (less than 1 mT).

In the flux creep regime, HTS are characterized by a power law between current and voltage. As we do not work close to the critical temperature $T_c \cong 90$ K, we can

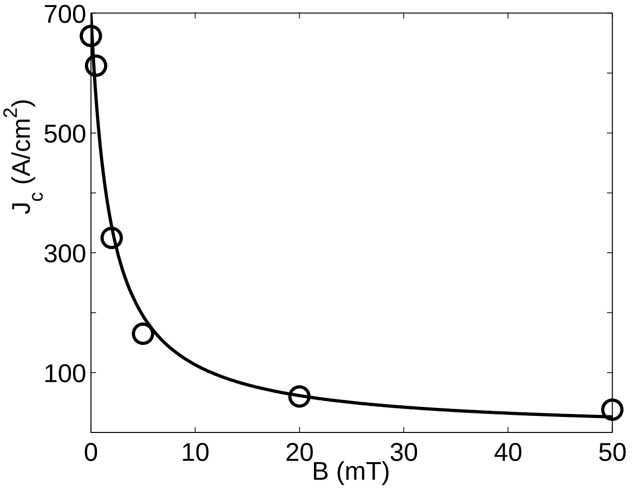

Figure 5.12: evolution of the critical current density, J_c, with the magnetic induction B at 77 K. The J_c values were deduced from the $I-V$ curves of figure 5.11, applying the 1 μV/cm criterion. The solid line is a fit using the Kim law. The fit parameters are given in (5.2) and (5.3).

assume that the coating is in the flux creep regime. But in figure 5.11, the relation between the current and the voltage is closer to a linear dependence than a power law at $I > I_c$. This suggests that for $I > I_c$, the measured resistance is that of silver, as the metallic substrate then presents a lower resistive path than the HTS coating does.

5.4.4 Shielding effect

In the two previous sections, we have shown that above the boiling point of liquid nitrogen, a macroscopic superconducting current can flow through the EPD Y-123 coatings on silver. But one may wonder how such samples can attenuate a low frequency magnetic field. In this section, we evaluate the shielding properties of a planar EPD coating, using the measurement setup described in section 5.1.3. For that purpose, we use sample 6, whose size is 4 cm × 4 cm. As a reminder, $T_\mathrm{c} \cong 87$ K in self field for samples prepared in the same conditions.

An AC magnetic field is applied by the source coil of figure 5.3, and the magnetic induction behind the sample is measured by the sensing coil. The distance between both coils is 5 mm and the sample is placed in between. The frequency of the applied field is 103 Hz and the measurement is carried out in liquid nitrogen. In such conditions the skin depth of silver, $\delta(77K) \cong 2.7$ mm, is larger than the thickness of the substrate (0.5 mm).

Figure 5.13 shows the ratio $B_\mathrm{abs}/B_\mathrm{pres}$ as a function of the RMS value of the applied magnetic induction. The magnetic induction along the abscissa of the graph of figure 5.13 is the applied induction at the centre of the planar sample, where the induction is actually perpendicular to the sample plane.

Below $B_\mathrm{a,RMS} = 0.07$ mT and for decreasing applied inductions, the ratio $B_\mathrm{abs}/B_\mathrm{pres}$ increases rapidly and reaches values around $230 \cong 47$ dB at $B_\mathrm{a,RMS} \cong$

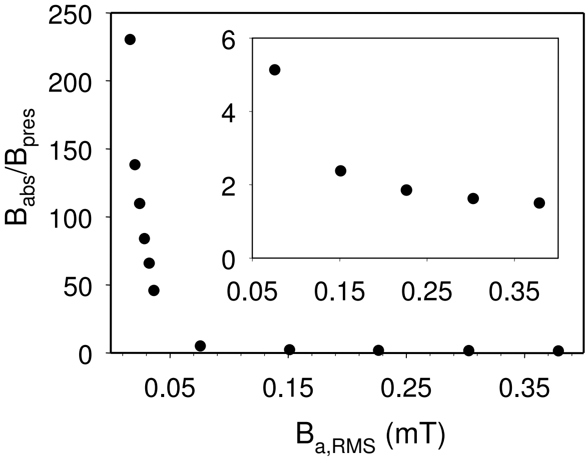

Figure 5.13: ratio $B_{\text{abs}}/B_{\text{pres}}$ measured with sample 6 as a function of the RMS value of the applied magnetic induction. The frequency is 103 Hz and the temperature is 77 K.

0.015 mT. For lower applied inductions, it is actually no longer possible to measure the magnetic induction in the presence of the sample with our setup. Hence, contrary to sample 2 (EPD coating with non-connected grains), we see that an EPD coating on silver with connected grains strongly attenuates a low frequency magnetic field at 77 K. For magnetic inductions larger than 0.07 mT, the ratio $B_{\text{abs}}/B_{\text{pres}}$ is close to unity, meaning that the sample ceases to shield.

At the end of the previous section, we have estimated the threshold induction given by the Bean model. We have found $B_{\text{lim,Bean}} \cong 0.3$ mT. In this model, there are no demagnetizing effects, and $B = 0$ below $B_{\text{a}} = B_{\text{lim,Bean}}$. Here, we do not have such a situation.

From figure 5.13, we see that at $B_{\text{a,RMS}} = B_{\text{lim,Bean}}/\sqrt{2} = 0.3\ \text{mT}/\sqrt{2} \cong 0.21$ mT, the ratio $B_{\text{abs}}/B_{\text{pres}}$ is close to two, and that it does not vary strongly with the applied field. But the geometry of the shielding measurement of figure 5.13 leads to important demagnetizing effects which can strongly increase the local applied field.

Assuming that sample 6 is an ellipsoid of revolution having an axis parallel to the applied field equal to 50 μm and an equatorial axis equal to 4 cm, we find that the demagnetizing factor is equal to $N \cong 0.998$ [19]. Taking $\chi = -1$, one can have a first estimation of the total field experienced by sample 6 (see chapter 1), $H_{\text{T}} = H_{\text{a}}/\left(1 + N\chi\right) \cong 500\, H_{\text{a}}$, which is much larger than H_{a}. Such an evaluation certainly overestimates H_{T} as $\chi \neq -1$ even if it is close to that value at low applied field. But this calculation could explain that the ratio $B_{\text{abs}}/B_{\text{pres}}$ is so small at $B_{\text{a,RMS}} = B_{\text{lim,Bean}}/\sqrt{2} \cong 0.21$ mT.

For reference, we characterized the shielding properties of a ferromagnetic planar sample of dimensions identical to those of sample 6. This plate, called sample 7 and 0.8 mm thick, is made of a mu-metal material coming from the firm MECA MAGNETIC [15]. According to the manufacturer, the ferromagnetic material has an initial relative permeability of $\sim$ 50 000 in DC conditions, and $\text{d}B/\text{d}H \cong \mu_0$ for $B > 0.75$ T. We applied a magnetic field of 103 Hz at one side of the plate, and measured the induction behind the screen. Here, the measurement was carried out at 300 K.

For 0.01 mT $< B_{\mathrm{a,RMS}} <$ 0.4 mT, we measured a nearly constant shielding factor: $B_{\mathrm{abs}}/B_{\mathrm{pres}} \cong 35$ (31 dB). Such a value is smaller than the 47 dB measured with the EPD coating at $B_{\mathrm{a,RMS}} \cong 0.015$ mT. Note that the thickness of the HTS layer is about 16 times smaller than the thickness of the mu-metal plate. Taking into account the substrate, the total thickness of the EPD sample is ~ 0.55 mm which is smaller than that of the ferromagnetic plate (0.8 mm). Hence, a planar superconducting coating seems to attenuate low magnetic fields of low frequency much more efficiently than a ferromagnetic plate does.

5.5 Summary

In this chapter, we have experimentally studied the superconducting and the shielding properties of Y-123 coatings deposited on silver and nickel substrates by the electrophoretic deposition (EPD) technique. This study has been carried out by using commercial, and home-made measurement systems.

The best coatings on nickel present a macroscopic superconducting path only below 58 K. This is due to the diffusion of nickel atoms into the Y-123 layer during the thermal treatment. Silver atoms also diffuse into the HTS layer during the thermal treatment, but they do not alter the superconducting properties of the Y-123 phase. For coatings on silver, the transition temperature lies around 90 K in self field. As the aim of our research project is to have a HTS shield working at 77 K, we focused mainly on coatings on silver.

Y-123 coatings on silver have a critical current density which lies between 300 and 1100 A/cm^2 in self field. Such values are of the same order of magnitude as the ones reported in the literature for similar samples. Using the Bean model, we deduce the threshold induction $B_{\mathrm{lim,Bean}} = 0.3$ mT if the coating thickness is ~ 50 μm. Hence, the maximum magnetic induction which could be shielded with an EPD shield is below 1 mT. When applying a magnetic induction, J_{c} strongly decreases, as it is expected for such a polycrystalline material. The decrease of J_{c} with B can be fitted with a Kim law.

By using a home-made system, we measured how a planar EPD coating attenuates a magnetic field of low frequency at 77 K. The sample is placed between two small coils. The source coil applies an AC magnetic field, and the sensing coil measures the field behind the screen. By comparing the signal at the sensing coil in the absence and in the presence of the sample, we can deduce the field attenuation realized by the plate. We have found that the attenuation is around 230 (~ 47 dB) if the RMS value of the applied induction is ~ 0.015 mT. Such a field attenuation is larger than the one realized by a mu-shield plate for which we measured a field attenuation around 35 for applied magnetic inductions of same magnitude and same frequency. Note that the thickness of the EPD coating lies around 50 μm, whereas the thickness of the ferromagnetic plate is 800 μm. Taking into account the silver substrate, the total thickness of the EPD sample is ~ 550 μm. Hence, HTS shields present higher field attenuations than ferromagnetic screens do. When the magnitude of the applied induction increases, the field attenuation realized by the EPD coating strongly decreases and there is nearly no field attenuation for $B_{\mathrm{a,RMS}} > 0.7$ mT.

The field geometry of this shielding characterization is generally not encountered in practice. To obtain high field attenuations, it seems important to have closed, or nearly closed geometries. Then, one can expect to have shielding factors much higher than ~ 200. The planar geometry of the shielding measurement leads also to some difficulties if one wants to compare the experimental results with theory. The applied field is strongly non uniform and the direction of the shielding currents is not known if we do not neglect the finite thickness of the coating. As HTS shields are generally not ellipsoids and do not present a uniform magnetization, the approach of the demagnetizing factor can only be used as a first approximation to evaluate the geometric effects.

For these reasons, we consider axisymmetric geometries in uniform axial fields in the two next chapters. For such geometries, numerical methods exist to study the field penetration into HTS, see chapter 4.

Chapter 6

Magnetic shielding properties of tubular HTS samples

The maximum attenuation that can be obtained for a magnetic shield of fixed surface is expected to be obtained with closed or nearly closed geometries. Hence, the tubular geometry is more relevant than the planar one studied in the previous chapter. A tube of finite size in the parallel geometry, in which the source field is applied parallel to the tube axis, is also amenable to direct physical interpretation and numerical simulations, as currents flow along concentric circles perpendicular to the axis, see chapter 4. These elements can explain why the tube geometry has been chosen by many authors for investigating the possibility to use HTS to make efficient magnetic shields [18, 26, 27, 28, 30, 31, 33, 70, 75, 78, 81, 147, 148, 149, 150, 151, 152]. Note that in the parallel geometry, a HTS tube certainly outclasses a ferromagnetic shield (see chapter 1).

In this chapter, we study both experimentally and theoretically the shielding properties of HTS tubular samples when a magnetic field is applied either parallel (parallel geometry) or perpendicular (transverse geometry) to the tube axis. In the parallel geometry, several properties, which are important for a shielding application, can be determined, such as the maximum magnetic induction that can be strongly attenuated, the spatial variation of the shielding factor, and the frequency response of a HTS shield.

The experimental part is carried out with a commercial sample, and with a home-made EPD sample. This allows one to compare the shielding properties of two HTS samples prepared in different conditions. The theoretical part is carried out with the approach of Campbell and Evetts (see section 4.1), and with the method of Brandt (see sections 4.5.1 and 4.5.2). The first method allows one to study the field penetration into infinite pierced samples in the parallel geometry. The method of Brandt is used to study the field penetration into HTS tubes of finite size in the parallel geometry, and into infinitely long tubular samples in the transverse case.

The chapter is organized as follows. First, we consider samples in the parallel geometry. In section 6.1, we model the field penetration into infinitely long hollow samples using the method of Campbell and Evetts. Then, we explain the characterization techniques used in this chapter. In section 6.3, we present a detailed study of the magnetic shielding properties of HTS tubes in the parallel geometry. Afterwards, we compare these results with those obtained with an EPD and a mu-metal tube. Finally, we study the field penetration into tubular HTS samples in the transverse geometry.

6.1 Infinitely long hollow samples in the parallel geometry

Different techniques exist to make a HTS tubular sample. A hole in a bulk superconducting material can be drilled [75, 153, 154, 155], a precursor powder can be pressed to form a tube [26, 28, 30, 31, 32, 152, 153, 156], or a coating can be deposited on a cylindrical substrate [33, 70, 78, 79, 157, 81, 83]. Depending on the used technique, the shield has different properties.

In chapter 2, according to the Bean model, we have seen that the maximum magnetic induction that can be efficiently shielded by a HTS tube is given by

$$B_{\mathrm{lim,Bean}} = \mu_0 H_{\mathrm{P}} = \mu_0 J_{\mathrm{c}} d, \tag{6.1}$$

where H_{P} is the full penetration field, J_{c} is the critical current density, and d is the thickness of the superconducting wall. This result was obtained with an infinitely long HTS with a centred hole of the same shape as the outer cross-section of the sample.

When a hole is drilled in a bulk HTS or when a powder is pressed in a tubular form, the thickness of the superconducting wall is typically larger than 1 mm. By comparison, the thickness of a HTS coating deposited on a metallic substrate is generally less than 100 μm. Taking typical values for drilled HTS or samples made from pressed powder, $J_{\mathrm{c}} = 500$ A/cm^2 and $d = 2$ mm, we deduce, from (6.1), that $B_{\mathrm{lim,Bean}} \cong 12$ mT. However, because HTS are brittle ceramics, large shields (of a few cubic decimetres) cannot be made with such methods. Instead, it is possible to make them with a HTS film deposited on a metallic substrate. Then, the maximum induction that can be efficiently shielded is estimated at $B_{\mathrm{lim,Bean}} \cong 0.3$ mT, if we take typical parameters of EPD coatings, $J_{\mathrm{c}} = 500$ A/cm^2 and $d = 50$ μm.

Hence, for some small scale applications, it could be useful to use a drilled bulk HTS or a hollow sample made from pressed powder to obtain a high $B_{\mathrm{lim,Bean}}$ value. Then, one can wonder what is the best hole shape, and what is its best location. In this section, we try to answer these questions by using the approach of Campbell and Evetts which was explained in section 4.1. In particular, we study how the relation (6.1) determining $B_{\mathrm{lim,Bean}}$ is affected when the hole has not the same shape as the sample outer cross-section and when it is not centred. As in the Bean model, $B_{\mathrm{lim,Bean}}$ is the applied magnetic induction for which the flux front reaches the cavity.

As a reminder, the approach of Campbell and Evetts assumes that an infinitely long sample is subjected to a uniform parallel magnetic field and that any flowing current has a density equal to J_{c}, independent of the magnetic induction. For our study, we suppose that the external HTS cross-section is a square of dimension $a \times a$ (see figure 6.1) and that the sample is characterized by the critical current density J_{c}.

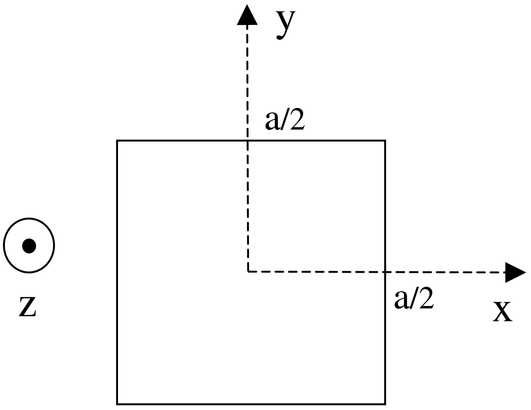

Figure 6.1: geometry studied in this section. An infinitely long sample along $\hat{z}$, with a square external cross-section $a \times a$, is subjected to the uniform magnetic induction $\mathbf{B}_\mathrm{a} = B_\mathrm{a}\hat{z}$.

We impose that the hole has a fixed surface, $S_\mathrm{sh} = \pi\,(0.2\,a)^2$. We want to determine which shape and position of the cavity lead to the highest $B_\mathrm{lim,Bean}$. First, consider a circular hole, centred at $(x_0, y_0) = -(0.2, 0.1)\,a$, and of radius $R = 0.2\,a$. Following the method of Campbell and Evetts and assuming that the sample has been cooled in zero-field conditions, figure 6.2 shows the flux front for equally separated increasing applied magnetic inductions. If e represents the smallest distance between the sample outer cross-section and the hole, then

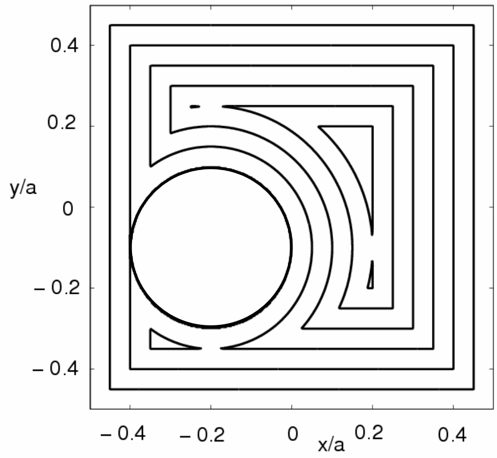

Figure 6.2: flux front for $B_\mathrm{a} = 0.05$, 0.1, 0.15, 0.2, 0.25, and $0.3\,\mu_0 J_\mathrm{c} a$, when the hole is circular, of radius $R = 0.2\,a$, and centred at $(x_0, y_0) = -(0.2, 0.1)\,a$.

$$B_\mathrm{lim,Bean} = \mu_0 J_\mathrm{c} e = 0.1\,\mu_0 J_\mathrm{c}\,a < \mu_0 H_\mathrm{P}. \tag{6.2}$$

To increase the threshold induction, $B_\mathrm{lim,Bean}$, it is necessary to maximize e.

Hence, keeping a circular hole, the cavity position which gives the highest $B_\mathrm{lim,Bean}$ is $(x_0, y_0) = (0, 0)$, which means that the hole and cross-section centres coincide. The flux front positions corresponding to this second case and for increasing applied inductions are depicted in figure 6.3. In this case, $B_{\mathrm{lim,Bean}} = \mu_0 J_{\mathrm{c}} 0.3\,a$, where $e = 0.3\,a$ is the smallest distance between the hole and the outer sample cross-section. But we have $B_{\mathrm{lim,Bean}} < \mu_0 H_{\mathrm{P}}$ again.

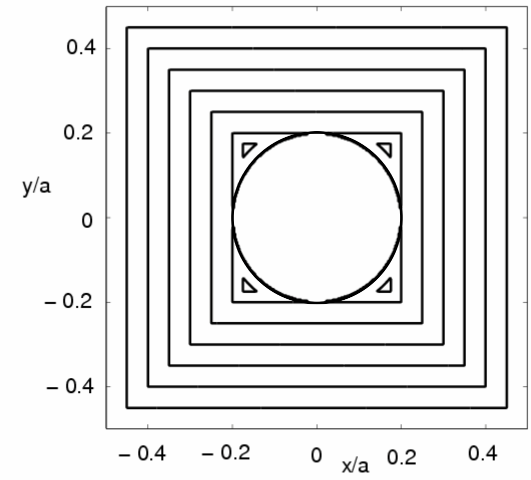

Figure 6.3: flux front for $B_{\mathrm{a}} = 0.05$, 0.1, 0.15, 0.2, 0.25, 0.3, and $0.325\,\mu_0 J_c a$ when the hole is circular, of radius $R = 0.2\,a$, and centred at $(x_0, y_0) = (0, 0)$.

Now, let us consider a square hole of side c, having the same surface as the circular cavity $S_{\mathrm{sh}} = \pi\,(0.2\,a)^2$, which means $c \cong 0.3545\,a$. We expect to obtain the highest $B_{\mathrm{lim,Bean}}$ when the hole is centred at $(x_0, y_0) = (0, 0)$. The flux front for increasing applied fields corresponding to this case is depicted in figure 6.4. The threshold induction corresponding to this geometry is $B_{\mathrm{lim,Bean}} = \mu_0 J_{\mathrm{c}}(0.5 - c/2)\,a \cong 0.3228\,\mu_0 J_{\mathrm{c}} a$. We have also $B_{\mathrm{lim,Bean}} = \mu_0 H_{\mathrm{P}}$. This is the largest threshold induction.

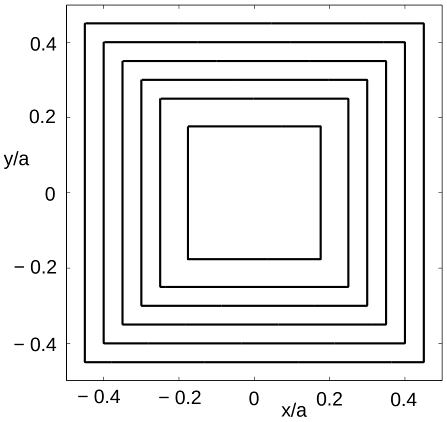

Figure 6.4: flux front for $B_{\mathrm{a}} = 0.05$, 0.1, 0.15, 0.2, 0.25, and $0.3228\,\mu_0 J_c a$, when the hole is a square, of side $c \cong 0.3545\,a$, and centred at $(x_0, y_0) = (0, 0)$.

One can obtain similar results using a circular or a rectangular outer sample cross-section. In each case, the solution which gives the highest threshold $B_{\mathrm{lim,Bean}}$ is to choose a hole having the same shape as the external cross-section, and whose centres coincide. In such a situation, $B_{\mathrm{lim,Bean}} = \mu_0 H_{\mathrm{P}}$.

The results that we have obtained in this section are strictly correct for infinitely long samples in the parallel geometry, with a constant critical current density, and without flux creep. Hence, the approach of Campbell and Evetts is not appropriate for studying real HTS. In section 6.3, we theoretically study the field penetration into samples of finite size with the method of Brandt when the applied field is axial. Using the same method, we consider in section 6.6 the transverse geometry. In each case, these numerical results are compared with measurements. In the next section, we describe the characterization techniques used for the experimental study.

6.2 Characterization techniques

The measurement systems described in this section allow one to characterize the shielding properties of tubular samples at 300 K and 77 K. The source field can be either DC or AC, and it can be directed parallel or perpendicular to the tube axis. We first present the experimental setup when the applied field is a DC field. Second, the apparatus working with an AC source field is described. Both are home-made measurement systems.

6.2.1 DC applied field

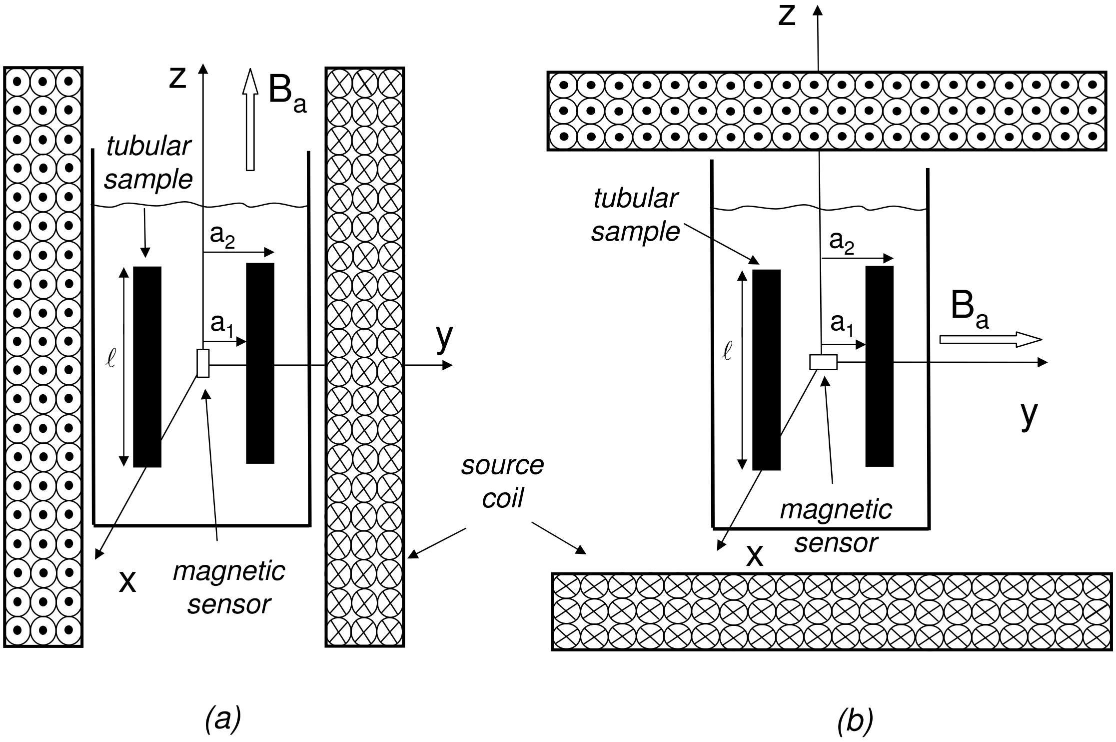

Figure 6.5: home-made experimental setup for characterizing the shielding properties of tubular samples if the source field is a DC field. The magnetic field is applied either parallel (figure (a)) or perpendicular (figure (b)) to the tube axis.

The system used for characterizing the shielding properties of tubular samples in the DC mode is sketched in figure 6.5. The sample is placed in a box which is itself inserted into a copper coil generating the source field. This box can be filled with liquid nitrogen. The inner diameter of the source coil is 20 cm and its length is 45 cm. Then, the variation of the applied field along the axis of a tubular sample, which is 10 cm long and is located at the centre of the source coil, is less than 1.5 % [158]. The source coil is connected to a DC power supply (SM 70-22 from Delta Electronika) and the applied induction can reach 30 mT. Depending upon the source coil position with respect to the box position, the applied field is axial or transverse. The induction in the inside of the tube, B_{in}, is measured with a high sensitivity Hall probe from Arepoc [159] (HHP-MP model). The size of the Hall probe is $7 \times 5 \times 1$ mm^3.

The magnetic sensor is connected to a HP34420 nanovoltmetre and is fixed at the centre of the tubular sample. To reduce noise from outside sources, the entire setup of figure 6.5 is enclosed in a double mu-metal ferromagnetic enclosure. Then, the magnetic resolution is around 1 μT. Figure 6.6 shows a photograph of the setup. More details concerning the realization of the experimental system can be found in [158].

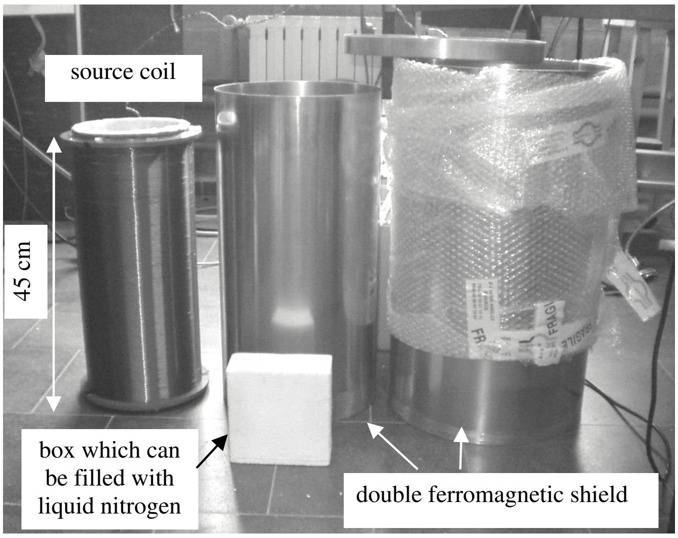

Figure 6.6: photograph of the measurement system designed to evaluate the shielding properties of tubular samples in the DC mode. The double ferromagnetic shield is used to reduce the environmental noise.

6.2.2 AC applied field

The measurement system used for characterizing the shielding properties of tubular samples in the AC mode is depicted in figure 6.7. The source coil, connected to an AC function synthetizer (HP8904A), delivers an AC magnetic induction, of frequency ranging between 43 Hz and 1003 Hz. Using an audio amplifier, the maximum applied induction at 103 Hz is 20 mT. The inner diameter of the source coil is 2.8 cm and its length is 21 cm. In contrast to the setup described in the DC mode, the applied induction can only be axial here.

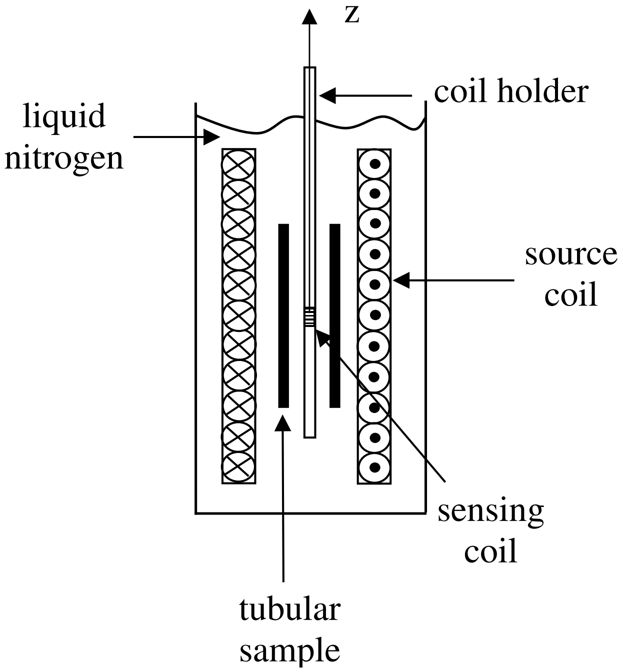

Figure 6.7: experimental setup for characterizing the shielding properties of tubular samples if the source field is an AC field. Here, the applied field can only be axial.

The magnetic induction inside the tube, B_{in}, is measured with a sensing coil having 800 turns and 5 mm long, mounted on a pyrex holder. The voltage across the sensing coil is measured by a lock-in amplifier (EGG7260). The source coil, the sample, and the sensing coil can be immersed in liquid nitrogen (77 K). The minimum measurable magnetic induction at 103 Hz is around 1 nT. As a result, care must be taken to reject the effect of common-mode voltages. In the present work, the capacitive coupling between the source and the pick-up coils was reduced by electrically connecting the tubular sample to earth so as to realize an electric shield. Contrary to the setup described in the DC mode, the magnetic sensor can move along the tube axis here. This allows one to study the spatial variation of the shielding properties along the tube axis. A photograph of the setup is shown in figure 6.8.

We now turn to studying the shielding properties of finite HTS tubes in the parallel geometry.

6.3 Magnetic shielding properties of finite HTS tubes in the parallel geometry

Several factors determine the quality of a HTS magnetic shield. The first factor is the threshold induction, B_{lim}, that characterizes the maximum applied induction that can be strongly attenuated. As real HTS magnetic shields are not infinitely long, do not have a constant critical current density, and are not characterized by a creep exponent $n \to \infty$, the real B_{lim} generally differs from the value given by the

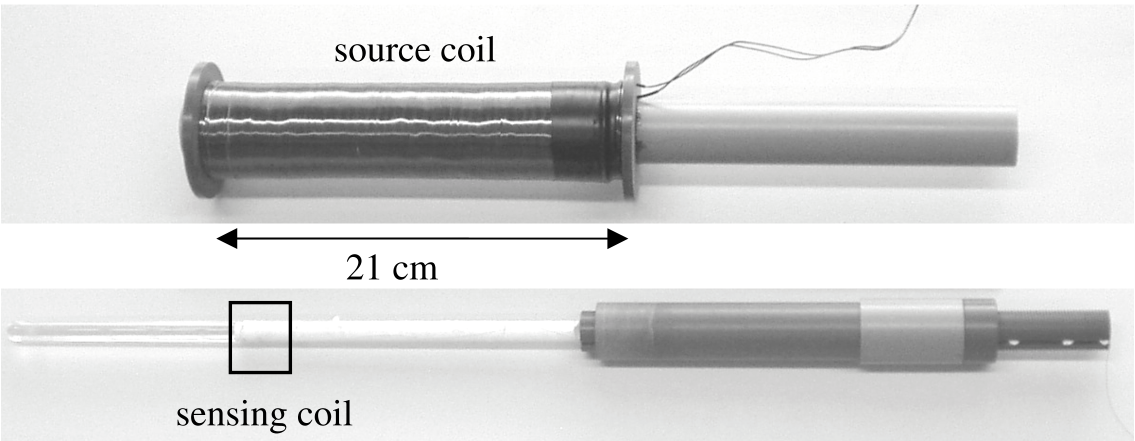

Figure 6.8: photograph of the experimental setup used for characterizing the shielding properties of tubular samples in the AC mode. The setup can be immersed in liquid nitrogen, and the sensing coil can move along the studied tube axis.

Bean model, $B_{\mathrm{lim,Bean}}$. A second important factor is the geometrical volume over which a shield of given size and shape can attenuate an external field below a given level. A third determining factor is the frequency response of the shield.

A number of results can be found in the literature on finite HTS tubes in the parallel geometry. For HTS polycrystalline materials at 77 K, B_{lim} was found to vary between 0.3 mT for a tube with a superconducting wall of thickness $d =$ 40 μm [18, 70], and 15 mT with $d = 2.2$ mm [148]. If lower temperatures than 77 K are allowed, higher B_{lim} values can be obtained. As an example, MgB_2 tubes were reported to shield magnetic inductions up to 1 T at 4.2 K [150, 160] ($d = 9$ mm). Results on the variation of the field attenuation along the tube axis appear to be contradictory. A decreasing exponential dependence towards the extremities was measured for a Y-123 tube [31] and for a BSCCO tube [78]. Other measurements in similar conditions have shown instead a constant shielding factor in a region around the centre of Y-123 and BSCCO tubes [147, 151]. As for the frequency response, the shielding factor is expected to be constant if flux creep effects are negligible, as is the case in the Bean model [48, 161]. It is, on the other hand, expected to increase with frequency in the presence of flux creep, since the induced currents saturate to values that increase with frequency [120]. Experimental data have shown very diverse behaviours. In [78], the field attenuation due to a thick BSCCO film on a cylindrical silver substrate was found to be frequency independent. The same results were established for superconducting disks made from Y-123 powder and subjected to perpendicular fields [162, 163]. Yet other studies on bulk BSCCO tubes [28, 30] measured a field attenuation that decreases with frequency, whereas the attenuation was shown to slowly increase with frequency for a Y-123 superconducting tube [152].

The purpose of this section is to provide a detailed study of the magnetic shielding properties of a finite polycrystalline HTS tube in the parallel geometry, with regard to the three determining factors: threshold induction, spatial variation of the field attenuation and frequency response[1]. The study is carried both experimentally and

---

[1] The material of this section has been reported in [149]

by means of numerical simulations, in order to shed light on the relation between the microscopic mechanisms of flux penetration and the macroscopic properties. For the experimental part, we use a commercial HTS tube. For the numerical simulations, we follow the method proposed by Brandt in [120] which was explained in section 4.5.1. As a reminder, the geometry that we consider here is shown in figure 6.9. We focus on a HTS tube with one opening at each end and assume that the superconducting properties are uniform along the axis and isotropic.

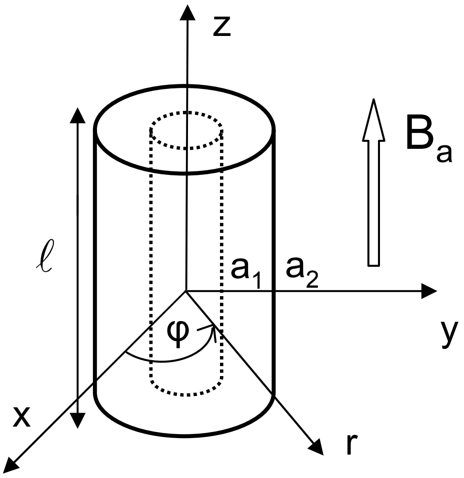

Figure 6.9: geometry studied in this section. A tube of internal radius a_1, external radius a_2, and length ℓ, is subjected to a uniform axial magnetic induction $\mathbf{B_a} = B_\mathrm{a}\,\hat{z}$. The centre of the tube lies at $(r, z) = (0, 0)$.

The section is organized as follows. The sample is described in section 6.3.1; the used constitutive laws and the numerical algorithm are given in section 6.3.2. Section 6.3.3 is devoted to the shielding properties of superconducting tubes subjected to slowly time varying applied fields (called the DC mode). First, the evolution of the measured internal magnetic induction of the commercial sample versus the applied induction is presented. We then detail the field penetration into a HTS tube and study the field attenuation as a function of position along the tube axis. The frequency response of the shield is addressed in section 6.3.4, where it is shown that the frequency dependence of the shielding factor can be explained by scaling laws provided heat dissipation caused by the AC magnetic field can be neglected.

6.3.1 Sample

We measured the shielding properties of a commercial superconducting specimen (type CST-12/80 from CAN Superconductors), which was cooled at $T = 77$ K under zero field. The sample is a tube made by isostatic pressing of a polygrain ceramic. Its main characteristics are summarized in table 6.1.

Material	$Bi_{1.8}Pb_{0.26}Sr_2Ca_2Cu_3O_{10+x}$
Length	$\ell = 8$ cm
Inner radius	$a_1 = 6.5$ mm
Outer radius	$a_2 = 8$ mm
Wall thickness	$d = a_2 - a_1 = 1.5$ mm
Critical temperature	$T_\mathrm{c} \cong 108$ K

Table 6.1: physical characteristics of the commercial HTS tube: the material composition and the critical temperature come from [164].

6.3.2 Theory

Flux penetration in polycrystalline bulk ceramics

Bulk polycrystalline BiSrCaCuO ceramics consist of a stack of a large number of superconducting grains, see chapter 3. The penetration of a magnetic flux in such a material is inhomogeneous and strongly depends on the microstructure, as shielding currents can flow both in the grains and the intergranular matrix. For a polygrain material that has been cooled in zero-field conditions, the flux penetrates in roughly three different steps [165]. First, for the weakest applied fields, Meissner surface currents shield the volume and no flux enters the sample. When the local induction, B, exceeds $\mu_0 H_{\mathrm{c}1i}$, where $H_{\mathrm{c}1i}$ is the lower critical field of the intergranular matrix, vortices start entering this region. The magnetic flux penetrates the grains at the higher induction $B \cong \mu_0 H_{\mathrm{c}1g}$ [166], where $H_{\mathrm{c}1g}$ is the lower critical field of the grains themselves.

Model assumptions

In our model, we neglect surface barrier effects and set $H_{\mathrm{c}1i}$ to zero. Therefore, flux starts threading the intergranular matrix as soon as the applied field is turned on. The penetration of individual grains depends on the intensity of the local magnetic field which, because of demagnetization effects, varies as a function of the grain sizes and orientations. The penetration of each grain may thus take place over a range of applied fields: we expect an increasing number of grains to be penetrated as the external field is increased. Since we aim at studying the macroscopic properties of the superconducting tube and aim at deriving recommendations of practical interest, we will not seek to describe grains individually and thus neglect detailed effects of their diamagnetism. We will instead consider the induction B to be an average of the magnetic flux over many grains and assume the constitutive law

$$\mathbf{B} = \mu_0 \mathbf{H}. \tag{6.3}$$

The resulting model describes the magnetic properties of an isotropic material which supports macroscopic shielding currents.

We will further assume the material to obey the constitutive law introduced in chapter 4:

$$\mathbf{E} = E_\mathrm{c} \left(\frac{J}{J_\mathrm{c}} \right)^n \frac{\mathbf{J}}{J}, \tag{6.4}$$

where J is the magnitude of the vector current density $\mathbf{J}$. The value for n that is adequate for the sample of table 6.1 is to be determined from the frequency dependence of its shielding properties, see section 6.3.4.

Finally, we will either assume that the critical current density, J_c, is field independent, or that it decreases with the local magnetic induction as in the Kim model:

$$J_\mathrm{c}(B) = \frac{J_{\mathrm{c}\,0}}{1 + B/B_1}. \tag{6.5}$$

Due to the polygranular nature of the commercial sample, we expect J_c to be sensitive to small magnetic inductions. The parameters $J_{\mathrm{c}\,0}$ and B_1 entering (6.5) are experimentally determined by fitting magnetization data, as discussed in section 6.3.3.

Numerical algorithm

To study the field penetration into HTS tubes of finite length, we use the method of Brandt which was explained in section 4.5.1. This method is based on the resolution of an equation of motion for the macroscopic current density flowing only in the superconducting tube. Once the current density distribution is known, the magnetic field in the entire space is obtained by integrating the Biot-Savart law. Because of the symmetry, we work in cylindrical coordinates, and since the current density and magnetic field are invariant under a rotation around the z-axis of figure 6.9, positions are denoted by $\mathbf{r} = (r, z)$ (no φ variation).

We present the results in the DC mode in the next section.

6.3.3 Results in the DC mode

Experimental results

To evaluate the shielding properties of the commercial sample in the DC mode, we used the experimental setup described in section 6.2.1. The sample is placed inside the source coil generating an axial magnetic induction $\mathbf{B}_\mathrm{a} = B_\mathrm{a}\,\hat{z}$. Here, in the DC mode, B_a increases at a constant rate $\dot{B}_\mathrm{a} = 0.2$ mT/s with a brief stop (around 1 s) needed to measure the internal induction at each wanted value of B_a. The induction in the inside of the shield, B_in, is measured with a Hall probe placed at the centre of the tube.

Figure 6.10 (open circles) shows the evolution of the magnetic induction measured at the centre of the tube, $B_\mathrm{in}(0,0) = \sqrt{B_r^2(0,0) + B_z^2(0,0)}$, as a function of the applied magnetic induction. The sample of table 6.1 was cooled down to 77 K in zero-field conditions. Then, we applied an increasing magnetic induction and reached $B_\mathrm{a} = 28$ mT. Upon decreasing the applied induction to $B_\mathrm{a} = -28$ mT and increasing it again up to $B_\mathrm{a} = 28$ mT, the internal induction is seen to follow an hysteretic curve. This behaviour reflects the dissipation that occurs as vortices sweep in and out of the superconductor. Remarkably, along the first magnetization curve, B_in is negligible below a threshold $B_\mathrm{lim} \cong 14$ mT and increases rapidly for higher B_a. As the tube is no longer an efficient magnetic shield in this latter regime, several authors regarded B_lim as a parameter determining the quality of the shield [81, 147, 148].

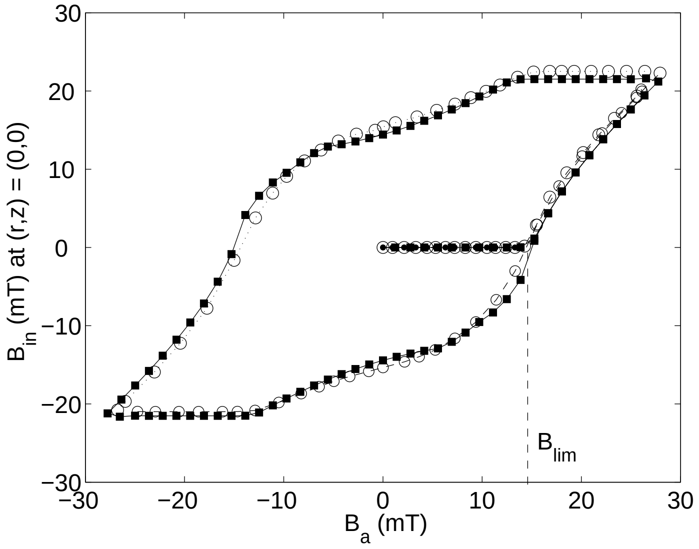

Figure 6.10: evolution of the internal magnetic induction at the centre of the commercial tube, $B_{\rm in}(0,0)$, as a function of the applied induction. The sample (table 6.1) is cooled in zero-field conditions down to $T = 77$ K. The open circles represent the experimental data and the filled squares represent the modelling.

In contrast to the Bean model, the internal field is never zero for real HTS tubes. Hence, we are led to determine $B_{\rm lim}$ using a criterion. In the DC mode, defining the shielding factor by

$$DCSF(r,z) = \frac{B_{\rm a}}{B_{\rm in}(r,z)}, \tag{6.6}$$

where $B_{\rm in}(r,z)$ is the magnitude of the magnetic induction at the position (r,z) in the hollow of the tube, we adopted the convention that $B_{\rm lim}$ corresponds to the maximum applied induction for which the DC shielding factor at the centre of the tube, $DCSF(0,0)$, is higher than 1000 (60 dB):

$$DCSF(0,0) > 1000 \quad \texttt{for} \quad B_{\rm a} < B_{\rm lim}. \tag{6.7}$$

With such a definition, the experimental threshold is $B_{\rm lim} \cong 14$ mT for the commercial tube.

Model parameter and numerical results

The shape of the curve of figure 6.10 is indicative of the dependence of the critical current density, $J_{\rm c}$, on the local induction. Assuming the Kim model (6.5), the parameters $J_{\rm c0}$ and B_1 can be extracted from data as follows. First, we neglect flux creep effects and assume that the current density can either be null or equal to $J = J_{\rm c}(B)$. Second, we neglect demagnetization effects and thus assume that the tube is infinitely long. Equation $\nabla \times \mathbf{B} = \mu_0 \mathbf{J}_{\rm c}$ then becomes

$$\frac{\partial B}{\partial r} = \mu_0 \frac{J_{\rm c0}}{1 + B/B_1}. \tag{6.8}$$

A direct integration yields a homogeneous field in the hollow of the tube that assumes the form

$$B_{\mathrm{in}} \;=\; \begin{cases} 0 & \text{for } B_{\mathrm{a}} < B_{\mathrm{lim},\infty}, \\ -B_1 + \sqrt{(B_1 + B_{\mathrm{a}})^2 - 2d\mu_0 J_{\mathrm{c0}} B_1} & \text{for } B_{\mathrm{a}} > B_{\mathrm{lim},\infty}, \end{cases} \tag{6.9}$$

where $B_{\mathrm{lim},\infty}$, defined as

$$B_{\mathrm{lim},\infty} = -B_1 + \sqrt{B_1^2 + 2d\mu_0 J_{\mathrm{c0}} B_1}\,, \tag{6.10}$$

is the theoretical threshold induction assuming an infinite tube with no creep. Fitting equation (6.9) to experimental data in the region $B_{\mathrm{a}} > 14$ mT, we find $B_1 = 5$ mT and $J_{\mathrm{c0}} = 1782$ A/cm^2.

In practice, flux creep effects are present and the exponent n assumes a high, but finite, value. In our case, as is to be determined in section 6.3.4, we found $n \cong 25$. The filled squares of figure 6.10 show the simulated values of the internal induction versus the applied induction, B_{a}, for a tube with the dimensions of the sample and a flux creep exponent $n = 25$ entering (6.4). The $J_{\mathrm{c}}(B)$ relation (6.5) was introduced in the equations of the algorithm of Brandt with $B_1 = 5$ mT and $J_{\mathrm{c0}} = 1782$ A/cm^2. These numerical results reproduce the data fairly well. As in the experiment, a simulated value of B_{lim} can be obtained as the maximum applied induction for which the $DCSF$ is higher than 60 dB at the centre of the tube (6.7). With such a definition, we also obtain $B_{\mathrm{lim}} \cong 14$ mT from the simulations. We note that, even in the presence of flux creep with $n = 25$, the simulated B_{lim} has the same value as the one given in the Kim model, (6.10).

Modelling of the field penetration into a HTS tube

We now compare the penetration of the magnetic flux in a tube and in a bulk HTS cylinder through a numerical analysis. This comparison reveals the coexistence of different penetration mechanisms in the tube. An understanding of these mechanisms is necessary to predict the efficiency of a HTS magnetic shield.

We use the numerical model of Brandt introduced in section 4.5.1, with a flux creep exponent $n = 25$. In order to facilitate comparisons with results from the literature, we choose here the critical current density, J_{c}, to be independent of the local magnetic induction. We further wish to normalize the applied field to the full penetration field, H_{P}, that, in the limit $n \to \infty$, corresponds to the field for which the sample is fully penetrated and a current density J_{c} flows throughout the entire volume of the superconductor.

For a bulk cylinder of radius a_2 and length ℓ, H_{P} assumes the form [165]:

$$H_{\mathrm{P}} = \frac{J_{\mathrm{c}}\ell}{2} \ln\left(\frac{2a_2}{\ell} + \sqrt{1 + \frac{4a_2^2}{\ell^2}}\right). \tag{6.11}$$

In the limit $\ell \to \infty$, one recovers the Bean limit $H_{\mathrm{P}\infty} = J_{\mathrm{c}}\, a_2$. An approximate expression of H_{P} for a tube can be obtained with the energy minimization approach developed in [167]:

$$H_{\mathrm{P}} = J_{\mathrm{c}}\frac{\ell}{2}\,\frac{1-\delta}{1+\delta}\,\ln\left[\frac{2a_2(1+\delta)}{\ell} + \left(1 + \left(\frac{2a_2(1+\delta)}{\ell}\right)^2\right)^{1/2}\right], \tag{6.12}$$

with $\delta = a_1/a_2$. An interesting observation is that (6.12) can be rewritten as:

$$H_{\mathrm{P}} = J_{\mathrm{c}} d \frac{\ell}{4\bar{a}}\,\ln\left[\frac{4\bar{a}}{\ell} + \left(1 + \left(\frac{4\bar{a}}{\ell}\right)^2\right)^{1/2}\right] \tag{6.13}$$

where $\bar{a} = (a_1 + a_2)/2$ is the mean radius. This shows that the correction to the field H_{P} of an infinite tube, $H_{\mathrm{P}\infty} = J_{\mathrm{c}}(a_2 - a_1) = J_{\mathrm{c}}\, d$, depends only on the ratio $\ell/\bar{a}$. Physically, this ratio is a measure of the importance of end effects.

Consider then the cylinder and the tube of figure 6.11, both of external radius a_2 and length $\ell = 6\, a_2$. The inner radius of the tube is $a_1 = 0.5\, a_2$. Both samples are subjected to an increasing axial magnetic induction, with $\dot{B}_{\mathrm{a}}(t) = E_{\mathrm{c}}/a_2$ and $B_{\mathrm{a}}(0) = 0$.

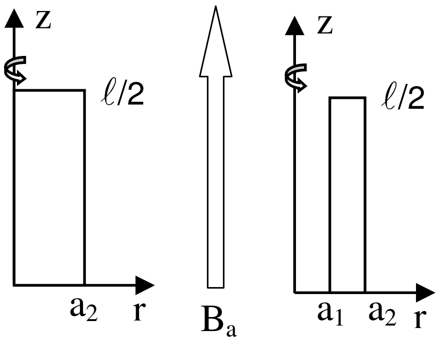

Figure 6.11: cylinder and tube of outer radius a_2, and length $\ell = 6\ a_2$ subjected to an axial magnetic induction $\mathbf{B}_{\mathrm{a}} = B_{\mathrm{a}}\hat{z}$. Only the region $0 \leq r \leq a_2$ and $0 \leq z \leq \ell/2$ is depicted for symmetry reasons.

Figure 6.12 shows a comparison of the simulated flux front for the cylinder (a) and for the tube (b) as a function of the applied magnetic induction. Here, the flux front corresponds to the locus of positions at which the current density rises to $J_{\mathrm{c}}/2$. To label the front as a function of the applied induction, we have taken as a reference magnetic field the full penetration field, H_{P}, whose expression is given in (6.11) and (6.12), both for the bulk cylinder and for the tube. The flux front is depicted for different external magnetic inductions with $B_{\mathrm{a}}/(\mu_0 H_{\mathrm{P}}) = 0.1, 0.3, 0.5,$ and 0.7. We note that the front shapes are similar to those obtained by Navau et al. [167], which used an approximate method based on the minimization of the total magnetic energy to study the field penetration into bulk and hollow cylinders. Due to the finite length of the samples, the flux front is curved in the end region $z \cong \ell/2$. Remarkably, this curvature implies that the magnetic flux progresses faster towards $z = 0$ along the inner boundary of the tube ($r = a_1$) than the magnetic flux penetrates the central region near $z = 0$ in a bulk cylinder. Thus, two penetration routes coexist for the

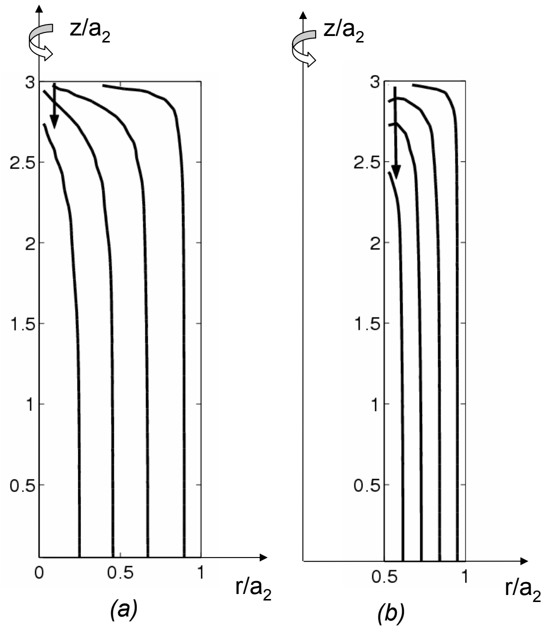

Figure 6.12: cylinder (a) and tube (b) of outer radius a_2, of length $\ell = 6\,a_2$ subjected to an axial magnetic field. The internal radius of the tube is $a_1 = 0.5\,a_2$. The samples are characterized by field independent J_c and n values ($n = 25$). As flux lines are symmetric about $z = 0$ and $r = 0$, only the region $0 \leq r \leq a_2$ and $0 \leq z \leq \ell/2$ is depicted. The contour curves show the flux front at $B_\mathrm{a} = 0.1, 0.3, 0.5, 0.7\ \mu_0 H_\mathrm{P}$ where H_P is the field of full penetration.

tube: the magnetic field can penetrate either from the external boundary at $r = a_2$, as in the cylinder, or from the internal boundary at $r = a_1$, via the two openings.

Consider next the field lines [2] for the cylinder and for the tube submitted to axial fields equal to half of their respective field H_P (see figure 6.13). The shape of the field lines in the region near $z = b$ are seen to be very different for the cylinder and for the tube. In particular, for the tube, the component B_z is negative near the opening and close to the inner boundary, as seen in the dashed circle of figure 6.13(b). Such a behaviour is reminiscent of the field distribution found in the proximity of a thin ring [168, 169, 170, 171].

The existence of a negative B_z inside the hollow part of the tube can be interpreted as follows. For an infinitely long tube, the magnetic field can only penetrate from the external surface and the field lines are parallel to the axis of the tube. As the length ℓ of the tube decreases, the flux lines spread out near $z = \ell$ due to demagnetization effects. As a result, shielding currents in the end region of the tube fail to totally shield the applied field and a non-zero magnetic field is admitted through the opening. The shielding currents flow in an extended region in the periphery of the superconductor. In the superconductor, ahead of the flux front, there is no

---

[2] A general difficulty arises when one tries to visualize 3D magnetic field lines with axial symmetry in a 2D plot. Here, we have used contours of the vector potential $A(r, z)$ at equidistant levels. Another possibility would be to use contours of $rA(r, z)$ at non-equidistant levels. Brandt has shown [120] that both approaches provide reasonably good approximations of the field lines.

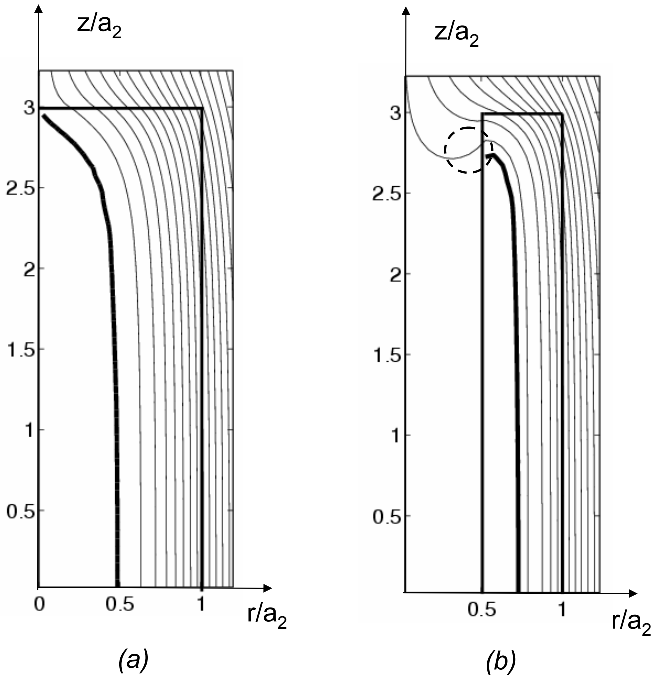

Figure 6.13: cylinder (a) and tube (b) of external radius a_2 and length $\ell = 6\,a_2$ subjected to an axial magnetic field. The samples are characterized by J_c and n values independent of the local magnetic induction ($n = 25$). Only the region $0 \leq r \leq a_2$ and $0 \leq z \leq \ell/2$ is depicted. The applied induction is 0.5 $\mu_0 H_\mathrm{P}$. The thick line represents the flux front ($J = J_\mathrm{c}/2$) and the thin lines represent the magnetic field lines. One can observe negative components B_z in the dashed circle of figure (b).

shielding current and hence no electric field. Integrating Faraday-Lenz's law along a contour lying in a non-penetrated region thus gives zero, meaning that the flux threaded by this contour must also be null. (As a reminder, the sample is cooled in zero-field.) Therefore, the magnetic flux due to the negative component B_z near $r = a_1$ is there to cancel the positive flux that has been allowed in the hollow of the tube near the axis.

Uniformity of the field attenuation in a HTS tube

Since magnetic flux can penetrate both through the outside surface and through the openings, it is relevant to investigate how the magnetic induction varies in the hollow of the tube. Numerical simulations show that the variation of the shielding factor along the radius is much smaller than the variation along the z-axis. We thus concentrate on the latter and study the DC shielding factor as a function of z at $r = 0$.

Figure 6.14 shows the variation of $DCSF$ along the z-axis as a function of the external induction B_a. The geometrical parameters are those of the sample studied experimentally and the $J_\mathrm{c}(B)$ relation with $B_1 = 5$ mT and $J_{\mathrm{c}0} = 1782$ A/cm^2 determined above is used. As the curve $DCSF(r = 0, z)$ is symmetric about $z = 0$, only the portion $z > 0$ is shown. Three different behaviours can be observed: in region 1, the shielding factor is nearly constant; in region 2, it starts decreasing smoothly; it falls off as an exponential in region 3, which is roughly defined as the region for which $z > \ell/2 - 2a_2$.

A useful result is known for semi-infinite tubes made of type-I superconductor and subjected to a weak axial field. In the Meissner state, the magnitude of the internal induction, $B_{\mathrm{in}}(r = 0, z)$, decreases from the extremity of the tube $z = \ell/2$ [44] as

$$B_{\mathrm{in}}(r = 0, z) \propto \mathrm{e}^{-C(\ell/2-z)/a_1}, \tag{6.14}$$

where a_1 is the inner radius, and $C \approx 3.83$ is the first zero of the Bessel function of the first kind $J_1(x)$. This result holds for $\ell/2 - z \gg a_1$ and implies that the shielding factor increases as an exponential of $\ell/2 - z$. An exponential dependence has also been measured in some HTS materials for applied fields above H_{c1} [31, 78]. Other measurements [151] in similar conditions have shown instead a uniform shielding factor in a region around the centre of the tube.

From the simulation results we see that both behaviours can actually be observed in a type-II tube, provided the ratio $\ell/\bar{a}$ is large. For the sample studied in this section, this ratio is equal to $\ell/\bar{a} \sim 11$. The exponential falling-off approximately follows the law $DCSF(r = 0, z) \sim \exp(C(\ell/2 - z)/a_1)$ (black solid line of figure 6.14) for the lowest fields only, but appears much softer for the larger magnitudes B_{a}.

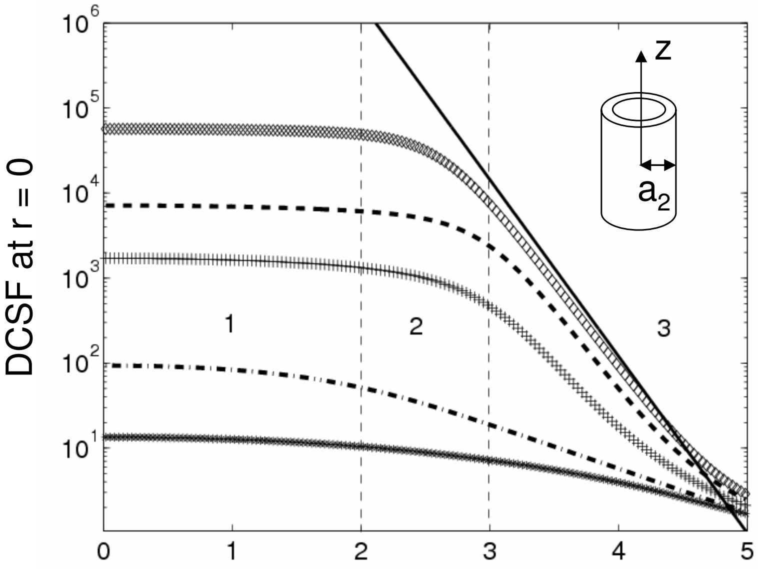

Figure 6.14: simulated variation of the DC shielding factor along the z-axis for increasing applied inductions. From top to bottom : $B_{\mathrm{a}}/B_{\mathrm{lim}} = 0.8, 0.9, 1, 1.05$, and 1.1. The threshold B_{lim} is determined as the maximum applied induction for which the $DCSF$ is higher than 60 dB at the centre of the tube. The geometry is identical to that of the sample studied experimentally. The black solid line is the equation $DCSF(r = 0, z) = \mathrm{e}^{C(\ell/2-z)/a_1}$ (see text). For symmetry reasons, only the upper half of the tube is shown.

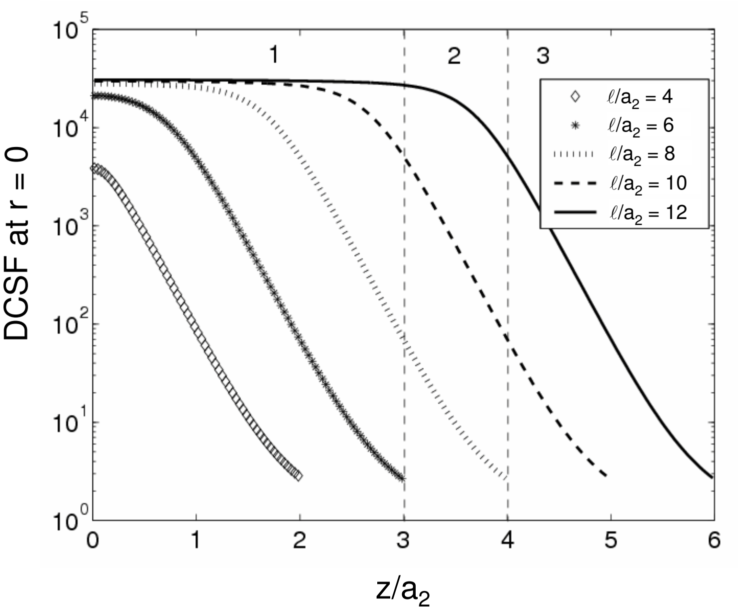

Figure 6.15: simulated evolution of the DC shielding factor along the axis for different lengths, ℓ. The internal and external radii, a_1 and a_2, are kept fixed ($a_1 = 0.8\ a_2$). The applied induction is $B_{\mathrm{a}} = 0.85\ B_{\mathrm{lim}}$.

The two behaviours — a nearly constant shielding factor and an exponential decrease of this factor — can be associated with the two mentioned penetration routes. For the part of the flux that penetrates via the openings, we expect the shielding factor to increase as an exponential of $(\ell/2 - z)$ as one moves away from the extremity. This is the behaviour observed in type-I shields, for which no flux can sweep through the side wall if $d \gg \lambda$, where λ denotes the London penetration depth. By contrast, in the centre region, for a tube with a large $\ell/\bar{a}$ ratio, the flux penetrating via the openings is vanishingly small and flux penetration through the walls prevails. This leads to the nearly constant shielding factor observed in region 1. As the ratio $\ell/\bar{a}$ increases, flux penetration through the wall strengthens. As a result, the plateau region increases in size as is confirmed in figure 6.15, which shows $DCSF(r = 0, z)$ for five different lengths ℓ/a_2 (the outer radius and the width $d = a_2 - a_1 = 0.2\,a_2$ are kept fixed) and for $B_{\mathrm{a}} = 0.85\ B_{\mathrm{lim}}$. Note that the plateau of the shielding factor disappears for the smallest ratios $\ell/\bar{a}$ (for $\ell \leq 6a_2$) as for these ratios, flux penetration through the openings competes with that through the wall.

This last example shows that it is important to distinguish B_{lim}, which we have defined as the maximum applied induction for which $DCSF(0, 0)$ is larger than 60 dB, from $\mu_0 H_{\mathrm{P}}$, which corresponds to the full penetration of the sample. In fact, for $\ell < 6\,a_2$, the attenuation falls below 60 dB before the sample is full penetrated. If ℓ is further reduced, $\ell \leq 2\,a_2$, it is actually not possible to define an induction B_{lim}, as $DCSF(0, 0)$ is lower than 60 dB for any applied induction. Therefore, the interest of using short open HTS tubes for magnetic shielding applications is very limited.

When $\ell \geq 6\,a_2$, the value of B_{lim} is very close to the applied field for which the sample is fully penetrated, as the main penetration mechanism is the non-linear magnetic diffusion through the superconducting wall. To evaluate $B_{\rm lim}$, one could then use (6.12), which for $\ell \geq 6\,a_2$, is close to $H_{\rm P\infty} = J_{\rm c}d$. However, this formula can be misleading for understanding the influence of the wall thickness, d. Expressions (6.12) or $H_{\rm P\infty} = J_{\rm c}d$ were established ignoring the variation of $J_{\rm c}$ with B and show a linear dependence of $B_{\rm lim}$ as a function of d. However, the decrease of $J_{\rm c}$ with the local induction yields a softer dependence as can be seen in (6.10). There, $B_{\rm lim} \approx B_{\rm lim,\infty}$ is linear in d only for thicknesses d much smaller than $B_1/(2\mu_0 J_{\rm c0}) \approx 0.1$ mm, but grows as $\sqrt{d}$ for larger thicknesses if one takes the $J_{\rm c0}$ and B_1 parameters of the commercial HTS tube of table 6.1. Thus, if one wants to shield high magnetic inductions (larger than 100 mT) with a superconductor similar to the commercial one, unreasonably thick wall thicknesses are required. In this case, it is advisable to first reduce the field applied to the superconductor by placing a ferromagnetic screen around it.

A final remark concerns the effect of the width of the superconducting wall, d, on the spatial dependence of $DCSF$. If d is increased while the ratio $B_{\rm a}/B_{\rm lim}$ is kept fixed, the shielding factor increases in magnitude but its z-dependence remains qualitatively the same.

In this section, we used a quasistatic applied field. The results concerning the spatial variation of the field attenuation are expected to be still valid in the case of an AC field.

6.3.4 Results in the AC mode

The sensing coil of the setup described in section 6.2.2 can move along the axis of a tubular sample. In this section, we present the measured variation of the AC shielding factor along the axis of the tube and compare it to numerical simulations for which an AC applied induction is used. The AC shielding factor, $ACSF$, is defined in a similar way as for the planar samples:

$$ACSF(r,z) = \frac{B_{\rm a,RMS}}{B_{\rm in,RMS}(r,z)}, \tag{6.15}$$

where $B_{\rm a,RMS}$ is the RMS value of the applied magnetic induction and $B_{\rm in,RMS}(r,z)$ is the RMS value of the fundamental component of $B_{\rm in}(r,z) = \sqrt{B_{\rm r}^2(r,z) + B_{\rm z}^2(r,z)}$, which can be directly measured by the lock-in amplifier. In this section, we also measure the frequency response and interpret the results with scaling laws arising from the constitutive law $E \propto J^n$.

Experimental results

The variations of the measured AC shielding factor $ACSF$ defined in (6.15), along the axis of the sample studied experimentally for a fixed frequency and varying amplitudes of the applied field are shown in figure 6.16 (filled symbols). Apart from the upper curve of figure 6.16 corresponding to $B_{\rm a,RMS} = 10.8$ mT, we observe a nearly constant measured shielding factor in the central region. Going further to the extremity of the tube, near $z = 5\,a_2$, $ACSF$ decreases as an exponential.

Figure 6.17 (filled symbols) shows a measurement of the AC shielding factor, $ACSF$, as a function of frequency for two applied magnetic inductions when the magnetic sensor is placed at the centre of the sample. The frequency dependence appears to follow a power law.

Figure 6.18 shows the evolution of the AC shielding factor measured at the centre of the tube at a fixed frequency $f = 103$ Hz and for varying RMS values of the applied induction. The shielding factor decreases with $B_{\mathrm{a,RMS}}$.

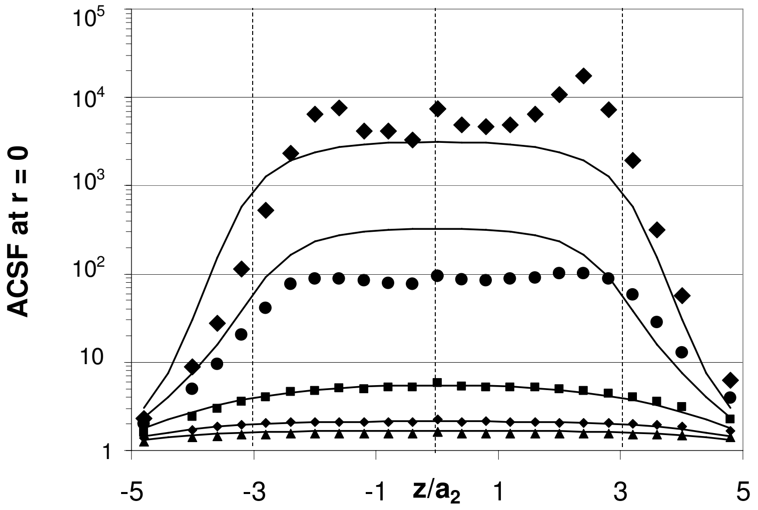

Figure 6.16: experimental and simulated variation of the AC shielding factor along the axis of the sample, at a frequency $f = 103$ Hz. Filled symbols : measurement. Continuous lines : simulation. From top to bottom: $B_{\mathrm{a,RMS}} = 10.8$, 12, 13.4, 15.3, and 16.6 mT.

Uniformity of the field attenuation

The solid lines of figure 6.16 represent the simulated $ACSF$ for the applied inductions used during the measurement. As in the DC case, we observe a constant shielding factor around the centre $z = 0$ of the tube whereas $ACSF$ falls off exponentially near the opening ends $z = 5\,a_2$. Remarkably, one can observe a relatively good quantitative agreement between simulated and experimental results of figure 6.16. For $B_{\mathrm{a,RMS}} = 10.8$ mT, local variations of the measured $ACSF$ can be observed for $|z|/a_2 < 3$. In particular, the maximum shielding factor is no longer located at the centre of the tube, and shielding appears to be asymmetric in z. For higher values of the applied magnetic induction, the maximum $ACSF$ lies at $z = 0$ and shielding recovers its symmetry about the centre of the tube. These effects are supposed to be due to non-uniform superconducting properties, see chapter 7.

Scaling laws and frequency response

The strong non-linearity of the constitutive law $E = E_{\mathrm{c}}(J/J_{\mathrm{c}})^n$ gives rise to frequency scaling laws with $n-$dependent power exponents, see section 4.3.1. Then, if

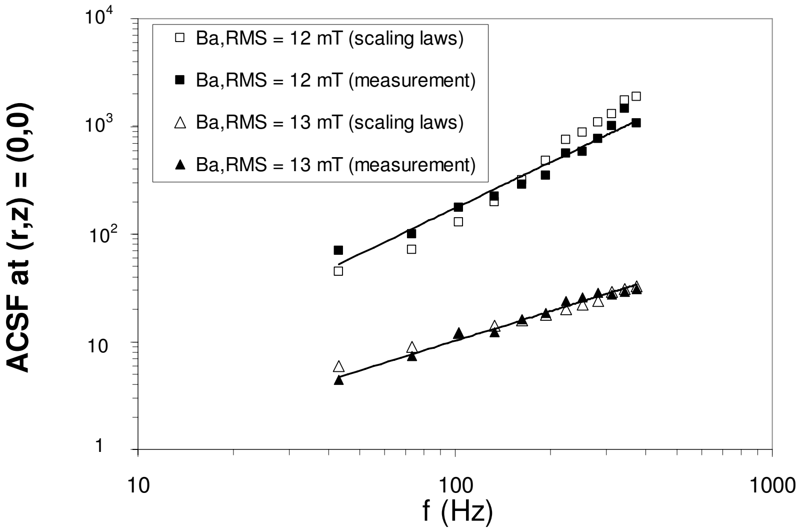

Figure 6.17: AC shielding factor versus frequency at the centre of the tube. The filled symbols come from a direct measurement and the open symbols correspond to an estimation based on scaling laws (see text). The two lines show that the variation of the AC shielding factor with the frequency is close to a power law.

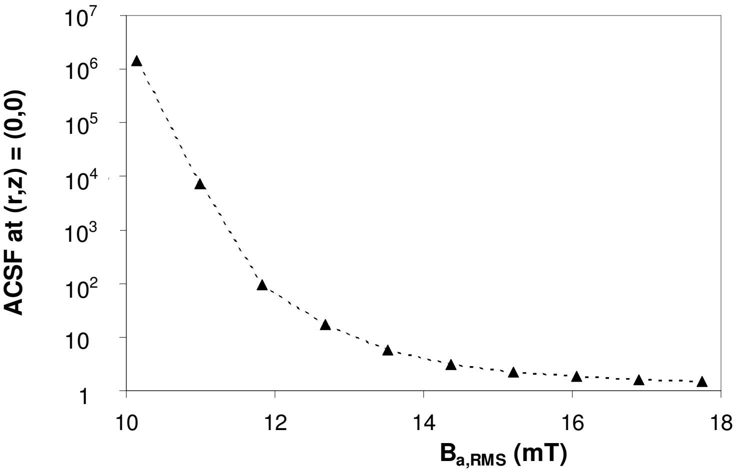

Figure 6.18: measured AC shielding factor at the centre of the sample versus the RMS value of the applied magnetic induction $B_{\mathrm{a,RMS}}$. Its frequency is kept fixed at $f = 103$ Hz.

one knows the $ACSF$ corresponding to the applied induction B_a at the frequency f, $ACSF(B_\mathrm{a}, f)$, one can deduce the $ACSF$ corresponding to the magnetic induction $B_{\mathrm{a,new}} = B_\mathrm{a} c^{1/(n-1)}$ at the frequency $f_{\mathrm{new}} = c\,f$, $c > 0$, by using:

$$ACSF(B_{\mathrm{a,new}}, f_{\mathrm{new}}) = ACSF(B_\mathrm{a}, f), \tag{6.16}$$

as $ACSF$ is the ratio of two magnetic inductions and is thus invariant under scaling. Then, the frequency dependence of $ACSF$ in figure 6.17 can be reproduced as follows using these scaling laws. First, we approximate the curve of figure 6.18 by piecewise exponentials, which gives $ACSF(B_{\mathrm{a}}, 103\ \mathrm{Hz})$. Second, we use (6.16) and write:

$$ACSF(12\ \mathrm{mT}, f_{\mathrm{new}}) = ACSF(B_{\mathrm{a}}, 103\ \mathrm{Hz}), \tag{6.17}$$

with

$$\begin{aligned} B_{\mathrm{a}} &= B_{\mathrm{a,new}}\, c^{-1/(n-1)} && (6.18)\\ &= 12\ \mathrm{mT} \left(\frac{103}{f_{\mathrm{new}}}\right)^{1/(n-1)} && (6.19) \end{aligned}$$

Hence, the variations with respect to B_{a} in figure 6.18 can be translated into frequency variations at a fixed induction. This gives the upper curve of figure 6.17 (open symbols) for which we used $n = 25$. The lower curve is obtained by fixing $B_{\mathrm{a,new}}$ to 13 mT. This construction thus demonstrates that the frequency variation intrinsically arises from scaling laws.

The detailed construction relies on a specific value of the creep exponent n, which we have taken here to be equal to $n = 25$ and independent of B. Analysing the frequency dependence with scaling laws thus also serves the purpose of determining the value of n that best fits experimental data. A HTS shield characterized by a lower n value would present a more pronounced frequency dependence of the shielding factor.

One may wonder on the role played by the increased dissipation, due to the motion of vortices, as frequency is increased. Such a dissipation can lead to a temperature rise, a decrease of the critical current density, and thus a decrease of the shielding factor. Nevertheless, it appears from figure 6.17 that the temperature increase must remain small in the frequency window investigated in our experiment (43 Hz – 373 Hz), as no significant reduction of $ACSF$ can be observed in that frequency range. One may equally wonder on the role played by the different harmonics of the internal magnetic induction. For the applied fields we consider here, the fundamental component strongly dominates the higher harmonics. As as consequence, the curves of figures 6.17 and 6.18 are not significantly affected if one takes the RMS value of the total internal magnetic induction, rather than its fundamental component, to define the shielding factor in the AC mode.

6.4 Magnetic shielding properties of a HTS EPD tube in the parallel geometry

In the previous section, we have shown that a commercial HTS tube can strongly attenuate an axial magnetic field. Here, we present the shielding properties of a tubular sample which was made by the EPD technique. The sample consists of a Y-123 coating deposited on the external surface of a silver tube. Its main characteristics are summarized in table 6.2. The critical temperature which is given in this table is the one obtained with planar EPD samples prepared in the same conditions, see chapter 4.

Material	$Y_1Ba_2Cu_3O_{7-\delta}$ coating on a silver tube
Length	$\ell = 10$ cm
Inner radius	$a_1 = 1$ cm
Thickness of the substrate	$t = 0.5$ mm
Thickness of the HTS layer	$d = 50\ \mu$m
Critical temperature	$T_c \cong 90$ K

Table 6.2: physical characteristics of the EPD HTS tube.

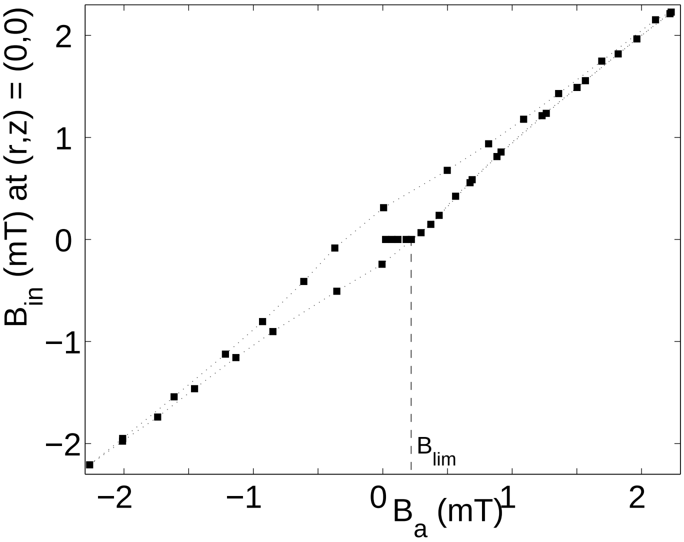

Figure 6.19: evolution of the internal magnetic induction versus the applied induction for the EPD tube of table 6.2.

6.4.1 DC mode

To evaluate the shielding properties of the tube of table 6.2 in the DC mode, we use the experimental setup of section 6.2.1, as for the commercial sample. Figure 6.19 shows the evolution of the internal magnetic induction at the centre of the tube, $B_{\mathrm{in}}(0,0)$, versus the applied axial induction. The sample of table 6.2 was cooled down to 77 K in zero-field conditions. Then we applied an increasing magnetic induction and reached $B_{\mathrm{a}} = 2.2$ mT. Upon decreasing the applied induction to $B_{\mathrm{a}} = -2.2$ mT and increasing it again up to $B_{\mathrm{a}} = 2.2$ mT, the internal induction is seen to follow a hysteretic curve. Below $B_{\mathrm{a}} \cong 0.2$ mT, it is no longer possible to measure B_{in} with our measurement system which has a sensitivity around 1 μT. Hence, we deduce $B_{\mathrm{lim}} \cong 0.2$ mT. As for the commercial tube, B_{lim} roughly corresponds to the applied induction for which the curve of first magnetization reaches the hysteresis cycle.

The threshold induction of the EPD tube is about 70 times smaller than the one of the commercial tube, for which we had $B_{\mathrm{lim}} \cong 14$ mT. The thicknesses of the superconducting walls, d, also differ: d is $\sim$ 30 times larger for the CAN tube. Hence, the difference between the B_{lim} values seems mainly due to to the difference of the thickness of the superconducting wall.

6.4.2 AC mode

Using the experimental setup working in the AC mode (system of section 6.2.2), we now study the variation of $ACSF$ for the EPD tube with respect to the applied induction, and along the tube axis. The sample was first cooled down to 77 K, and then subjected to an AC axial magnetic field having a frequency of 103 Hz. In these conditions, the attenuation by the silver substrate is given in a first approximation by $e^{0.5/2.7} \cong 1.2$, where 0.5 mm is the thickness of the silver tube, and 2.7 mm is the skin depth of silver at 77 K and 103 Hz.

Figure 6.20 shows the variation of the $ACSF$ versus the RMS value of the applied induction at the centre of the EPD tube, $(r, z) = (0, 0)$. We see that the $ACSF$ rises rapidly when the applied induction is lower than 0.3 mT. For higher applied inductions, $ACSF$ is around 1.3.

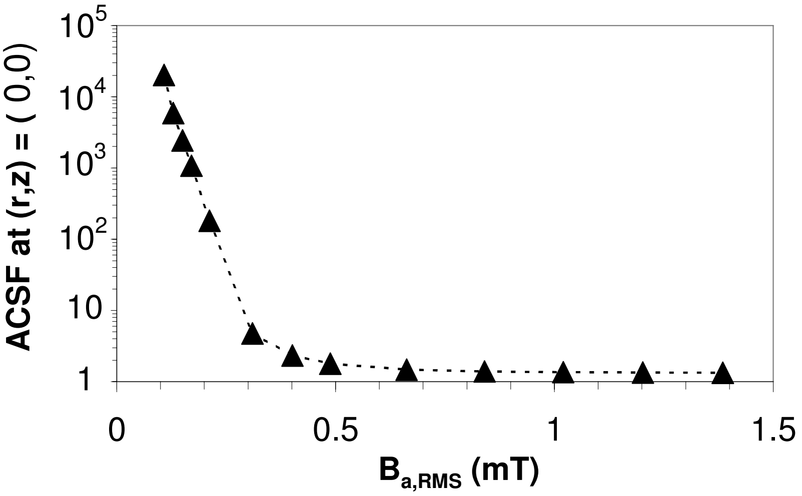

Figure 6.20: experimental AC shielding factor measured at the centre of the EPD tube of table 6.2 as a function of the RMS value of the applied magnetic induction, $B_{\mathrm{a,RMS}}$. The frequency of the applied field is $f = 103$ Hz.

Figure 6.21 shows the variation of the $ACSF$ along the tube axis for different applied magnetic inductions. The tube centre lies at $z = 0$. The measured $ACSF$ is not symmetric with respect to $z = 0$. In particular, the $ACSF$ is much lower for the negative z-values than for the positive ones. We also observe that the maximum $ACSF$ does not lie at the centre of the tube as expected for a uniform tube. Moreover, the position of this maximum changes with the magnitude of $B_{\mathrm{a,RMS}}$: it moves towards larger z values as $B_{\mathrm{a,RMS}}$ increases. These observations suggest that the tube does not have uniform superconducting properties along its axis: it is expected that they are better for positive z-values.

Nevertheless, this measurement shows that the EPD technique can be used to make a HTS magnetic shield up to 10 cm long. Some refinement has to be done in the sample preparation, in particular to improve the homogeneity of the superconducting properties. Our home-made experimental setup which works in the AC mode allows one to check this homogeneity along the axis of a HTS tube.

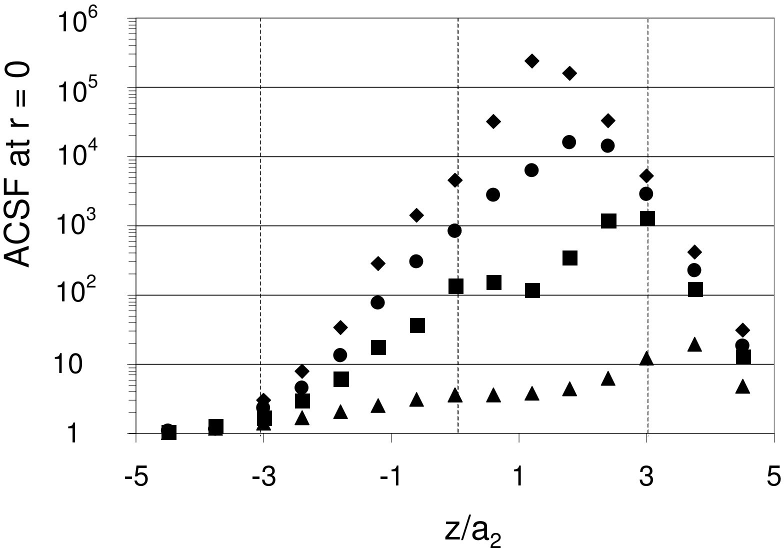

Figure 6.21: experimental variation of the measured AC shielding factor along the axis of the EPD tube of table 6.2, at the frequency $f = 103$ Hz. From top to bottom: $B_{\mathrm{a,RMS}} = 0.13$, 0.17, 0.21, and 0.31 mT.

Material	nickel (80%), iron (15%), molybdenum (4%), other elements (1%)
Length	$\ell = 8$ cm
Inner radius	$a_1 = 6$ mm
Thickness of the tube	$d = 1$ mm
Relative permeability at f=60 Hz	$\mu_{\mathrm{r}} = \mu_{\mathrm{r,max}} \cong 30000$ if $B = 100$ mT $\mu_{\mathrm{r}} \cong 20000$ if $B = 10$ mT
DC magnetic property	$\mathrm{d}B/\mathrm{d}H \cong \mu_0$ if $B \geq 800$ mT

Table 6.3: physical characteristics of the ferromagnetic tube (from the manufacturer).

6.5 Magnetic shielding properties of a ferromagnetic tube in the parallel geometry

In the two previous sections, we have seen that high shielding factors (higher than 10^4) can be obtained with HTS tubes in the parallel geometry. It would be interesting to compare these levels to those achieved by a ferromagnetic tube in the same field geometry.

We used a commercial ferromagnetic tube from the MuShield company [172], whose characteristics are given in table 6.3. Figure 6.22 shows the measured $ACSF$ at the centre of the tube as a function of the RMS value of the applied induction of frequency $f = 103$ Hz. The shielding mechanism of this tube is a combination of the skin effect and the concentration of magnetic flux in the ferromagnetic material (see chapter 1).

First, we see that the $ACSF$ does not vary in a monotonous way as the applied

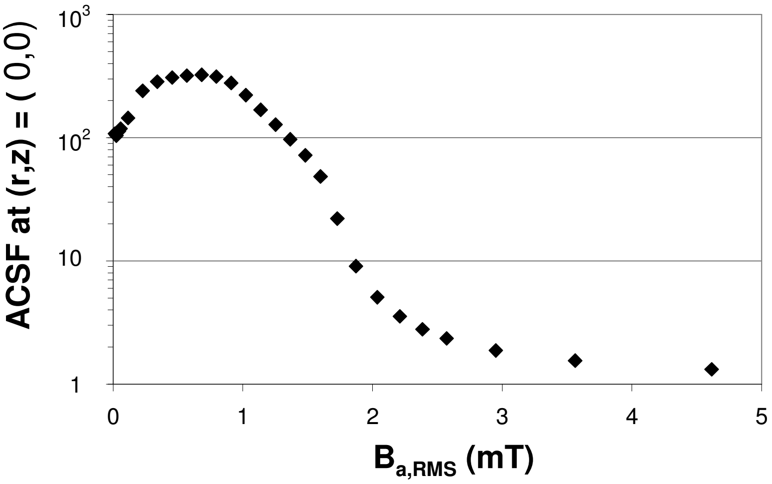

Figure 6.22: measured AC shielding factor at the centre of the ferromagnetic tube of table 6.3 at the frequency $f = 103$ Hz.

induction increases. This has to be related to the variation of the relative permeability with the magnetic induction. In particular, the maximum value of μ_{r} does not correspond to the relative permeability at very small B. This can explain that the maximum of the $ACSF$ is not reached at a non-vanishing value of $B_{\mathrm{a,RMS}}$.

Second, we see that the shielding factor obtained with the ferromagnetic tube is much smaller than the ones that we measured with the HTS tubes. Hence, as for the planar samples of chapter 5, HTS screens seem to be much more efficient to shield a low frequency magnetic field.

It is also interesting to compare the $ACSF$ of HTS tubes with that of a non magnetic conducting tube. In this case, the shielding factor does not depend upon the applied field. If we consider a copper tube at 77 K and 103 Hz, the $ACSF$ is roughly given by:

$$ACSF \cong \mathrm{e}^{t/\delta} \cong 1.74, \tag{6.20}$$

if the thickness of the tube is taken to be equal to 1.5 mm, which is the same thickness as the tube from CAN Superconductors (sample of table 6.1). This value is very small. To have a shielding factor of 10^4, a copper tube with a thickness equal to ~ 2.5 cm would be necessary. Hence, HTS can be very useful for screening a low frequency magnetic field.

6.6 Magnetic shielding properties of HTS tubes in the transverse geometry

We now consider the transverse geometry, which means that the field is applied perpendicular to the tube axis. This study is carried out both experimentally and theoretically.

For the experimental part, we use the commercial tube from CAN (table 6.1) with the measurement system described in section 6.2.1 (DC mode). For the theoretical part, we assume that the sample is infinitely long, see figure 6.23. In this case, the shielding currents flow along the tube axis, $\hat{z}$, if $\mathbf{B}_\mathrm{a} = B_\mathrm{a}\,\hat{x}$. To obtain the current distribution, we use the numerical method of Brandt described in section 4.5.2 with the same constitutive laws as in the parallel geometry, which means:

$$\mathbf{E} = E_\mathrm{c}\left(\frac{J}{J_\mathrm{c}}\right)^n \frac{\mathbf{J}}{J}, \tag{6.21}$$

$$J_\mathrm{c}(B) = \frac{J_{\mathrm{c}\,0}}{1 + B/B_1}, \tag{6.22}$$

with the n, $J_{\mathrm{c}\,0}$, and B_1 values determined in the parallel geometry ($n = 25$, $J_{\mathrm{c}\,0} = 1782$ A/cm^2, and $B_1 = 5$ mT). As explained in chapter 4, the equations to solve in the transverse case are very similar to that in the parallel geometry. Only the integral kernel has to be changed.

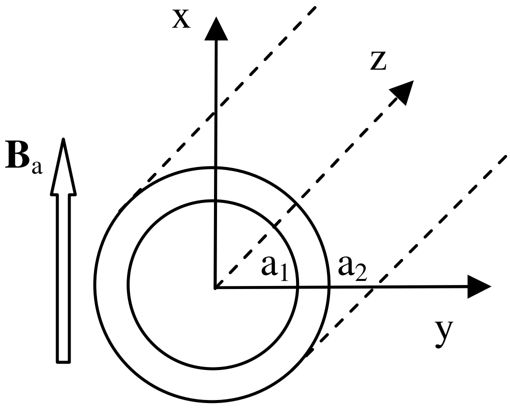

Figure 6.23: geometry used for the theoretical study in the transverse case. The geometry is an infinitely long tube subjected to a uniform transverse magnetic induction $\mathbf{B}_\mathrm{a} = B_\mathrm{a}\,\hat{x}$.

6.6.1 Results

The sample has been cooled down to 77 K in zero-field conditions, and the induction at the centre of the tube has been measured for different magnetic inductions applied perpendicular to the tube axis. Figure 6.24(a) shows the evolution of the internal magnetic induction as a function of the applied transverse induction. The open circles represent the measurement, and the filled squares represent the simulation. For comparison, the curve obtained in the parallel geometry is shown in figure 6.24(b).

The threshold induction, B_lim, is lower when the applied field is transverse. We have $B_\mathrm{lim} \cong 8$ mT in the transverse geometry, whereas $B_\mathrm{lim} \cong 14$ mT in the parallel case.

Two elements explain that B_lim is lower in the transverse case. First, assuming that the tube is infinitely long, the demagnetizing factor N is equal to 0.5 in the

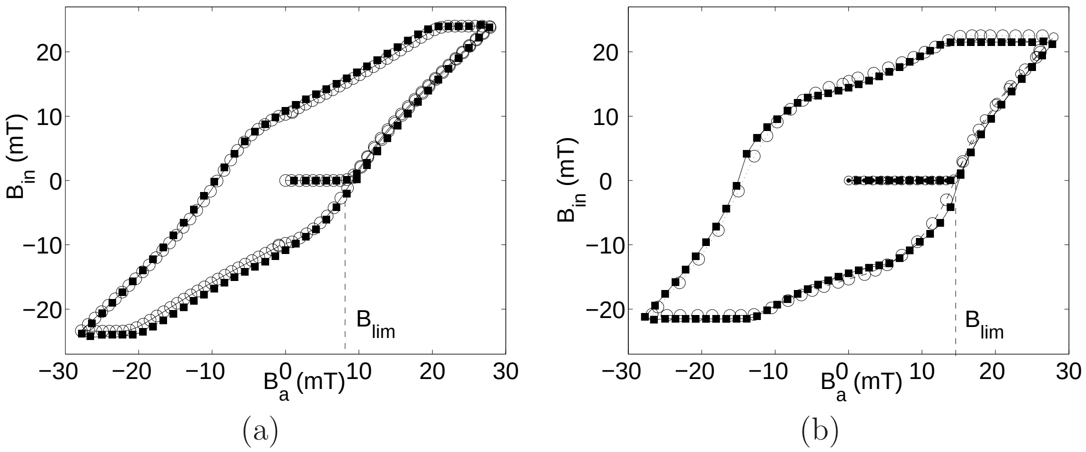

(a) (b)

Figure 6.24: evolution of the internal magnetic induction at the centre of the commercial HTS tube (table 6.1), as a function of the magnetic induction applied perpendicular (figure (a)) or parallel (figure (b)) to the tube axis. The sample is cooled down to $T = 77$ K in zero-field conditions. The open circles represent the measurement, and the filled squares represent the simulation.

transverse geometry, and to 0 in the parallel geometry (see chapter 1). Because of the demagnetizing effects, the full penetration field, H_{P}, is lower when the magnetic field is applied perpendicular to the tube axis. When the tube is fully penetrated, it shields no longer efficiently.

Second, assuming that the tube is infinitely long, the applied magnetic field for which the inner cavity is reached by the flux front is lower than H_{P} in the transverse case. This is illustrated in figure 6.25 which shows the calculated field lines in the transverse case if $B_{\mathrm{a}} = 0.9\ B_{\mathrm{lim}}$. We see that the magnetic field has nearly reached the cavity in the plane $x = 0$, but the parts of the tube near $|x|/a_2 = 1$ are not penetrated yet. As $B_{\mathrm{lim}} \cong \mu_0 H_{\mathrm{P}}$ in the parallel geometry for an infinitely long tube, the threshold induction is larger when the applied field is axial.

This explanation is expected to be valid when the tube has a finite length if $\ell > 6\ a_2$. In this case, the end effects weakly affect B_{lim} (see section 6.3.3).

6.7 Summary

In this chapter, we studied the magnetic shielding properties of HTS tubular samples. This study has been carried out both theoretically and experimentally.

In a first part, we used the method of Campbell and Evetts to calculate the magnetic field penetration into infinitely long specimens when the magnetic field is applied parallel to the tube axis (parallel geometry). This study was carried out to determine what are the optimal shape and position of the hole in order to obtain the highest threshold induction, $B_{\mathrm{lim,Bean}}$. We found that, keeping the volume to be shielded constant, the solution which gives the highest $B_{\mathrm{lim,Bean}}$ consists in making a hole with the same shape as the sample cross-section, and with its centre at the centre of the sample. In this case, $B_{\mathrm{lim,Bean}} = \mu_0 H_{\mathrm{P}}$.

In a second part, we presented a detailed study of the magnetic shielding pro-

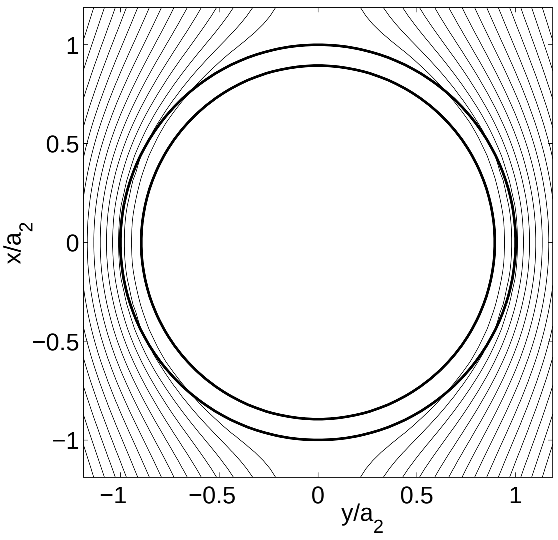

Figure 6.25: simulated magnetic field lines in the transverse geometry. The applied induction is $B_{\mathrm{a}} = 0.9\ B_{\mathrm{lim}}$, where $B_{\mathrm{lim}} = 8$ mT.

perties of a commercial polycrystalline Bi-2223 superconducting tube subjected to an axial field. We have measured the field attenuation with a high sensitivity for DC and AC source fields, and have confronted data with computer modelling of the field distribution in the hollow of the tube. The numerical model is based on the algorithm proposed by Brandt, see chapter 4. This study allows us to detail the variation of the shielding factor along the axis, interpret it in terms of the penetration mechanisms and take into account flux creep and its effects on the frequency dependence.

Our main findings are the following:

- A HTS tube can efficiently shield an axial induction below a threshold induction B_{lim}. As real HTS samples are not infinitely long, do not have a constant critical current density, and are not characterized by a creep exponent $n \to \infty$, B_{lim} generally differs from the value predicted by the Bean model, $B_{\mathrm{lim,Bean}}$. For the commercial sample, we obtained $B_{\mathrm{lim}} = 14$ mT. The threshold induction B_{lim} increases with the ratio $\ell/\bar{a}$ (ℓ is the length of the tube and $\bar{a}$ is the mean radius), the thickness of the tube, and depends on the exact $J_c(B)$ dependence. When the length of the tube decreases, B_{lim} rapidly decreases because of demagnetizing effects.

- There are two penetration routes in a HTS tube: one from the external surface of the tube, and one from the opening ends, the latter mechanism being suppressed for long tubes. These two mechanisms lead to a spatial variation of the shielding factor along the axis of the tube. In a zone extending between $z = 0$ (centre of the tube) and $z = \ell/2 - 3\,a_2$, the shielding factor is approximately constant when $\ell > 6\,a_2$ (a_2 is its external radius). Then it decreases as an exponential as one moves towards the extremity of the tube. As a consequence of this spatial dependence, no zone with a constant shielding factor exists for small tubes ($\ell < 6\,a_2$).

- The shielding factor increases with the frequency of the field to shield, following a power law. This dependence can be explained from scaling laws arising from the constitutive law $E \propto J^n$.

In a third part of our study, we compared the shielding factor of a HTS tube with that of a ferromagnetic tube, both in the parallel geometry, for a frequency of the field of 103 Hz. We found that much higher field attenuations can be obtained with a HTS shield. For a commercial ferromagnetic tube having a thickness equal to 1 mm, the maximum shielding factor is 320 ($\cong$ 50 dB) if the RMS value of the magnetic induction is $B_{\mathrm{a,RMS}} = 0.7$ mT. At 77 K and for the same applied induction, the shielding factor is higher than $10^6 \cong 120$ dB for the commercial Bi-2223 tube, which has a thickness equal to 1.5 mm. To obtain a shielding factor of 120 dB at 77 K and 103 Hz with a copper tube, a thickness equal to 3.7 cm $\cong 24 \times 1.5$ mm would be necessary.

In the final part of this chapter, we studied experimentally and numerically the field penetration into a HTS tube in the transverse geometry. For the theoretical part, we assumed that the tube is infinitely long. In this case, the direction of the shielding currents is known and the method of Brandt can be used to solve the problem. In the transverse case, the threshold induction, B_{lim}, is lower than in the parallel geometry. Two facts explain such a situation. First, the full penetration field, H_{P}, is lower in the transverse case because of demagnetizing effects. Second, the applied field for which the cavity is reached by the flux lines is lower than H_{P}.

In the next chapter, using the numerical method of Brandt, we study the shielding properties of various axial symmetric samples in the parallel geometry.

Chapter 7

Numerical study: effects of a cap, a non-superconducting joint, and non-uniform superconducting properties

In the previous chapter, we studied experimentally and numerically the shielding properties of open HTS tubes that were subjected to a source field applied parallel to the tube axis. Three factors were considered to evaluate the quality of the shields: the threshold induction, B_{lim}, the spatial variation of the field attenuation, and the frequency response of the shield.

These results can be used to design better magnetic screens. For instance, putting a cap at both ends of the tube reduces the penetration from the extremities and thus raises the level of attenuation inside the tube. In practice, however, several design constraints must also be taken into account. For instance, electrical wiring is oftentimes needed to connect the inside and the outside of a magnetic shield. The wiring should be placed so that the shielding action is the least perturbed. In particular, a wiring hole is best made where the field is the weakest, which for a closed cylinder corresponds to the centre of one of the closing caps.

Other design constraints arise when considering large shields, typically of dimensions larger than a few centimetres. Because of the brittleness of HTS ceramics, large samples tend to develop cracks and defects, and to a degree which depends on the particular processing used, may exhibit non-uniform superconducting properties. The precursor powder always contains a small amount of impurities. The particles of the initial powder are not spherical and, as they pack on one another, the density of the obtained material can vary as a function of the position inside the material. A change of density induces local variations of the critical current density, J_{c}. Other factors, specific to the fabrication technique, also induce non-uniformity in the material. For polycrystalline samples made by isostatic pressing, local variations of the density are induced by the pressing step [173]. If the sample is made with the EPD technique, the stability of the initial suspension strongly determines the homogeneity of the superconducting coating [97, 98, 140]. The presence of clusters has to be suppressed. Moreover, oxygenation and sintering must be done in a furnace with a uniform temperature and a controlled atmosphere. A spatial variation of the oxygen diffusion can lead to non-uniform superconducting properties. A temperature gradient in the furnace can also induce variations of J_c, as some parts of the sample are more melted than others. In practice, these requirements can be difficult to match when using large furnaces. An alternative for making large HTS magnetic shields is to join smaller tubes which are sintered separately.

The purpose of this chapter is to extend the study of chapter 6 to HTS magnetic shields designed with constraints that are dictated by the applications[1]. As in section 6.3, we consider axisymmetric samples in the parallel geometry, which means that the source field is applied parallel to the sample axis. We consider three different illustrative systems:

1. a tube closed with two caps, each containing a wiring hole,
2. an open tube made of smaller tubes that are joined with a normal material,
3. an open tube having non-uniform superconducting properties.

The shielding properties of these systems are studied as a function of their geometry. To our knowledge, analytical expressions of the threshold induction $B_{\rm lim}$, or of the spatial variation of the field attenuation, are not available for these non trivial geometries. We thus resort to numerical simulations, and follow the method of Brandt [120] which was explained in section 4.5.1. A numerical study has the advantage of treating perfectly specified systems; it thus allows us to consider one effect at a time. Carrying out a similar study by experimental means is, however, much more difficult. Due to the many steps involved in fabricating large superconducting shields, many effects can cause deviations from theory, see for instance section 6.4. These effects often act simultaneously, which makes data interpretation arduous. Our work is meant to be a first approximation study of the problems encountered with large superconducting shields. Being numerical, and not experimental, this approach should be taken as providing a rough guideline for the design of HTS magnetic shields. More work is of course required to apply this guideline for building real systems. As a reminder, we nevertheless have shown in section 6.3 that the simulations following the method of Brandt reproduce the experimental data with good accuracy for open tubes.

The chapter is organized as follows. In section 7.1, we detail the constitutive laws, and the model parameters used in our numerical study. After, we present and discuss our numerical results. First, we compare the shielding properties of open and closed tubes (section 7.2). Second, we study how a non-superconducting ring affects the field penetration into an open tube (section 7.3). Third, the shielding capabilities of an open tube having non-uniform superconducting properties are presented (section 7.4). We conclude in section 7.5.

7.1 Constitutive laws and model parameters

We focus on polygrain materials which consist of a large number of grains separated by weak links [175, 176]. We assume that the shielding polycrystalline material

---

[1] The material in this chapter has been reported in [174]

satisfies the three following constitutive laws:

$$\mathbf{B} = \mu_0 \mathbf{H}, \tag{7.1}$$

$$\mathbf{E}(J) = E_c \left(\frac{J}{J_c}\right)^n \frac{\mathbf{J}}{J}, \tag{7.2}$$

and

$$J_c(B) = \frac{J_{c0}}{1 + B/B_1}. \tag{7.3}$$

In order to take realistic parameters n, J_{c0}, and B_1, we take the same values as the ones determined for the commercial HTS tube of table 6.1. As a reminder, we had:

$$n = 25, \tag{7.4}$$

$$J_{c0} = 1782 \text{ A/cm}^2, \tag{7.5}$$

$$B_1 = 5 \text{ mT}. \tag{7.6}$$

We further assume that the external magnetic induction is varied with a constant sweep rate given by

$$\dot{B}_a = \pm\, E_c/a_2 \cong \pm\, 12.5 \text{ mT/s}. \tag{7.7}$$

Hence, we work in the DC mode of chapter 6. The plus (minus) sign corresponds to increasing (decreasing) applied inductions. This temporal evolution allows one to follow the full hysteretic curve of the superconducting shield. Results corresponding to faster or slower temporal ramps can be directly obtained from the results we present here by applying the scaling laws described in section 4.3.1.

7.2 Comparison of the shielding properties of open and closed tubes

Closed tubes should present better shielding properties than open tubes, as one expects the penetration from the extremities to be reduced in the presence of a cap. However, allowing an electrical connection between the inside and the outside of a shield is always necessary. In this section, we compare the shielding properties of the three following systems:

- system 1: an open tube (figure 7.1*(a)*);
- system 2: a tube closed by caps (figure 7.1*(b)*);
- system 3: a tube closed by caps, each pierced by a hole (figure 7.1*(c)*).

The three systems are depicted in figure 7.1. For symmetry reasons, only a quarter of each system is shown.

The three systems are subjected to an axial induction of magnitude B_a, which increases at a constant rate $\dot{B}_\mathrm{a} = E_\mathrm{c}/a_2$. We consider tubes with dimensions similar to that of the commercial HTS tube of table 6.1, which means a_2 = 8 mm, a_1 =

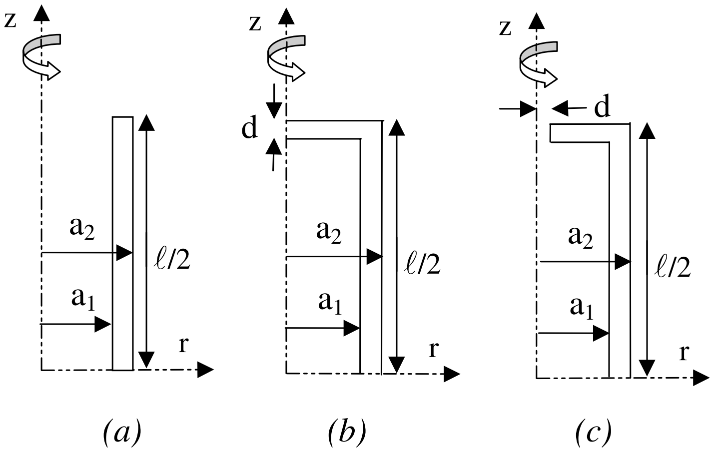

Figure 7.1: *(a)* system 1: open tube of length ℓ, with a wall thickness $d = a_2 - a_1 = 0.2\,a_2$; *(b)* system 2: closed tube with a cap of thickness $d = 0.2\,a_2$; *(c)* system 3: closed tube with a hole in the cap; the radius of the hole is $d = 0.2\,a_2$. For each system, the induction is applied along the z-axis. Only a quarter of each system is shown for symmetry reasons.

6.5 mm, and thus a superconducting wall thickness $d = a_2 - a_1 = 0.2\ a_2 = 1.5$ mm. The thickness of the cap and the radius of the holes of system 3 are also chosen equal to $d = 0.2\ a_2$. These represent realistic values, both for the thicknesses that can be practically obtained, for instance by isostatic pressing methods as in [164], and for the radius of the hole that is necessary for housing an electrical connection.

We first compare the threshold induction B_{lim} of the three systems as a function of the length ℓ. Afterwards, we compare the uniformity of the field attenuation realized by the three systems.

7.2.1 The threshold induction B_{lim}

Table 7.1 gives the values of B_{lim} for the three systems and for different values of the ratio ℓ/a_2. As in chapter 6, if $B_{\text{in}}(r,z)$ is the magnitude of the internal magnetic induction at the position (r,z), B_{lim} is the maximum applied magnetic induction for which the $DCSF$,

$$DCSF(r,z) = \frac{B_{\text{a}}}{B_{\text{in}}(r,z)}, \tag{7.8}$$

at $(r,z) = (0,0)$ (centre of the tube) is larger than 1000 (60 dB).

In table 7.1, one can notice that for short open tubes, with $\ell/a_2 \leq 2$, the field attenuation at the centre is lower than 60 dB for all applied inductions. It is therefore not possible to determine B_{lim} in these cases. In the range of ratios $2 \leq \ell/a_2 \leq 6$, the threshold induction can be defined and is found to be systematically higher for the closed tube than for the open one. For $\ell = 3\,a_2$, the value of B_{lim} for the closed tube is twice as large as that for the open tube. For ratios larger than $\ell = 5\,a_2$, the parameters B_{lim} for the three systems differ by less than 1.5 %. Note also that as soon as $\ell/a_2 \geq 3$, the threshold induction B_{lim} for sample 3 is not significantly

ℓ/a_2	system 1	system 2	system 3
1	—	10.69	9.72
2	—	11.66	10.69
3	6.41	12.63	12.25
4	12.83	13.41	13.22
5	13.61	13.80	13.80
6	14	14	14
7	14	14	14
8	14	14	14

Table 7.1: comparison of the threshold induction B_{lim} (in mT) for the three systems of figure 7.1 and for different ratios ℓ/a_2.

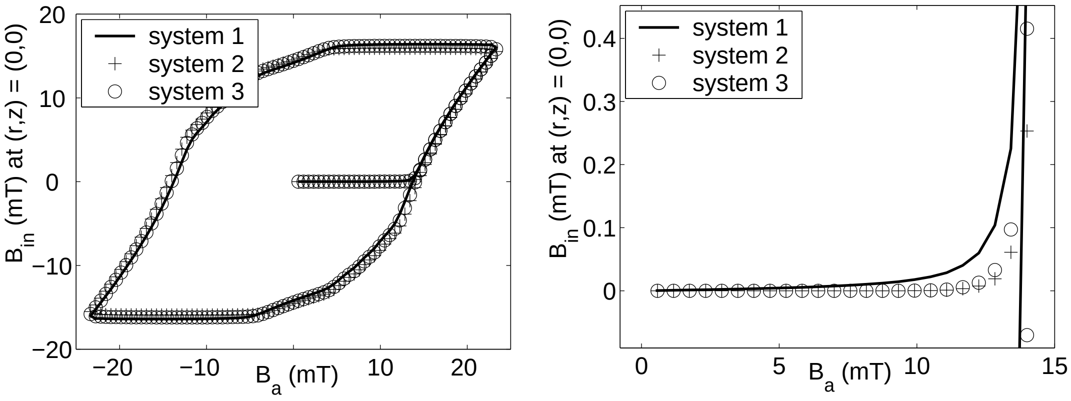

(a) (b)

Figure 7.2: evolution of the internal magnetic induction (at the centre) as a function of the applied induction for the three systems depicted in figure 7.1 and for a ratio $\ell/a_2 = 3$. Figure (b) is a zoom of figure (a) at low applied induction along the curve of first magnetization.

different from that of sample 2. This can be easily understood, as for these ratios, the shielding attenuation at the centre is less affected by the penetration via the openings (see section 6.3.3), and thus a wiring hole has limited effects.

Figure 7.2(a) shows the evolution of the internal magnetic induction as a function of the applied induction for the three systems, when $\ell = 3\,a_2$. Figure 7.2(b) is the same graph for range of inductions below threshold, $B_{\mathrm{a}} < B_{\mathrm{lim}}$. We see that the global evolution of the magnetic induction at the centre of the tube is not significantly affected by the cap. In figure 7.2(b), one can also see that, at low applied inductions, the internal induction, B_{in}, is systematically higher in system 1 (open tube) than in the two other systems.

7.2.2 Spatial variation of the shielding factor

We saw in the previous section that for long tubes, with an aspect ratio $\ell/a_2 \geq 6$, adding a cap does not significantly increase the threshold induction B_{lim}. We now turn to studying the effect of adding a cap to long tubes ($\ell = 6\ a_2$ in this case) on

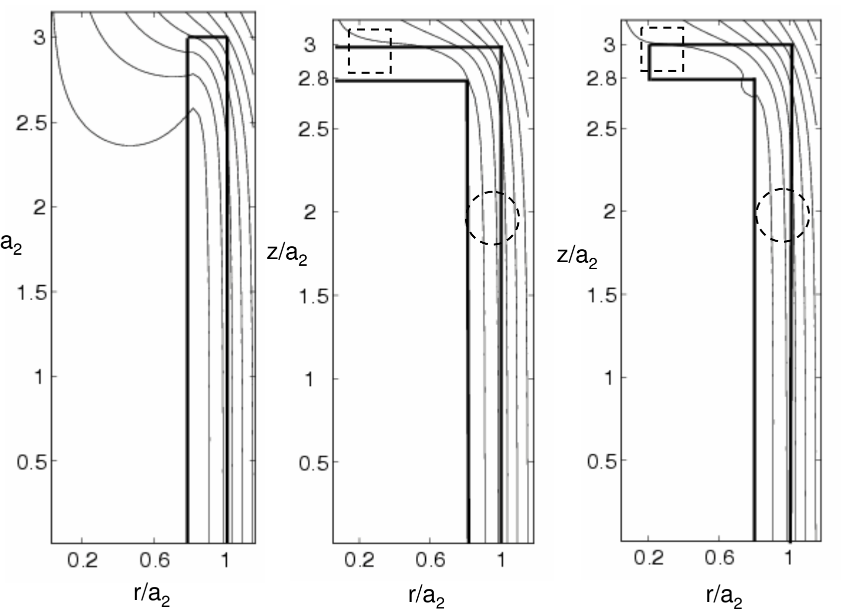

system 1 *system 2* *system 3*

Figure 7.3: magnetic field lines for systems 1, 2, and 3 if $B_{\mathrm{a}} = 0.8\ B_{\mathrm{lim}}$. The field lines distribution is weakly (resp. significantly) affected by the hole of system 3 in the region delimited by the dashed circle (resp. square).

the spatial variation of the shielding factor, and comparing systems 1 (no cap) and 2 (two caps). Afterwards, we compare systems 2 and 3.

Figure 7.3 shows the magnetic field lines for the three systems, assuming a magnetic induction $B_{\mathrm{a}} = 0.8\ B_{\mathrm{lim}}$ applied after zero-field cooling. For symmetry reasons, only a quarter of each system is shown. Figure 7.4 shows the contour lines of the ratio between the $DCSF$ for system 2 and for system 1, when $B_{\mathrm{a}} = 0.8\ B_{\mathrm{lim}}$.

From figure 7.3, a difference in the flux line patterns can be clearly observed between system 1 and system 2. In the latter case, the shape of the field lines is close to that of a bulk cylinder, which at this induction would only be partially penetrated through its outer surface [120, 149, 167]. For the central region, $z/a_2 < 1$, and for both systems 1 and 2, the internal magnetic induction is mainly due to the penetration through the thickness of the tube and not through the opening ends. Thus, the cap does not significantly affect the shielding factor, which explains that the gain plotted in figure 7.4 is smaller than ~ 3 in this region. For larger values of z, the penetration from the opening ends is the main penetration mechanism for system 1, whereas this mechanism is strongly reduced in system 2. Therefore, the gain plotted in figure 7.4 increases as one moves towards the extremity. This can also be seen more clearly in figure 7.5 which shows the $DCSF$ obtained along the z-axis, in the three systems and for $B_{\mathrm{a}} = 0.8\ B_{\mathrm{lim}}$. The shielding factor decreases by a factor of ~ 10 (20 dB) between $z = 0$ and $z = 2.5$ for the closed tube (system 2), whereas it decreases by a factor ~ 1000 (60 dB) for the open tube (system 1). Near the extremities and close to the internal surface, $z/a_2 = 2.5$, $r = a_1$, we observe in figure 7.3 a concentration of the magnetic field lines due to the finite length of sample 2. Accordingly, the gain in shielding factor in figure 7.4 is reduced in this

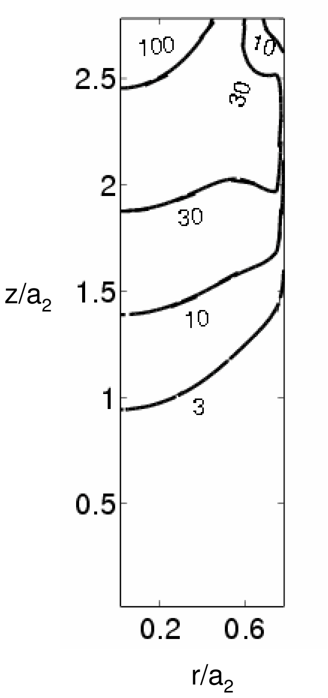

Figure 7.4: contour lines of the ratio of the $DCSF$ realized by system 2 over that realized by system 1, for $B_\mathrm{a} = 0.8\ B_\mathrm{lim}$.

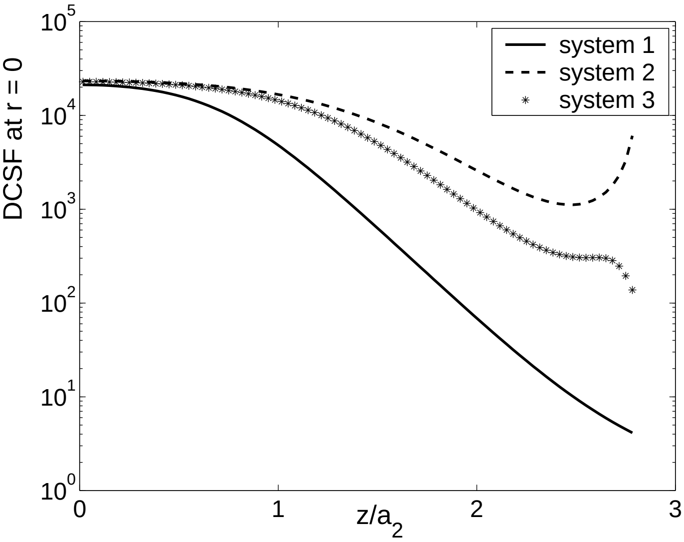

Figure 7.5: DC shielding factor for systems 1, 2, and 3 along the z-axis, for $B_\mathrm{a} = 0.8\ B_\mathrm{lim}$. As a reminder, B_lim is nearly the same for three samples, as $\ell = 6\,a_2$.

region (lower than 20 dB). Note that the contour lines of figure 7.4 are not parallel to the r-axis and that the cap effects greatly vary inside the tube. The non-penetrated central part of the cap of system 2 repels the field lines from the z-axis. Hence, the difference between the field lines distribution of systems 1 and 2 is stronger near the axis than near the internal surface, $r = a_1$. Finally, the ratio of the $DCSF$ of systems 2 and 1 increases as one moves towards $r = 0$.

To express these findings quantitatively, let us define an effective volume, V_{eff}, as the volume over which the local values of the shielding factor are at most 5 dB lower than the shielding factor at the centre ($z = 0$ and $r = 0$). From values of $DCSF$ given above, we find $V_{\mathrm{eff}} = 1.67$ cm^3 for system 1 and $V_{\mathrm{eff}} = 2.08$ cm^3 for system 2. Thus, even though B_{lim} is similar in both systems, a cap increases the volume V_{eff} by about 25 %, which is a substantial gain in the quality of the shield.

If we now look at the volume where the $DCSF$ of system 2 (closed tube) is higher by 5 dB than the $DCSF$ of system 1 (open tube), we have found that this volume decreases as the applied induction increases: this volume is respectively equal to 4.17, 3.62, and 3.16 cm^3 for $B_{\mathrm{a}} = 0.7,\ 0.8$, and 0.9 B_{lim}. This follows from the fact that as the applied induction increases, the field starts penetrating through the cap. So, the benefit of using a cap is useful mostly for low applied fields.

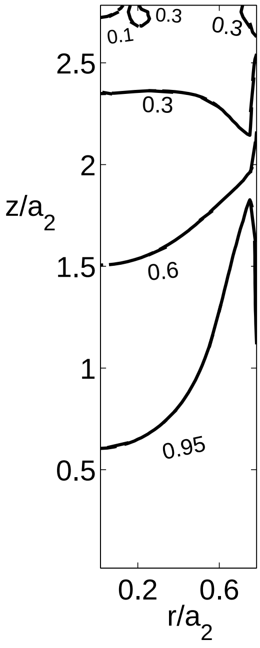

Figure 7.6: contour lines of the ratio of the DC shielding factor realized by system 3 over that realized by system 2. The applied induction is $B_{\mathrm{a}} = 0.8\ B_{\mathrm{lim}}$.

We now turn to the differences of the shielding properties between system 2 and system 3. Figure 7.6 shows the contour lines of the ratio of the $DCSF$ for system 3 over that of system 2, and for an applied induction $B_{\mathrm{a}} = 0.8\ B_{\mathrm{lim}}$. Due to the presence of the hole, the $DCSF$ of system 3 is reduced near the extremity and close to the axis, $z/a_2 = 2.5,\ r/a_2 = 0$. This reduction, by a factor ~ 10 (20 dB), is only found in the vicinity of the hole. This can also be seen in figure 7.5, where the curve corresponding to system 3 shows a kink in the vicinity of the hole. For positions with $z/a_2 < 2.5$, the $DCSF$ of system 3 is smaller than that of system 2, though roughly of the same order of magnitude. The effective volume, V_{eff}, is respectively equal to 2.08 cm^3 and 2.02 cm^3 for systems 2 and 3 if $B_{\mathrm{a}} = 0.8\ B_{\mathrm{lim}}$.

One may wonder how the size of the hole in system 3 modifies the shielding properties. When the radius of the hole is reduced by a factor 2, V_{eff} is equal to

2.06 cm^3, and the $DCSF$ increases by about 14 dB near $r = 0$, $z = \ell/2$. On the opposite, V_{eff} is reduced respectively to 1.78 cm^3 and 1.52 cm^3 when the hole radius is doubled (hole radius equal to $0.4\,a_2$) or tripled (giving a radius of $0.6\,a_2$). In the latter case, the $DCSF$ is reduced by a factor of $\sim$ 40 dB near $z = \ell/2$. This suggests that the smallest possible apertures should be used when designing a HTS magnetic shield.

From figure 7.6, we see that the effect of a hole is more important near the z-axis, directly below the hole, than near the inner surface at $r = a_1$. Indeed, the contour lines of figure 7.6 are not parallel to the r-axis. Consider the field lines distribution of figure 7.3. In the region near $r = a_1$, delimited by dashed circles, the field lines are not significantly different for system 3 and system 2. By contrast, we observe a deeper penetration in the zone delimited by a dashed square near the z-axis for system 3. Hence, the difference between the shielding properties of systems 2 and 3 is stronger in this region. For applied inductions higher than 0.8 B_{lim}, the central part of the cap of system 2 becomes penetrated, reducing its effect on the shielding properties. Hence, the difference between the shielding properties of systems 2 and 3 decreases as the applied induction increases.

7.3 Tube presenting an annular defect

As already mentioned in the beginning of this chapter, the realization of efficient large HTS magnetic shields is a technical challenge. One possibility to make large superconducting magnetic shields would be to join different tubes together after the sintering process, to obtain a larger one. In this section, we study the effect of a non-superconducting joint on the shielding properties. This study can also be used as a rough model for effects of local defects, which in this case are assumed to have an annular shape.

Figure 7.7 shows the geometry used for the simulations. Here, we are no longer assuming that the tube is symmetric about the plane $z = 0$. A HTS tube with length $\ell = 8\,a_2$ and inner radius $a_1 = 0.8\,a_2$ contains a non-superconducting ring of thickness $e = a_2/30$ at $z = h$ (black rectangle). The applied field is supposed to be quasistatic, whence we can neglect the induced currents within the normal joint with respect to superconducting shielding currents. Due to the presence of the junction, we expect the $DCSF$ to be depressed in the hollow of the superconducting tube. In this section, we evaluate this reduction and the volume of influence of the non-superconducting joint as a function of its position, h.

Figure 7.8 shows the contour lines of the relative shielding factor, RSF, which is defined as

$$RSF = \frac{DCSF(\texttt{tube with a joint})}{DCSF(\texttt{tube without a joint})}, \tag{7.9}$$

for an applied induction $B_{\text{a}} = 0.8\ B_{\text{lim}}$ and a joint that is located at equal distance from both ends, $h = 0$. Here, B_{lim}, is evaluated for a tube without the joint. Figure 7.9 shows the same ratio RSF at $B_{\text{a}} = 0.8\ B_{\text{lim}}$, but along the z-axis ($r = 0$), and for different positions h of the joint. From figure 7.8, we see that the joint not only reduces the $DCSF$ in its neighbourhood, where $r \sim a_1 = 0.8\ a_2$, but also in a region extending all the way to the tube axis, at $r = 0$. Along the axis, RSF is

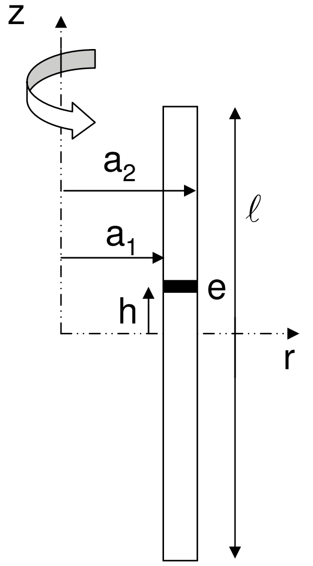

Figure 7.7: tube with an annular defect or a non-superconducting joint of thickness $e = a_2/30$, located at $z = h$.

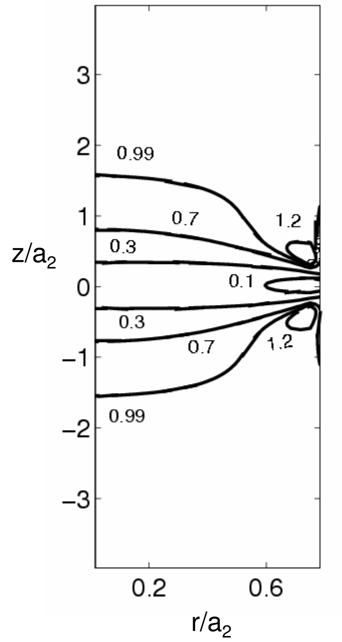

Figure 7.8: contour lines of the ratio between the $DCSF$ of a tube with an annular joint and that of a tube without a joint (see (7.9)). The applied induction is $B_{\mathrm{a}} = 0.8\ B_{\mathrm{lim}}$, where B_{lim} is defined as the threshold induction for the tube without the joint.

significantly smaller than 1 (0 dB) for $|z|/a_2 < 1.5$ and reaches 0.2 (-14 dB) at the centre, $r = 0$ and $z = 0$. The maximum reduction of $DCSF$ and the volume of the zone of influence of the joint decrease as the position h of the joint increases. The position of the minimum of RSF, z_{min}, roughly coincides with the position of the

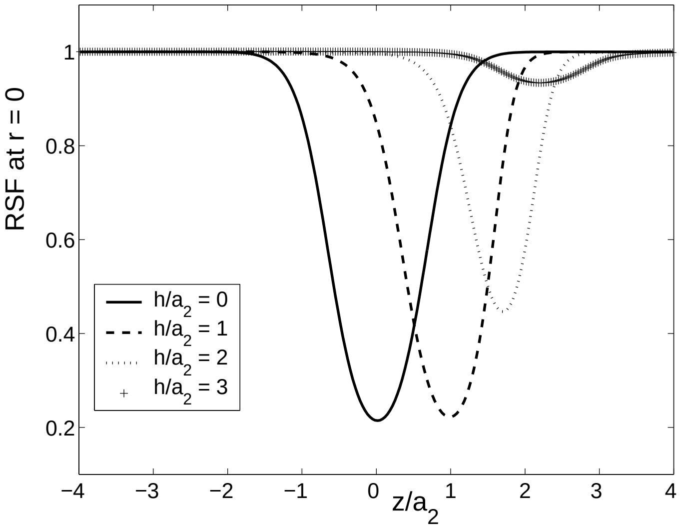

Figure 7.9: variation of the ratio RSF, (7.9), along the z-axis and for different positions of the joint. The applied induction is $B_{\mathrm{a}} = 0.8\ B_{\mathrm{lim}}$.

joint as long as $h/a_2 \leq 1$. For larger values of h, z_{min} is pushed away from the joint towards the middle of the tube, $z_{\mathrm{min}} < h$ (see figure 7.9).

The behaviour of the location of the minimum of RSF as a function of the position h of the defect can be explained as follows. When the joint is located near the tube extremity, $z = \ell/2$, the penetration via the openings is enhanced by the presence of the joint, while the radial penetration through the cylindrical shell is unchanged over most of the length ℓ of the tube. This affects the balance between the two penetration routes in favour of that occurring via the ends. As a result, the RSF minimum locates at lower z values than the position of the joint.

In a tube without a joint, the parts located near $z = \ell/2$ are first penetrated due to demagnetizing effects, see section 6.3. Hence, the effect of a joint is smaller if the joint is located near $z = \ell/2$, than if it is located at the middle, $z = 0$ (see figure 7.9). We have also found that RSF increases with the applied induction (not shown here). Indeed, as the applied induction increases, the part of the tube being fully penetrated increases in size, reducing the effect of the joint. Therefore, the effect of the joint is stronger at low applied fields.

In figure 7.8, we observe some regions near the weld where RSF is higher than 1. This has to be related to the negative B_z component near the extremities of an open superconducting tube subjected to an axial field, see section 6.3.3. Due to end effects, there is a concentration of the counter magnetic field lines near the joint, which locally enhances the shielding properties of the tube.

Figure 7.10 shows the $DCSF$ along z at $r = 0$ for different thicknesses e of the weld if $h = 0$. As the thickness of the joint e increases, the spatial variation of the reduction of the shielding factor still exhibits the shape shown in figure 7.8. But both the width of the region where $DCSF$ is reduced and the amplitude of its reduction increase with e. Whereas the $DCSF$ at the centre is reduced by 14 dB when the thickness of the weld is $a_2/30$, it is decreased by 40 dB when the thickness e is multiplied by 3 ($e = a_2/10$)! In figure 7.10, we also see that the region over

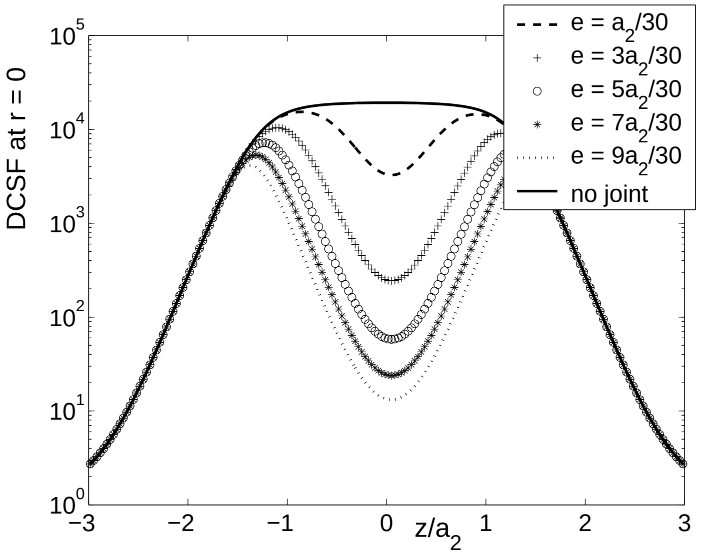

Figure 7.10: shielding factor along the z-axis for different values e of the joint thickness if $h = 0$. The field attenuation without a joint is also shown for comparison. The applied induction is $B_\mathrm{a} = 0.8\ B_\mathrm{lim}$.

which $DCSF$ is significantly reduced grows as the thickness of the weld increases. So, for practical considerations, it is important to have a joint as small as possible.

In the last part of this section, we present two possibilities to reduce the effect of the non-superconducting joint as illustrated in figure 7.11. Here, the joint is located at $h = 0$ and its thickness e is equal to $a_2/30$. The first possibility is to enclose the joint with a superconducting ring (figure 7.11(a)). The height of the ring is $t = 3\,e$ and its width is $d = 0.2\,a_2 = a_2 - a_1$. The second possibility is to make a sleeve as illustrated in figure 7.11(b). Depending on the fabrication process, several sleeve shapes are possible. As a first approach, we consider the geometry of figure 7.11(b) to simplify the calculations.

Figure 7.12 shows the shielding factor along the z-axis for a tube without a joint, for a tube with a joint, and finally, for the solutions (a) and (b) of figure 7.11. The inset is a zoom for $|z/a_2| < 2$. There is still an entry for the magnetic flux for the two proposed solutions and so, we do not recover the shielding factor of a tube without the annular defect. Nevertheless, the shielding factor is higher when using one of the two solutions of figure 7.11, in particular in the central region for which $|z/a_2| < 1$. At the centre $z = r = 0$, the $DCSF$ is increased by 9 dB when adopting solution (a). The field attenuation realized by systems (a) and (b) of figure 7.11 is nearly the same, although slightly higher for system (a) (2 dB higher at $z = r = 0$). We can also see that the maximum of the $DCSF$ is no longer located at the middle of the tube, $z = 0$, due to the joint.

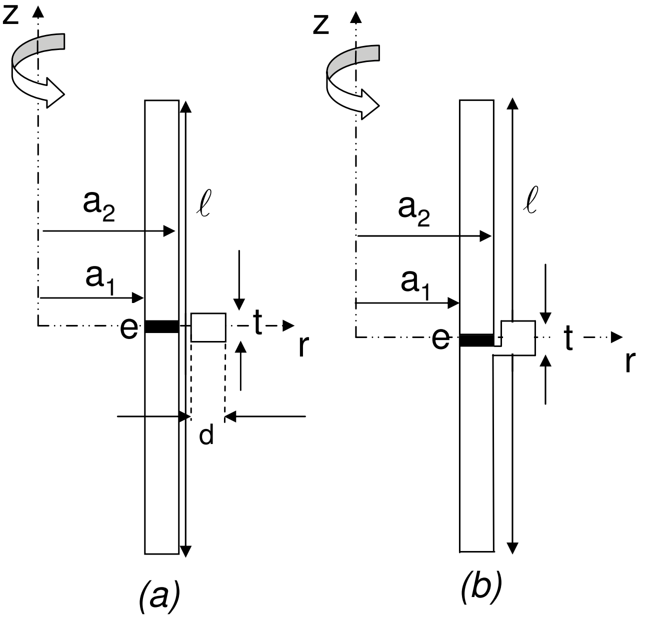

Figure 7.11: two possibilities to reduce the effect of the non-superconducting joint. The thickness e is $a_2/30$ and $t = 3\ e$.

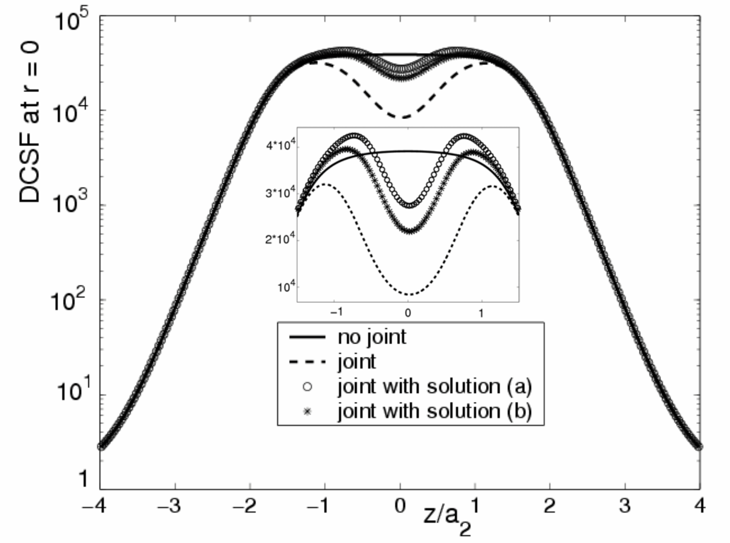

Figure 7.12: $DCSF$ along the z-axis for the two solutions of figure 7.11, for a tube without a joint, and for a tube with a joint. The applied induction is $B_\mathrm{a} = 0.8\ B_\mathrm{lim}$, where B_lim is the threshold induction for a tube without a joint. The inset is a zoom near $z = 0$.

7.4 Effect of inhomogeneities on the shielding properties

As mentioned in the introduction, the realization of large HTS shields presenting uniform superconducting properties is not obvious. Several parameters can alter this uniformity both during the fabrication and the sintering process. In the parallel geometry, when a HTS tube presents uniform superconducting properties along the z-axis, the maximum field attenuation is obtained at the centre of the tube, see the numerical results of section 6.3.3. For the EPD tube of chapter 6, we have seen in figure 6.21 that the measured variation of the shielding factor along the axis strongly differed from the theoretical one. In particular, the maximum of the shielding factor did not lie at the centre of the tube, and its position varied with the amplitude of the applied field. We have attributed this behaviour to non-homogeneous superconducting properties of the EPD tube.

In this section, we study the change of position of the maximum of $DCSF$ when a HTS tube has non-uniform superconducting properties. More specifically, we consider a case in which the tube presents two different values of the J_{c0} parameter entering (7.3). We consider the system of figure 7.13 which for $z < \ell/4$, exhibits a current density with $J_{c0} = 0.8 \times 1782$ A/cm$^2 \cong 1425$ A/cm^2, and for $\ell/4 < z < \ell/2$, has $J_{c0} = 1782$ A/cm^2. The tube has an internal radius $a_1 = 0.8\,a_2$ and a length $\ell = 8\,a_2$.

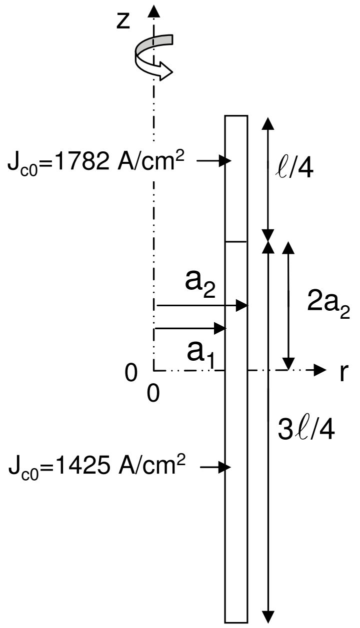

Figure 7.13: system used to study the effect of non-uniform superconducting properties on the shielding factor. The tube has an internal radius equal to $a_1 = 0.8\,a_2$, and a length $\ell = 8\,a_2$. The tube has two different values of J_{c0}, depending the position along the z-axis. For $z < \ell/4$, $J_{c0} = 1425$ A/cm^2; for $\ell/4 < z < \ell/2$, $J_{c0} = 1782$ A/cm^2.

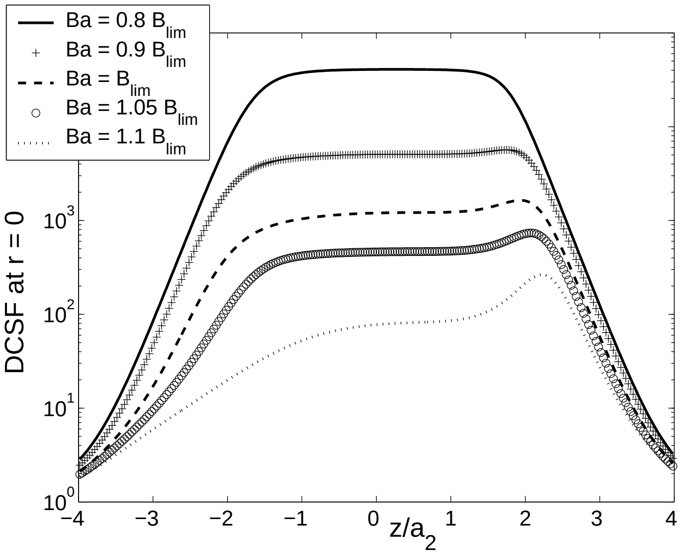

Figure 7.14: DCSF along the z-axis ($r = 0$) at different applied inductions, for the system described in figure 7.13 having non-uniform superconducting properties.

Figure 7.14 shows the variation of the shielding factor along the z-axis for different applied inductions. Here, B_{lim} is 12 mT. From figure 7.14, we see that the maximum shielding factor occurs at the centre of the tube ($z = 0$) when $B_{\mathrm{a}} = 0.80\ B_{\mathrm{lim}}$. As the applied induction is further increased, this position moves towards higher z values and lies near $z = 2\ a_2$, i.e. the position of the boundary between the two parts of the tube with different J_{c0} values. Hence, the position of the maximum field attenuation depends upon the magnitude of the applied induction when the tube has non-uniform superconducting properties.

For low B_{a} values, the tube is only partly penetrated along its side wall and some field can penetrate from the opening end at $z = \ell/2$. This results in a shielding factor that is maximum at the centre of the tube. As B_{a} is increased, the lower part, $z < \ell/4$, is penetrated before the upper part, $z > \ell/4$, because of the lower J_{c0} value. Therefore, the magnetic field can fully penetrate for $z < \ell/4$, reducing the shielding factor there. As some parts of the tube are not fully penetrated for $z > \ell/4$, the maximum of the shielding factor lies in this region. As B_{a} is further increased, the part with the lower J_{c0} value no longer acts as a shield. The magnetic field can then penetrate from the region $z < \ell/4$ towards higher z values, by the same route which allows the flux to penetrate via the ends of an open tube. As a result, the maximum shielding factor position moves towards larger z.

The results that we have presented in this section are based on a very simple model (see figure 7.13) to study of the effect of non-uniform superconducting on the shielding capabilities of a HTS tube. This model which supposes that a half of the tube has a lower J_{c0} value can not completely explain the results obtained in figure 6.21. Nevertheless, by comparing figure 7.14 (with $B_{\mathrm{a}} = 1.1\ B_{\mathrm{lim}}$) and figure 6.21 (with $B_{\mathrm{a}} = 0.21$ mT), we see that we have qualitatively the same trends for the variation of the $DCSF$ along the tube axis. This suggests that the EPD tube of table 6.2 has, as expected, non-uniform superconducting properties, and more specifically a lower critical current density in the lower half (negative z values).

7.5 Summary

In this chapter, we calculated the shielding properties, under an axial field, of tubular HTS samples which possess characteristics that are realistic. The numerical simulations are based on the algorithm of Brandt described in section 4.5.1. This study was carried out in view of designing efficient superconducting magnetic shields. Our results can be summarized as follows.

For long tubes, $\ell > 6\,a_2$, (where ℓ is the tube length and a_2 is the external radius), a cap does not increase the maximum shieldable magnetic induction B_{lim}, but reduces the spatial variation of the shielding factor. A closed tube thus presents a larger volume with a shielding factor higher than a given level. For small tube lengths, $\ell < 6\,a_2$, closed tubes also present more uniform shielding properties than open tubes. In addition, the threshold induction B_{lim} is higher for closed tubes if $\ell < 6\,a_2$, as the importance of the penetration route from the extremities is reduced by the cap. Hence, using closed tubes is particularly interesting when the volume to shield is small. As a connexion is always needed between the inside and the outside of a shield, one must also consider holes in the cap. A small hole, of diameter equal to a quarter of the cap diameter, weakly reduces the shielding capabilities of closed tubes. On the contrary, large holes, with a diameter larger than the half of the cap diameter, drastically reduce the shielding properties. Hence, the size of the apertures has to be minimized for shielding applications.

The introduction of a non-superconducting joint between stacked tubes reduces the shielding factor all along the diameter of the tube, and not only in a small region around the weld. The reduction is higher if the joint is located near the centre of the tube. Nevertheless, the effect of this non-superconducting part is relatively weak if the joint is thin. Hence, care must be taken to have the thinnest possible weld when joining different tubes to obtain a larger one. Covering the soldering by a superconducting ring or using a sleeve strongly reduces the effect of the joint.

When an open superconducting tube has uniform superconducting properties, the shielding factor is maximum at the centre of the tube. This is no longer the case when the tube presents non-homogeneities. In particular, the position of this maximum depends upon the magnitude of the applied magnetic induction.

Chapter 8

Conclusions and outlook

In contrast with normal conductors which only oppose a variation of the magnetic field, high-temperature superconductors (HTS) prevent the magnetic field itself from penetrating them. Hence, if low temperatures are allowed by the application (typically 77 K for HTS), efficient low frequency magnetic shields can be made with these superconducting materials. As HTS are brittle ceramics, it seems difficult to realize large bulk HTS shields. Therefore, our project aimed at growing $\mathrm{YBa_2Cu_3O_7}$ (Y-123) films on metallic substrates by the electrophoretic deposition (EPD) technique.

In this thesis, we first presented and discussed the superconducting and shielding properties of planar EPD samples. As the HTS films are grown on a metallic substrate with no buffer layer, the metal must be carefully chosen. We have shown that EPD coatings grown on nickel do not have a superconducting transition above 77 K because of the diffusion of nickel ions into the Y-123 layer. By contrast, coatings on silver present a macroscopic superconducting path above 77 K. Such samples typically have a critical current density $J_\mathrm{c} \cong 500$ A/cm^2 in self field and at 77 K, with a coating thickness $d \cong 50$ μm. Since the HTS layer consists of a non-textured polycrystalline material, J_c is very sensitive to small magnetic fields. According to the Bean model and taking the J_c value in self field, one deduces that the maximum magnetic induction that can be efficiently shielded with our EPD coatings on silver is about 0.3 mT. Using a home-made experimental setup, we compared the shielding factors of HTS and ferromagnetic materials. Working at a frequency $f = 103$ Hz and under an applied induction lower than 20 μT, we showed that a planar EPD sample at 77 K achieves a higher attenuation than a mu-metal plate at room temperature. The benefit of a larger attenuation may outweigh the drawbacks associated with cooling the HTS material below its critical temperature.

In a second part, we numerically and theoretically studied the shielding properties of a HTS polycrystalline tube subjected to a uniform axial magnetic field. Such a geometry has a great practical interest since a tube can be easily made, and since closed or nearly closed screens are expected to give the highest shielding factors. For the experimental study, we used a commercial HTS tube of thickness $d = 1.5$ mm. For the theoretical analysis, we followed the numerical method of Brandt. This study has pointed out the importance of geometric effects on the shielding capabilities. By using the Kim law for the variation of the current density with the magnetic induction, the constitutive law $E \propto J^n$ with a creep exponent $n = 25$, we obtained numerical results in good agreement with the experiment. We showed that the commercial tube efficiently shields magnetic inductions that are lower than the threshold induction $B_{\mathrm{lim}} = 14$ mT, at 77 K. We also detailed the two penetration routes into an open HTS tube: one from the opening ends, and one from the outer wall. Both mechanisms determine the spatial variation of the shielding factor in the hollow of the tube. In a zone extending between $z = 0$ (centre of the tube) and $z = \ell/2 - 3\,a_2$, the shielding factor is constant when $\ell > 6\,a_2$ (ℓ is the tube length and a_2 is its external radius). It then decreases as an exponential as one moves towards the extremity of the tube. As a consequence of this spatial dependence, no zone with a constant shielding factor exists for small tubes ($\ell < 6\,a_2$). Finally, we showed that the frequency response of a HTS shield follows a power law, which can be explained on the basis of the scaling laws that result from the non-linear constitutive law $E \propto J^n$.

By using a home-made measurement system, we have shown that an EPD tube strongly shields an axial low frequency magnetic induction of low amplitude. In particular, below 0.2 mT, at $T = 77$ K and $f = 103$ Hz, we measured that the field attenuation of an EPD tube of 10 cm long is much higher than that of a ferromagnetic tube at $T = 300$ K. For the EPD tube, the shielding factor is around 10^4 (80 dB) for an applied induction of ~ 0.1 mT. For a commercial mu-metal tube, we measured that the maximum shielding factor is lower than 400 (~ 52 dB) for an axial applied magnetic field with the same frequency. Our measurements show that the EPD technique can be used to make efficient magnetic shields of large sizes. However, using our experimental setup, we also found that the EPD tube does not have uniform superconducting properties along its axis.

In a third part, we compared the shielding properties of a HTS tube for an axial and for a transverse applied field. Assuming that the tube is infinitely long, we found that the shielding capabilities are weaker when the field is transverse, because of demagnetizing effects. We observed the same effect with the commercial HTS tube, which has a length equal to ten times its outer radius.

Finally, by using the numerical method of Brandt, we studied the shielding properties of axisymmetric geometries with realistic features, when subjected to a magnetic field applied parallel to the symmetry axis. In particular, we studied the effect of a cap, a non-superconducting joint, and non-uniform superconducting properties. For long tubes, $\ell > 6\,a_2$, a cap does not increase the maximum shieldable magnetic induction B_{lim}, but reduces the spatial variation of the shielding factor. For small tube lengths, $\ell < 6\,a_2$, closed tubes also present more uniform shielding properties than open tubes. In addition, the threshold induction B_{lim} is higher for closed tubes if $\ell < 6\,a_2$. The introduction of a non-superconducting joint between stacked tubes reduces the shielding factor all along the diameter of the tube, and not only in a small region around the weld. The reduction is higher if the joint is located near the centre of the tube. Care must thus be taken to have the thinnest possible weld when joining different tubes. When an open superconducting tube has uniform superconducting properties, the shielding factor is maximum at the centre of the tube. This is no longer the case when the tube presents non-homogeneities. In particular, the position of this maximum depends upon the magnitude of the applied magnetic induction.

These results point to future work in several directions. We showed that the EPD technique can be used to make large HTS magnetic shields. Nevertheless, some refinements of the technique are necessary, in particular to improve the homogeneity of the superconducting properties of the HTS layer. The system that we designed for characterizing the shielding properties of tubes in the AC mode can in fact also be used for evaluating the degree of homogeneity of the HTS layer.

To reduce or cancel the diffusion of nickel into the EPD layer during the thermal treatment, one could use a buffer layer between the substrate and the HTS coating. Then, EPD layers with a superconducting transition above 77 K could be obtained. With a nickel substrate, higher magnetic inductions might be screened than with silver, because of the combined shielding effects of the substrate and the superconductor. The interaction between these two shielding materials seems of significant interest.

In this work, we investigated the shielding properties of HTS at 77 K. Since the critical current density increases with decreasing temperature, higher magnetic inductions could be shielded at temperatures lower than the boiling point of liquid nitrogen. One could also study the shielding properties of other superconducting materials than HTS, such as MgB_2, which was recently reported to shield a magnetic induction up to 1 T at 4.2 K [150].

By using the numerical method of Brandt, other geometries than those studied in this thesis could be considered. As an example, one could calculate the shielding achieved with a HTS tube in which a small magnetic dipole is inserted (emission problem). One could also calculate the attenuation realized by a HTS plate having an axial symmetry placed near a magnetic dipole. Then, the influence of the distance between the dipole and the screen on the shielding properties could be investigated. Such a study should provide insight for problems with a source of inhomogeneous magnetic field.

Because of flux creep effects, a DC magnetic field applied to a HTS tube leads to a time varying internal magnetic induction. Such a variation is a limitation to the use of HTS to shield a DC magnetic field. It seems that the way the internal field evolves over time depends on the magnitude of the applied field. An understanding of this evolution could give informations relevant to the shielding mechanisms. This study should also determine the maximum DC field to apply to obtain a HTS shield which does not present large variations of its shielding properties over a given time.

Finally, besides these prospects drawn from our work, it would be very promising to investigate the field penetration into HTS of arbitrary shape and extend the approach of Mikitik and Brandt [121]. This theoretical study could lead to very important practical results. For the shielding application, one could for instance calculate the field penetration into a finite HTS tube subjected to a transverse field, or evaluate the shielding properties of a HTS tube in an oblique field.

In summary, many investigations can further be carried out for the application of magnetic shielding with HTS. Such a study should be carried out both experimentally and theoretically. The experimental work would help optimizing the process parameters of the EPD technique. The theoretical part could be used as a guide to design efficient HTS magnetic shields.

Appendix A

Numerical method to study the field penetration in thin films

The geometry considered here is shown in figure A.1. For simplicity, we consider that the film is rectangular, but one could solve the problem for any film shape. The only requirement is that the thickness of the film, d, tends to zero, and that $\mathbf{B}_\mathrm{a} = B_\mathrm{a}\,\hat{z}$, where $\hat{z}$ is perpendicular to the film plane.

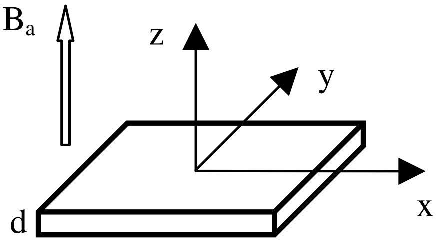

Figure A.1: infinitely thin film ($d \to 0$) in a uniform perpendicular applied induction.

In the film plane $z = 0$,

$$\mathbf{B} = B\,\hat{z}. \tag{A.1}$$

If $d \to 0$, there is no variation with respect to z, and

$$J_\mathrm{z} = 0. \tag{A.2}$$

Hence, $\mathbf{J} \perp \mathbf{B}$.

We introduce the sheet current density, $\mathbf{J}_\mathrm{s}$, defined by

$$\mathbf{J}_\mathrm{s}(x, y) = \int_{-d/2}^{d/2} \mathbf{J}(x, y, z)\,\mathrm{d}z, \tag{A.3}$$

which only depends upon (x, y). For simplicity, we write $(x, y) = \mathbf{u}$.

A useful trick for this geometry is to express the two dimensional sheet current density in terms of one scalar function $g(\mathbf{u})$:

$$\mathbf{J}_\mathrm{s}(\mathbf{u}) = \nabla \times g(\mathbf{u})\hat{z} = -\hat{z} \times \nabla g(\mathbf{u}), \tag{A.4}$$

where g plays a role similar to a local magnetic moment. Brandt proposed an equation of motion for the g function [177]. As for the axial symmetric geometry and for the bars in the transverse geometry, the algorithm is based on the resolution of a motion equation, which here has the form

$$\dot{g} = f^{-1}(g), \tag{A.5}$$

where f has to be determined for the geometry of figure A.1. Knowing g in the film, the sheet current density can be found from (A.4), and after the magnetic field in the entire space.

From the Biot-Savart law, one has in the film plane

$$B_{\mathrm{z}}(\mathbf{u}) = B(\mathbf{u}) = B_{\mathrm{a}} + \mu_0 \int_{\mathrm{S}} Q(\mathbf{u}, \mathbf{u}')g(\mathbf{u}')\mathrm{d}^2\mathbf{u}', \tag{A.6}$$

$$g(\mathbf{u}) = \frac{1}{\mu_0} \int_{\mathrm{S}} Q^{-1}(\mathbf{u}, \mathbf{u}') \left(B(\mathbf{u}') - B_{\mathrm{a}}\right) \mathrm{d}^2\mathbf{u}', \tag{A.7}$$

where the integrals are taken over the specimen area S along $\hat{x}$ and $\hat{y}$. For the thin film geometry of figure A.1, $Q(\mathbf{u}, \mathbf{u}')$ is the limit of the 3D kernel $K(\mathbf{r}, \mathbf{r}')$ obtained from the Biot-Savart law when z and z' tend to zero:

$$Q(\mathbf{u}, \mathbf{u}') = \lim_{z,z' \to 0} K(\mathbf{r}, \mathbf{r}') = \lim_{z,z' \to 0} \left[\frac{2(z-z')^2 - (x-x')^2 - (y-y')^2}{|\mathbf{r} - \mathbf{r}'|^5} \right], \tag{A.8}$$

where $\mathbf{r} = (x, y, z)$, $\mathbf{r}' = (x', y', z')$. The finding of a well behaved integral kernel, and its inverse, is a non-trivial task as the kernel becomes highly singular when one performs the limit of zero thickness [72, 178].

Let us define the sheet resistivity

$$\rho_{\mathrm{d}} = \rho/d, \tag{A.9}$$

where $\rho = E/J$. Then,

$$\mathbf{E} = \rho_{\mathrm{d}}\mathbf{J}_{\mathrm{s}} = -\rho_{\mathrm{d}}\hat{z} \times \nabla g. \tag{A.10}$$

From $\nabla \times \mathbf{E} = -\partial \mathbf{B}/\partial t$,

$$\dot{B} = \nabla \cdot \left(\rho_{\mathrm{d}} \nabla g\right). \tag{A.11}$$

Taking the time derivative of (A.7), we finally obtain the equation of motion to solve:

$$\dot{g}(\mathbf{u}, t) = \frac{1}{\mu_0} \int_{\mathrm{S}} Q^{-1}(\mathbf{u}, \mathbf{u}') \left[\nabla \cdot (\rho_{\mathrm{d}} \nabla g) - \dot{B}_{\mathrm{a}}\right] \mathrm{d}^2\mathbf{u}'. \tag{A.12}$$

By solving this equation numerically, the current and magnetic field distribution has been calculated for thin films of square and rectangular shape [177, 178].

Appendix B

Publications

1. Ph. Vanderbemden, Z. Hong, T. A. Coombs, **S. Denis**, M. Ausloos, J. Schwartz, I. B. Rutel, N. Hari Babu, D. A. Cardwell, and A. M. Campbell, "Behavior of bulk high-temperature superconductors of finite thickness subjected to crossed magnetic fields," *Phys. Rev. B*, vol. 75, pp. 174515-1 - 174515-14, 2007
2. **S. Denis**, M. Dirickx, Ph. Vanderbemden, M. Ausloos, and B. Vanderheyden, "Field penetration into high-temperature superconducting tubes: effects of a cap, a non-superconducting joint, and non-uniform superconducting properties," *Supercond. Sci. Technol.*, vol. 20, pp. 418-427, 2007
3. **S. Denis**, L. Dusoulier, M. Dirickx, Ph. Vanderbemden, R. Cloots, M. Ausloos, and B. Vanderheyden, "Magnetic shielding properties of high-temperature superconducting tubes subjected to axial fields," *Supercond. Sci. Technol.*, vol. 20, pp. 192-201, 2007 (featured article)
4. L. Dusoulier, **S. Denis**, Ph. Vanderbemden, M. Dirickx, M. Ausloos, R. Cloots, and B. Vertruyen, "Preparation of $YBa_2Cu_3O_{7-x}$ superconducting thick films by the Electrophoretic Deposition method," J. Mat. Sci., vol. 41, pp. 8109-8114, 2006
5. **S. Denis**, G. Grenci, L. Dusoulier, R. Cloots, Ph. Vanderbemden, B. Vanderheyden, M. Dirickx and M. Ausloos, "Characterisation of the magnetic shielding properties of YBaCuO thick films prepared by electrophoretic deposition on silver substrates," J. Phys.: Conf. Ser., vol. 43, pp. 509-512, 2006
6. L. Dusoulier, **S. Denis**, J.-F. Fagnard, C. Henrist, B. Vanderheyden, Ph. Vanderbemden, A. Rulmont, M. Dirickx, M. Ausloos, R. Cloots, B. Vertruyen, "$YBa_2Cu_3O_{7-\delta}$ thick films on Ag prepared by the Electrophoretic Deposition technique," J. Phys.: Conf. Ser., vol. 43, pp. 134-137, 2006
7. L. Dusoulier, **S. Denis**, N. Nutal, C. Henrist, B. Vanderheyden, Ph. Vanderbemden, A. Rulmont, M. Dirickx, M. Ausloos, R. Cloots and B. Vertruyen, "Texturation of $YBa_2Cu_3O_{7-\delta}$ thick films by ElectroPhoretic Deposition under Magnetic Field," Key Eng. Mat., vol. 314, pp. 153-158, 2006

8. G. Grenci, **S. Denis**, L. Dusoulier, F. Pavese, N. Penazzi, “Preparation and characterization of $YBa_2Cu_3O_{7-x}$ thick films deposited on silver substrates by the electrophorectic deposition technique for magnetic screening applications,” Supercond. Sci. Technol., vol. 19, pp. 249-255, 2006
9. M. Dirickx, **S. Denis**, B. Vanderheyden, L. Dusoulier, and M. Ausloos, “Inversion of the Biot-Savart Law : an approach based on discrete sine and cosine transforms,” Nato Science Series II, vol. 142, pp. 257-264, 2004
10. P. Eyben, **S. Denis**, T. Clarysse, W. Vandervorst, “Progress towards a physical contact model for scanning spreading resistance microscopy,” Mat. Sci. Eng. B, vol. 102, pp. 132-137, 2003

Bibliography

[1] R. Clayton, *Introduction to Electromagnetic Compatibility.* John Wiley & Sons, 1992.

[2] C. Christopoulos, *Principles and techniques of electromagnetic compatibility.* CRC Press, 1995.

[3] B. Keiser, *Principles of electromagnetic compatibility.* Artech House, 1987.

[4] D. Weston, *Electromagnetic compatibility: principles and applications*, 1991.

[5] F. Pavese, *Handbook of Applied Superconductivity.* London: IoP Publishing, 1998, no. G10, ch. Magnetic shielding, pp. 1461–1483.

[6] D. Koelle, R. Kleiner, F. Ludwig, E. Dantsker, and J. Clarke, "High-transition-temperature superconducting quantum interference devices," *Rev. Mod. Phys.*, vol. 71, pp. 631–686, 1999.

[7] J. Vrba and S. Robinson, "SQUID sensor array configurations for magnetoencephalography applications," *Supercond. Sci. Technol.*, vol. 15, pp. R51–R89, 2002.

[8] V. Pizzella, S. Della Penna, C. Del Gratta, and G. Luca Romani, "SQUID systems for biomagnetic imaging," *Supercond. Sci. Technol.*, vol. 14, pp. R79–R114, 2001.

[9] P. Degauque and J. Hamelin, *Compatibilité électromagnétique ; bruits et perturbations radioélectriques.* Dunod, 1990.

[10] M. Dirickx, L. Dusoulier, and S. Denis, "Etude F03/03: blindage magnétique par matériaux supraconducteurs à haute température critique. Rapport scientifique intermédiaire."

[11] Durand, *Magnétostatique.* Masson, 1966.

[12] http://www.magnetic shield.com/shielding/material.html.

[13] http://www.magnetic shield.com/index.html.

[14] http://www.mumetal.com/index.html.

[15] http://www.mecamagnetic.fr/accueil_fr.php.

[16] http://www.mumetal.com/about_mumetal.html.

[17] H. Ibach and H. Lüth, *Solid-State Physics.* Springer, 1996.

[18] S. Denis, G. Grenci, L. Dusoulier, R. Cloots, P. Vanderbemden, B. Vanderheyden, M. Dirickx, and M. Ausloos, "Characterisation of the magnetic shielding properties of YBaCuO thick films prepared by electrophoretic deposition on silver substrates," *Journal of Physics : Conference Series*, vol. 43, pp. 509–512, 2006.

[19] R. Goldfarb, M. Lelental, and C. Thompson, "Alternating-field susceptometry and magnetic susceptibility of superconductors," in *Magnetic susceptibility of superconductors and other spin systems*, R. Hein, T. Francavilla, and D. Liebenberg, Eds. New York and London: Plenum press, 1991, pp. 49–80.

[20] P. Vanderbemden, "Determination of critical current in bulk high-temperature superconductors by magnetic flux profile measuring methods," Ph.D. dissertation, University of Liège, 1999.

[21] L. Landau and E. Lifshitz, *Electrodynamics of continuous media.* Butterworth-Heinenann, 1984.

[22] E. Brandt, "Statics and dynamics of the flux-line lattice in realistic geometries," in *Applied Sciences (series E) - Physics and Materials Science of Vortex States, Flux Pinning and Dynamics*, R. Kossowsky, S. Bose, V. Pan, and Z. Durusoy, Eds. Kluwer Academic Publishers, 1999, pp. 81–108.

[23] A. Mager, "Magnetic shields," *IEEE Trans. Magn.*, vol. MAG-6, no. 1, pp. 67–75, 1970.

[24] S. Shenfeld, "Shielding of cylindrical tubes," *IEEE Trans. Electromagn. Compat.*, vol. EMC-10, no. 1, pp. 29–34, 1968.

[25] P. Norling, P. Svedlindh, S. Rudner, and L.-D. Wernlund, "Low frequency screening and magnetic relaxation studies on $YBa_2Cu_3O_7$ electromagnetic shields," *Supercond. Sci. Technol.*, vol. 4, pp. 423–426, 1991.

[26] R. Müller, G. Fuchs, A. Grahl, and A. Köhler, "Magnetic shielding properties of $YBa_2Cu_3O_{7-x}$ tubes," *Supercond. Sci. Technol.*, vol. 6, pp. 225–232, 1993.

[27] A. Omura, K. Kotani, K. Yasu, and M. Itoh, "Analysis of the magnetic distribution within a high-temperature superconductor magnetic shielding cylinder by use of the finite element method," *Journal of physics and chemistry of solids*, vol. 67, pp. 43–46, 2006.

[28] V. Plechacek, E. Pollert, and J. Hejtmanek, "Influence of the microstructure on magnetic-shielding properties of (Bi,Pb)-Sr-Ca-Cu-O superconductor," *Materials Chemistry and Physics*, vol. 43, pp. 95–98, 1996.

[29] D. Opie, M. Read, S. Remillard, M. Brown, W. Kossler, and H. Schone, "Magnetic shielding by $Y_1Ba_2Cu_3O_{7-\delta}$ thick films," *IEEE Trans. Appl. Supercond.*, vol. 3, pp. 189–192, 1993.

[30] V. Plechacek, J. Hejtmanek, D. Sedmidubsky, K. Knizek, E. Pollert, Z. Janu, and R. Tichy, "Magnetic shielding and trapping properties of BPSCCO superconducting tubes," *IEEE Trans. Appl. Supercond.*, vol. 5, no. 2, pp. 528–531, 1995.

[31] O. Symko, W. Yeh, and D. Zheng, "Magnetic shielding and relaxation characteristics of superconducting $YBa_2Cu_3O_7$ tubes," *J. Appl. Phys.*, vol. 65, no. 5, pp. 2142–2144, 1989.

[32] E. Tjukanov, R. Cline, R. Krahn, M. Hayden, M. Reynolds, W. Hardy, and J. Carolan, "Current persistence and magnetic shielding properties of YBaCuO tubes," *Phys. Rev. B*, vol. 36, no. 13, pp. 7244–7247, 1987.

[33] F. Pavese, M. Bianco, D. Andreone, R. Cresta, and P. Rellecati, "Magnetic shielding properties of $YBa_2Cu_3O_{7-x}$ thick films deposited on silver cylinders with the continuous detonation spray technique," *Physica C*, vol. 204, pp. 1–7, 1993.

[34] T. Orlando and K. Delin, *Foundations of Applied Superconductivity.* Addison-Wesley, 1991.

[35] A. M. Forrest, "Meissner and Ochsenfeld revisited," *Eur. J. Phys.*, vol. 4, pp. 117–120, 1983.

[36] J. G. Bednorz and K. A. Müller, "Possible highTc superconductivity in the Ba-La-Cu-O system," *Z. Phys. B*, vol. 64, pp. 189–193, 1986.

[37] M. Wu, J. Ashburn, C. Torng, P. Menh, L. Gao, Z. Huang, U. Wang, and C. Chu, "Superconductivity at 93 K in a New Mixed-Phase Y-Ba-Cu-O Compound System at Ambient Pressure," *Phys. Rev. Lett.*, vol. 58, pp. 908–910, 1987.

[38] J. Nagamatsu, N. Nakagawa, T. Muranaka, Y. Zenitani, and J. Akimitsu, "Superconductivity at 39 K in magnesium diboride," *Nature*, vol. 410, p. 63, 2001.

[39] http://www.amsuper.com.

[40] A. Malozemoff, J. Mannhart, and D. Scalapino, "High-temperature cuprate superconductors get to work," *Physics Today*, vol. 58, pp. 41–47, 2005.

[41] E. Brandt, "Levitation in physics," *Science*, vol. 243, pp. 349–355, 1989.

[42] F. London and H. London, "The electromagnetic equations of the superconductor," *Proc. Roy. Soc.*, vol. A149, pp. 71–88, 1935.

[43] A. C. Rose-Innes and E. H. Rhoderick, *Introduction to superconductivity.* Pergamon, 1994.

[44] B. Cabrera, "The use of superconducting shields for generating ultra-low magnetic field regions and several related experiments," Ph.D. dissertation, Standford university, 1975.

[45] A. A. Abrikosov, "On the magnetic properties of superconductors of the second group," *Soviet Physics JETP*, vol. 5, pp. 1174–1182, 1957.

[46] U. Essmann and H. Träuble, "The direct observation of individual flux lines in type-II superconductors," *Physics Letters*, vol. 24A, pp. 526–527, 1967.

[47] P. Goa, H. Hauglin, A. Olsen, M. Baziljevich, and T. Johansen, "Magneto-optical imaging setup for single vortex observation," *Review of scientific instruments*, vol. 74, no. 1, pp. 141–146, 2003.

[48] C. Bean, "Magnetization of high-field superconductors," *Rev. Mod. Phys.*, vol. 36, pp. 31–39, 1964.

[49] J. R. Clem, "Zero-quantum superconducting magnetic shielding apparatus and method," *IEEE Trans. Mag.*, vol. MAG-19, pp. 1278–1281, 1983.

[50] J. Clem, "Zero-quantum superconducting magnetic shield," in *Monopole '83*, 1984.

[51] R. Cloots, "An investigation of several chemical and physical routes for improving the crystallographic and physical properties of various high-T$_c$ superconducting materials," Ph.D. dissertation, University of Liège, 1994.

[52] S. Stassen, "New synthesis processes for 2212 and 2223 Bi-based high-Tc superconducting ceramics," Ph.D. dissertation, University of Liège, 1996.

[53] J.-P. Mathieu, "Synthèse, caractérisation et optimisation de monodomaines superconducteurs de DyBaCuO," Ph.D. dissertation, University of Liège, 2006.

[54] M. Cyrot and D. Pavuna, *Introduction to superconductivity and high-T_c materials.* World Scientific, 1992.

[55] G. Blatter, M. Feigel'man, V. Geshkenbein, A. Larkin, and V. Vinokur, "Vortices in high-temperature superconductors," *Rev. Mod. Phys.*, vol. 66, pp. 1125–1388, 1994.

[56] A. Campbell and D. Cardwell, "Bulk high-temperature superconductors for magnet applications," *Cryogenics*, vol. 37, pp. 567–575, 1997.

[57] D. Verebelyi, C. Cantoni, J. Budai, D. Christen, H. Kim, and J. Thompson, "Critical current density of $YBa_2Cu_3O_{7-\delta}$ low-angle grain boundaries in self-field," *Appl. Phys. Lett.*, vol. 78, p. 2031, 2001.

[58] R. Klie, J. Buban, M. Varela, A. Franceschetti, C. Jooss, Y. Zhu, N. Browning, S. Pantelides, and S. J. Pennycook, "Enhanced current transport at grain boundaries in high-Tc superconductors," *Nature*, vol. 435, pp. 475–478, 2005.

[59] Z. Ivanov, P. Nilsson, D. Winkler, J. Alarco, T. Claeson, E. Stepantsov, and A. Tzalenchuk, "Weak links and dc SQUIDS on artificial nonsymmetric grain boundaries in $YBa_2Cu_3O_{7-\delta}$," *Appl. Phys. Lett.*, vol. 59, pp. 3030–3032, 1991.

[60] N. Heinig, R. Redwing, I. Fei Tsu, A. Gurevich, J. Nordman, S. Babcock, and D. Larbalestier, "Evidence for channel conduction in low misorientation angle [001] tilt $YBa_2Cu_3O_{7-x}$ bicrystal films," *Appl. Phys. Lett.*, vol. 69, pp. 577–579, 1996.

[61] K. Salama, V. Selvamanickam, L. Gao, and K. Sun, "High current density in bulk $YBa_2Cu_3O_x$ superconductor," *Appl. Phys. Lett.*, vol. 54, pp. 2352–2354, 1989.

[62] R. Cloots, T. Koutzarova, J.-P. Mathieu, and M. Ausloos, "From RE-211 to RE-123. how to control the final microstructure of superconducting single-domains," *Supercond. Sci. Technol.*, vol. 18, pp. R9–R23, 2005.

[63] T. Aselage and K. Keefer, "Liquidus relations in Y-Ba-Cu oxides," *J. Mater. Res.*, vol. 6, pp. 1279–1291, 1988.

[64] S. Meslin, N. Iida, K. Hari Babu, D. Cardwell, and J. Noudem, "The effect of Y-211 precursor particle size on the microstructure and properties of Y-Ba-Cu-O bulk superconductors fabricated by seeded infiltration and growth," *Supercond. Sci. Technol.*, vol. 19, pp. 711–718, 1996.

[65] N. Ogawa, I. Hirabayashi, and S. Tanaka, "Preparation of a high-Jc YBCO bulk superconductor by the platinum doped melt growth method," *Physica C*, vol. 177, pp. 101–105, 1991.

[66] B. Yang, X. Wang, C. Wang, R. Wang, C. Cul, and S. Li, "Single-crystal YBaCuO thin films with high critical current density on $Zr(Y)O_2$, $SrTiO_3$, and $LaAlO_3$, deposited by DC-magnetron sputtering," *Supercond. Sci. Technol.*, vol. 4, pp. 143–148, 1991.

[67] S. Brück and J. Albrecht, "Experimental evidence of the dominant role of low-angle grain boundaries for the critical current density in epitaxially grown $YBa_2Cu_3O_{7-\delta}$ thin films," *Phys. Rev. B*, vol. 71, pp. 174 508–1 – 174 508–5, 2005.

[68] H. Walter, M. Delamare, B. Bringmann, A. Leenders, and H. Freyhardt, "Melt-textured YBaCuO with high trapped fields up to 1.3 T at 77 K," *J. Mater. Res.*, vol. 15, pp. 1231–1234, 2000.

[69] S. Kim, D. Feldmann, D. Verebelyi, C. Thieme, X. Li, A. Polyanskii, and D. Larbalestier, "Influence of the grain boundary network on the critical current density of deformation-textured $YBa_2Cu_3O_{7-x}$ coated conductors made

by metal-organic deposition," *Phys. Rev. B*, vol. 71, pp. 104 540–1 – 104 101–9, 2005.

[70] G. Grenci, S. Denis, L. Dusoulier, F. Pavese, and N. Penazzi, "Preparation and characterization of $YBa_2Cu_3O_{7-x}$ thick films deposited on silver substrates by the electrophorectic deposition technique for magnetic screening applications," *Supercond. Sci. Technol.*, vol. 19, pp. 249–255, 2006.

[71] S. Denis, "Blindage magnétique par matériaux suprconducteurs : étude préliminaire d'un banc de mesures magnéto-optiques," Master's thesis, University of Liège, 2004.

[72] C. Joos, J. Albrecht, H. Kuhn, S. Leonhardt, and H. Kronmüller, "Magneto-optical studies of current distributions in high-Tc superconductors," *Rep. Prog. Phys.*, vol. 65, pp. 651–788, 2002.

[73] A. Campbell, "Screening by high-Tc superconductors," *Supercond. Sci. Technol.*, vol. 1, pp. 65–67, 1988.

[74] J. Macfarlane, R. Driver, R. Roberts, E. Horrigan, and C. Andrikidis, "Electromagnetic shielding properties of yttrium barium cuprate superconductor," *Physica C*, vol. 153-155, pp. 1423–1424, 1988.

[75] J. Willis, M. McHenry, M. Maley, and H. Sheinberg, "Magnetic shielding by superconducting Y-Ba-Cu-O hollow cylinders," *IEEE Trans. Magn.*, vol. 25, no. 2, pp. 2502–2505, 1989.

[76] J.-P. Mathieu, J. Fagnard, P. Laurent, B. Mattivi, C. Henrist, P. Vanderbemden, M. Ausloos, and R. Cloots, "Silver paint as a soldering agent for DyBaCuO single-domain welding," *Supercond. Sci. Technol.*, vol. 18, pp. 508–512, 2005.

[77] S. Haseyama, N. Fujinaka, S. Yoshizawa, and H. Nakane, "Bi-2223 large sized magnetic shields prepared by jointing sintered bulks," *Physica C*, vol. 354, pp. 437–440, 2001.

[78] H. Matsuba, A. Yahara, and D. Irisawa, "Magnetic shielding properties of HTc superconductor," *Supercond. Sci. Technol.*, vol. 5, pp. S432–S439, 1992.

[79] R. Lin, T. Chen, S. Hsu, and P. Wu, "Magnetic shielding properties of superconducting Y-Ba-Cu-O films on Ni foils," *Physica C*, vol. 185-189, pp. 2127–2128, 1991.

[80] N. Alford, S. Penn, and T. Button, "High-temperature superconducting thick films," *Supercond. Sci. Technol.*, vol. 10, pp. 169–185, 1997.

[81] F. Pavese, E. Bergadano, M. Bianco, D. Ferri, D. Giraudi, and M. Vanolo, "Progress in fabrication of large magnetic shields by using extended YBCO thick films sprayed on stainless steel with the HVOF technique," *Advances in Cryogenic Engineering*, vol. 42, pp. 917–922, 1996.

[82] J. Karthikeyan, A. Palthankar, P. Chaddah, and K. Sreekumar, “Study of the propagation of an AC magnetic field through superconducting thick films,” *Supercond. Sci. Technol.*, vol. 4, pp. 250–256, 1991.

[83] H. Ohta, M. Aono, T. Matsui, Y. Uchikawa, K. Kobayashi, K. Tanabe, S. Takeuchi, K. Narasaki, S. Tsunematsu, Y. Koyabu, Y. Kamekawa, K. Nakayama, T. Shimizu, K. Koike, K. Hoshino, H. Kotaka, E. Sudoh, H. Takahara, Y. Yoshida, K. Shinada, M. Takahata, Y. Yamada, and K. Kamijo, “Neuromagnetic SQUID Measurement in a Superconducting Magnetic Shield,” *IEEE Trans. Appl. Supercond.*, vol. 9, pp. 4073–4076, 1999.

[84] H. Ohta, T. Matsui, Y. Aono, M. andUchikawa, K. Kobayashi, K. Tanabe, S. Takeuchi, K. Narasaki, S. Tsunematsu, Y. Koyabu, Y. Kamekawa, K. Nakayama, T. Shimizu, K. Koike, K. Hoshino, H. Kotaka, E. Sudoh, H. Takahara, Y. Yoshida, K. Shinada, M. Takahata, Y. Yamada, and K. Kamijo, “A 64-channel whole-head SQUID system in a superconducting magnetic shield,” *Supercond. Sci. Technol.*, vol. 12, pp. 762–765, 1999.

[85] P. Sarkar and P. Nicholson, “Electrophoretic deposition (EPD) : Mechanisms, Kinetics, and Application to Ceramics,” *J. Am. Ceram. Soc.*, vol. 79, no. 8, pp. 1987–2002, 1996.

[86] O. Van der Biest and L. Vandeperre, “Electrophoretic deposition of materials,” *Annu. Rev. Mater. Sci.*, vol. 29, pp. 327–352, 1999.

[87] M. Gani, “Electrophoretic deposition - A Review,” *Industr. Ceram.*, vol. 14, pp. 163–173, 1994.

[88] W. Ryan and E. Massoud, “Electrophoretic deposition could speed up ceramic casting,” *Interceram.*, vol. 2, pp. 117–119, 1979.

[89] N. De Calmes, “Comportement de l´oxyde de titane dans la cataphorèse,” Ph.D. dissertation, Lille university, 1995.

[90] A. Boccaccini and I. Zhitomirsky, “Application of electrophoretic and electrolytic deposition techniques in ceramics processing,” *Current Opinion in Solid State and Materials Science*, vol. 6, pp. 251–260, 2002.

[91] C. Chu and B. Dunn, “Fabrication of $YB_2Cu_3O_{7-y}$ superconducting coatings by electrophoretic deposition,” *Appl. Phys. Lett.*, vol. 55, pp. 492–494, 1989.

[92] H. Maiti, S. Datta, and R. Basu, “High-T_c superconductor coating on metal substrates by an electrophoretic technique,” *J. Am. Ceram. Soc*, vol. 72, pp. 1733–1735, 1989.

[93] L. Woolf, W. Raggio, F. Elsner, M. Fisher, R. Stephens, T. Figueroa, C. Shearer, J. Rose, K. Schaubel, R. Olstad, T. Ohkawa, D. Duggan, M. DiMartino, and F. R.L., “Continuous fabrication of high-temperature superconductor coated metal fiber and multifilamentary wire,” *Appl. Phys. Lett.*, vol. 58, pp. 534–536, 1991.

[94] P. Sarkar, S. Mathur, P. Nicholson, and C. Stager, “Fabrication of textured Bi-Sr-Ca-Cu-O thick film by electrophoretic deposition,” *J. Appl. Phys*, vol. 69, pp. 1775–1777, 1991.

[95] C. Kao, H. Tang, Y. Shiue, S. Sheen, and M. Wu, “Fabrication of $Bi_{1.7}Pb_{0.4}Sr_{1.6}Ca_{2.4}Cu_{3.6}0_y$ superconducting films on silver substrates by the electrophoretic deposition technique,” *J. Mater. Sci. Lett.*, vol. 12, pp. 1793–1794, 1993.

[96] J. Yau and Y. Wong, “Rapid synthesize of Bi-2223 precursor for the fabrication of superconducting tapes using electrophoretic deposition,” *Physica C*, vol. 339, pp. 79–87, 2000.

[97] L. Dusoulier, S. Denis, N. Nutal, C. Henrist, B. Vanderheyden, P. Vanderbemden, A. Rulmont, M. Dirickx, M. Ausloos, R. Cloots, and B. Vertruyen, “Texturation of $YBa_2Cu_3O_{7-x}$ by electrophoretic deposition under magnetic field,” *Key Engineering Materials*, vol. 314, pp. 153–157, 2006.

[98] L. Dusoulier, S. Denis, P. Vanderbemden, M. Dirickx, M. Ausloos, R. Cloots, and B. Vertruyen, “Preparation of $YBa_2Cu_3O_{7-x}$ superconducting thick films by the electrophoretic deposition method,” *J. Mater. Sci.*, vol. 41, pp. 8109–8114, 2006.

[99] D. Soh, Y.-Q. Shan, J. Park, Y. Li, and Y. Cho, “Preparation of YBCO superconducting thick film by electrophoresis,” *Physica C*, vol. 337, pp. 44–48, 2000.

[100] D. Bhattacharya, S. Roy, R. Basu, A. Das Sharma, and H. Maiti, “Critical current in electrophoretically deposited thick films of YBCO superconductor,” *Materials Letters*, vol. 16, pp. 337–341, 1993.

[101] D. Johnson, D. Opie, H. Schone, M. Lanagan, and J. Stevens, “High-temperature superconducting magnetic shields formed by deep drawing,” *IEEE Trans. Appl. Supercond.*, vol. 6, pp. 51–54, 1996.

[102] http://www.goodfellow.com/csp/active/gfHome.csp.

[103] Z. He, Z. Chen, J. Xia, G. Pan, Y. Qian, and Q. Zhang, “Doping effects of 3D metal on single-phase $YBa_2Cu_3O_{7-\delta}$,” *J. Appl. Phys.*, vol. 64, no. 7, pp. 3589–3592, 1988.

[104] J. M. S. Skakle, “Crystal chemical substitutions and doping of $YBa_2Cu_3o_x$ and related superconductors,” *Materials Science and Engineering R*, vol. 23, pp. 1–40, 1998.

[105] S. Ondono-Castillo and N. Casan-Pastor, “Deposition of $YBa_2Cu_3O_{7-\delta}$ over metallic substrates by electrophoresis of suspensions in isobutylmethylketone. influence of electric field, thermal and mechanical treatments,” *Physica C*, vol. 268, pp. 317–333, 1996.

[106] M. Kawachi, N. Sato, K. Noto, and M. Yoshizawa, “Fabrication of grain-aligned YBCO films using electrophoretic deposition in a magnetic field,” *Physica C*, vol. 372-376, pp. 802–805, 2002.

[107] A. Campbell and J. Evetts, “Flux vortices and transport currents in type II superconductors,” *Advances in Physics*, vol. 21, pp. 199–428, 1972.

[108] K. H. Müller, D. Matthews, and R. Driver, “Critical current density of ceramic high-temperature superconductors in a low magnetic field,” *Physica C*, vol. 191, pp. 339–346, 1992.

[109] A. Campbell and F. Blunt, “Probing self field effects on intergrain currents using an AC technique,” *Physica C*, vol. 172, pp. 253–259, 1990.

[110] Y. Kim, C. Hempstead, and A. Strnad, “Critical persistent currents in hard superconductors,” *Phys. Rev. Lett.*, vol. 9, no. 7, pp. 306–309, 1962.

[111] Y. Yeshurun, A. Malozemoff, and A. Shaulov, “Magnetic relaxation in high-temperature superconductors,” *Rev. Mod. Phys.*, vol. 68, no. 3, pp. 911–949, 1996.

[112] E. Brandt, “The flux-line lattice in superconductors,” *Rep. Prog. Phys.*, vol. 58, pp. 1465–1594, 1995.

[113] A. Diaz, L. Mechin, P. Berghuis, and J. Evetts, “Observation of viscous flux flow in $YBa_2Cu_3O_{7-\delta}$ low-angle grain boundaries,” *Phys. Rev. B*, vol. 58, pp. R2960–R2963, 1998.

[114] Y. Cha, “An empirical correlation for E(J,T) of a melt-cast-processed BSCCO-2212 superconductor under self-field,” *IEEE Trans. Appl. Supercond.*, vol. 13, no. 2, pp. 2028–2031, 2003.

[115] A. Nader, “Magnetic relaxation of a superconducting slab : a description of the temporal evolution,” *Supercond. Sci. Technol.*, vol. 15, pp. 894–897, 2002.

[116] P. Kes, J. Aarts, J. Van den Berg, C. Van der Beek, and J. Mydosh, “Thermally assisted flux flow at small driving forces,” *Supercond. Sci. Technol.*, vol. 1, pp. 242–248, 1989.

[117] P. Anderson, “Theory of flux creep in hard superconductors,” *Phys. Rev. Lett.*, vol. 9, pp. 309–311, 1962.

[118] P. Anderson and Y. Kim, “Hard superconductivity: theory of the motion of Abrikosov flux lines,” *Rev. Mod. Phys.*, vol. 36, pp. 39–43, 1964.

[119] E. Zeldov, N. Amer, G. Koren, A. Gupta, R. Gambino, and M. McElfresh, “Optical and electrical enhancement of flux creep in $YBa_2Cu_3O_{7-\delta}$ epitaxial films,” *Phys. Rev. Lett.*, vol. 62, pp. 3093–3096, 1989.

[120] E. Brandt, “Superconductor disks and cylinders in an axial magnetic field. I. flux penetration and magnetization curves,” *Phys. Rev. B*, vol. 58, pp. 6506–6522, 1998.

[121] G. Mikitik and E. Brandt, “Critical state in type-II superconductors of arbitrary shape,” *Phys. Rev. B*, vol. 71, pp. 012 510–, 2005.

[122] J. Clem, “Flux-line cutting losses in type-II superconductors,” *Phys. Rev. B*, vol. 26, pp. 2463–2473, 1982.

[123] J. Clem and A. Perez-Gonzalez, “Flux-line cutting and flux-pinning losses in type-II superconductors in rotating magnetic fields,” *Phys. Rev. B*, vol. 30, pp. 5041–5047, 1984.

[124] L. Prigozhin, “The bean model in superconductivity: variational formulation and numerical solution,” *J. Comp. Phys.*, vol. 129, pp. 190–200, 1996.

[125] K. Berger, “Etude des phénomènes couplés magnétothermiques dans les supraconducteurs à haute température,” Ph.D. dissertation, Nancy, 2006.

[126] F. Sirois, Y. Basile-Bellavance, and J. Cave, “Non-linear magnetic diffusion in a Bi2212 hollow cylinder : Measurements and numerical simulations,” 2006, preprint ASC 2006.

[127] S. Ikuno and A. Kamitani, “Shielding current density analysis of axisymmetric HTS by element-free Galerkin method,” *IEEE Trans. Appl. Supercond.*, vol. 15, pp. 3688–3691, 2005.

[128] A. Sanchez and C. Navau, “Magnetic properties of finite superconducting cylinders. I. uniform applied field,” *Phys. Rev. B*, vol. 64, pp. 214 506–1–214 506–10, 2001.

[129] C. Navau and A. Sanchez, “Magnetic properties of finite superconducting cylinders. II. nonuniform applied field and levitation force,” *Phys. Rev. B*, vol. 64, pp. 214 507–1–214 507–10, 2001.

[130] D.-X. Chen, E. Pardo, and C. Gu, “Critical-state and eddy-current ac susceptibilities of conducting cylinders,” *Supercond. Sci. Technol.*, vol. 18, pp. 1280–1289, 2005.

[131] G. James, *Modern Engineering Mathematics.* Addison-Wesley, 1996.

[132] L. Prigozhin, “Analysis of critical-state problems in type-II superconductivity,” *IEEE Trans. Appl. Supercond.*, vol. 7, no. 4, pp. 3866–3873, 1997.

[133] S. Stavrev, “Modelling of high temperature superconductors for ac power applications,” Ph.D. dissertation, Ecole polytechnique fédérale de Lausanne, 2002.

[134] Z. Hong, A. Campbell, and T. Coombs, “Numerical solution of critical state in superconductivity by finite element software,” *Supercond. Sci. Technol.*, vol. 19, pp. 1246–, 2006.

[135] S. Stavrev, F. Grilli, B. Dutoit, N. Nibbio, I. Klutsch, G. Meunier, P. Tixador, Y. Yang, and E. Martinez, “Comparison of numerical methods for modeling of superconductors,” *IEEE Trans. Magn.*, vol. 38, no. 2, pp. 849–852, 2002.

[136] E. Brandt, “Superconductors of finite thickness in a perpendicular magnetic field : strips and slabs,” *Phys. Rev. B*, vol. 54, no. 6, pp. 4246–4264, 1996.

[137] Keithley, *Low level measurements handbook.* Keithley Instruments, 1998.

[138] A.-F. Gerday, “Conception et réalisation d’un système de mesure des propriétés magnétiques basse fréquence de films supraconducteurs,” Master’s thesis, University of Liège, 2004.

[139] N. Ashcroft and N. Mermin, *Solid State Physics*, 1900.

[140] L. Dusoulier, S. Denis, J.-F. Fagnard, C. Henrist, B. Vanderheyden, P. Vanderbemden, A. Rulmont, M. Dirickx, M. Ausloos, R. Cloots, and B. Vertruyen, “$YBa_2Cu_3O_{7-\delta}$ thick films on Ag prepared by the Electrophoretic Deposition technique,” *Journal of Physics : Conference Series*, vol. 43, pp. 134–137, 2006.

[141] L. Dusoulier, “Elaboration de films épais d’$YBa_2Cu_3O_{7-x}$ par électrophorèse et plasma-spray,” Ph.D. dissertation, University of Liège, 2007.

[142] Y. Idemoto and Y. Fueki, “Melting Point of Superconducting Oxides as a Function of Oxygen Partial Pressure,” *Japan. J. Appl. Phys.*, vol. 29, pp. 2729–2731, 1990.

[143] H. Niu, H. Shinkawata, Y. Hagiwara, and S. Kishino, “Fabrication of Y-Ba-Cu-O superconducting films by electrophoresis with the use of firing in helium ambience,” *Supercond. Sci. Technol.*, vol. 4, pp. 229–231, 1991.

[144] S. Hur and S. Lee, “Fabrication of $YBa_2Cu_3O_{7-x}$ superconducting film with CeO_2/BaTiO double buffer layer,” *Thin Solid Films*, vol. 398-399, pp. 444–447, 2001.

[145] K. Yamagiwa, K. Matsumoto, and I. Hirabayashi, “Solid-phase epitaxial growth of oxide buffer materials for (Rare earth)$Ba_2Cu_3O_{7-y}$ superconductor,” *J. Mat. Res.*, vol. 15, pp. 2547–2557, 2000.

[146] A. Campbell and F. Blunt, “The effect of sample shape on the measurement of intergrain currents in YBaCuO,” *Supercond. Sci. Technol.*, vol. 3, pp. 450–453, 1990.

[147] M. Itoh, T. Ohyama, T. Minemoto, K. Numata, and K. Hoshino, “The improvement in magnetic shielding by use of a double-cylinder configuration of high-Tc oxide superconductors,” *J. Phys. D: Appl. Phys.*, vol. 25, pp. 1630–1634, 1992.

[148] A. Omura, M. Oka, K. Mori, and M. Itoh, “Magnetic shielding effects of the superposition of a ferromagnetic cylinder over an HTS cylinder : magnetic shielding dependence on the air gap between the BPSCCO and soft-iron cylinders,” *Physica C*, vol. 386, pp. 506–511, 2003.

[149] S. Denis, L. Dusoulier, M. Dirickx, P. Vanderbemden, R. Cloots, M. Ausloos, and B. Vanderheyden, "Magnetic shielding properties of high-temperature superconducting tubes subjected to axial fields," *Supercond. Sci. Technol.*, vol. 20, pp. 192–201, 2007.

[150] T. Cavallin, R. Quarantiello, A. Matrone, and G. Giunchi, "Magnetic shielding of MgB_2 tubes in applied DC and AC field," *Journal of Physics : Conference Series*, vol. 43, pp. 1015–1018, 2006.

[151] K. Yasui, Y. Tarui, and M. Itoh, "Improvement of the magnetic shielding effects by the superposition of a multi-layered ferromagnetic cylinder over an hts cylinder : Relationship between the shielding effects and the layer number of the ferromagnetic cylinder," *Journal of Physics : Conference Series*, vol. 43, pp. 1393–1396, 2006.

[152] J. Karthikeyan, A. Paithankar, R. Prasad, and N. Sonl, "Magnetic shielding and harmonic generation of high-tc superconducting tubes," *Supercond. Sci. Technol.*, vol. 7, pp. 949–955, 1994.

[153] J. Purpura and T. Clem, "The fabrication and characterization of high temperature superconducting magnetic shields," *IEEE Trans. Magn.*, vol. 22, no. 2, pp. 2506–2510, 1989.

[154] S. Haindl, F. Hengstberger, H. Weber, S. Meslin, J. Noudem, and X. Chaud, "Hall probe mapping of melt processed superconductors with artificial holes," *Supercond. Sci. Technol.*, vol. 19, pp. 108–115, 2006.

[155] S. Meslin, C. Harnois, D. Chubilleau, D. Horvath, D. Grossin, E. Suddhakar, and J. Noudem, "Shaping and reinforcement of melt textured $YBa_2Cu_3O_{7-\delta}$ superconductors," *Supercond. Sci. Technol.*, vol. 19, pp. S585–S589, 2006.

[156] F. Eberhardt, A. Hibbs, and A. Campbell, "Flux trapping and magnetization of hollow superconducting cylinders," *Cryogenics*, vol. 28, pp. 681–684, Oct. 1988.

[157] R. Lin, T. Chen, Y. Chen, and L. Chen, "Magnetic shielding properties of Y-Ba-Cu-O films on Ni and Ag foils," *Chinese Journal of Physics*, vol. 31, no. 6-11, pp. 1103–1108, 1993.

[158] D. Bajusz, "Conception et réalisation d'un dispositif de mesure de blindage magnétique. Application aux supraconducteurs à haute température critique." Master's thesis, University of Liège, 2005.

[159] http://www.arepoc.sk/.

[160] G. Giunchi, G. Ripamonti, T. Cavallin, and E. Bassani, "The reactive liquid Mg infiltration process to produce large superconducting bulk MgB_2 manufacts," *Cryogenics*, vol. 46, pp. 237–242, 2006.

[161] C. Bean, "Magnetization of hard superconductors," *Phys. Rev. Lett.*, vol. 8, no. 6, pp. 250–253, 1962.

[162] A. Hussain and M. Sayer, “Simple magnetic shielding experiment on high Tc superconducting bulk ceramics and thin films, metals and alloys,” *Cryogenics*, vol. 32, no. 1, pp. 64–68, 1992.

[163] H. Niculescu, R. Schmidmeier, B. Topolscki, and P. Gielisse, “Shielding effects in ceramic superconductors,” *Physica C*, vol. 299, pp. 105–112, 1994.

[164] http://www.can.cz/.

[165] A. Forkl, “Magnetic flux distribution in single crystalline, ceramic and thin film high-Tc superconductors,” *Physica scripta*, vol. T49, pp. 148–158, 1993.

[166] K. Müller, J. MacFarlane, and R. Driver, “Josephson vortices and flux penetration in high temperature superconductors,” *Physica C*, vol. 158, pp. 69–75, 1989.

[167] C. Navau, A. Sanchez, E. Pardo, D.-X. Chen, E. Bartolomé, X. Granados, T. Puig, and X. Obradors, “Critical state in finite type-II superconducting rings,” *Phys. Rev. B*, vol. 71, pp. 214 507–1–214 507–9, 2005.

[168] E. Brandt, “Susceptibility of superconductor disks and rings with and without flux creep,” *Phys. Rev. B*, vol. 55, no. 21, pp. 14 513–14 526, 1997.

[169] E. Brandt and M. Indenbom, “Type-II superconductor strip with current in a perpendicular magnetic field,” *Phys. Rev. B*, vol. 48, no. 17, pp. 12 893–12 906, 1993.

[170] M. Pannetier, F. Klaasen, R. Wijngaarden, M. Welling, K. Heeck, J. Huijbregtse, B. Dam, and R. Griessen, “Magneto-optical investigation of flux penetration in a superconducting ring,” *Phys. Rev. B*, vol. 64, pp. 144 505–1–144 505–7, 2001.

[171] T. Schuster, H. Kuhn, E. Brandt, M. Indenbom, M. Koblischka, and M. Konczykowski, “Flux motion in thin superconductors with inhomogeneous pinning,” *Phys. Rev. B*, vol. 50, no. 22, pp. 16 684–16 707, 1994.

[172] http://www.mushield.com/.

[173] B. Guillaume, F. Boschini, A. Rulmont, M. Ausloos, and R. Cloots, “Influence of the shaping effect on hardness homogeneity by Vickers indentation analysis,” *Journal of European Ceramic Society*, vol. 26, pp. 3191–3196, 2006.

[174] S. Denis, M. Dirickx, P. Vanderbemden, M. Ausloos, and B. Vanderheyden, “Field penetration into hard type-II superconducting tubes: effects of a cap, a non-superconducting joint, and non-uniform superconducting properties,” *Supercond. Sci. Technol.*, vol. 20, pp. 418–427, 2007.

[175] R. Doyle, A. Bradley, W. Lo, D. Cardwell, A. M. Campbell, P. Vanderbemden, and R. Cloots, “High field behavior of artificially engineered boundaries in melt-processed $YBa_2Cu_3o_{7-\delta}$,” *Appl. Phys. Lett.*, vol. 73, pp. 117–120, 1998.

[176] P. Vanderbemden, C. Destombes, R. Cloots, and M. Ausloos, “Magnetic flux penetration and creep in BSSCO-2223 composite ceramics,” *Supercond. Sci. Technol.*, vol. 11, pp. 94–100, 1998.

[177] E. Brandt, “Square and rectangular thin superconductors in a transverse magnetic field,” *Phys. Rev. Lett.*, vol. 74, no. 15, pp. 3025–3028, 1995.

[178] T. Schuster, H. Kuhn, E. Brandt, M. Indenbom, M. Kläser, G. Müller-Voigt, H. Habermeier, H. Kronmüller, and A. Forkl, “Current and field pattern in rectangular and inhomogeneous superconductors,” *Phys. Rev. B*, vol. 52, pp. 10 375–10 389, 1995.